GRAIN ORIENTATION TEXTURE CONTROL AND ITS EFFECTS ON THE HARDNESS AND ABRASION RESISTANCE OF SINTERED CARBIDES

A Thesis

by

SAGAR DEVRAJ PATEL

Submitted to the Office of Graduate and Professional Studies of
Texas A&M University
in partial fulfillment of the requirements for the degree of

MASTER OF SCIENCE

Chair of Committee,	Hong Liang
Co-Chair of Committee,	Mathew Kuttolamadom
Committee Members,	Ibrahim Karaman
	Jyhwen Wang
Head of Department,	Ibrahim Karaman

May 2016

Major Subject: Materials Science and Engineering

ABSTRACT

The objective of this research work is to develop and evaluate a fabrication procedure that enables a degree of control over the surface and sub-surface grain orientation texture of spark plasma sintered carbides and to investigate its effects on the hardness and abrasion resistance of the material. The composite material used in this investigation is a mixture of tungsten carbide (90% WC) and cobalt (10% Co) powders. The fabrication procedure predominantly involves mixing measured weight fractions of WC and Co powders with a temporary binder (polyvinyl alcohol) so that the mixture is malleable into thin sheets, and then subjecting these to multiple high-pressure rolling operations – subjecting these sheets to high-pressure rolling is primarily responsible for partially "aligning" the grains in order to have a dominant orientation. From these sheets, a number of discs were cut, stacked, thermally de-bound (to remove the temporary binder), and then spark plasma sintered to obtain bulk cemented WC-Co samples. The relationships between the degree of orientation texture and the fabrication process conditions were investigated through X-ray diffraction (XRD). Certain mechanical properties of the samples were then characterized, including indentation hardness testing and scratch testing using a diamond engraver, in order to evaluate their comparative hardness and abrasion resistance. Manipulating the grain orientation texture in this manner thus has potential to enable a level of control over numerous mechanical properties of WC-Co hard-material composites.

ACKNOWLEDGEMENTS

I would like to express my deepest gratitude to Dr. Mathew Kuttolamadom for his guidance and motivation throughout my research. I have learnt a lot while working in his group and gained tremendous knowledge and experience in the personal and professional front. The last 15 months have been the most productive and enriching duration in my life for me and I cannot think of anyone to thank more than him for being there, always.

I would like to thank Dr. Hong Liang for her invaluable guidance and support and for being my committee chair. Next, I would like to thank Dr. Jyhwen Wang, Dr. Zachary Grasley and Dr. Ibrahim Karaman for their guidance and inputs on my work.

I would also like to thank Ms. Jules Henry for being a wonderful advisor throughout my Master's, as well as Dr. Ted Hartwig, Dr. Angie Price, Dr. Anup Bandyopadhyay, and Dr. Andrew Mott for their support in my work towards my thesis. My friends have supported and motivated me throughout my work- thank you Srushti, Avantika, Sharath, Saniya, and many more.

Finally yet importantly, I want to thank my parents, my brother and my close family members. Without their love, understanding and support, this work would have been impossible.

NOMENCLATURE

2D/3D	Two/Three Dimensional
A	Amperes
AFM	Atomic Force Microscope
BCC	Body Centered Cubic
Co	Cobalt
C	Carbon
DC	Direct electrical Current
EBSD	Electron Backscatter Diffraction
EDX	Energy Dispersive X-ray Spectroscopy
FAST	Field Assisted Sintering Technology
FCC	Face Centered Cubic
HCP	Hexagonal Close Packed
IPF	Inverse Pole Figure
MRD	Multiple of a Random Distribution
ND	Normal Direction
Ni	Nickel
ODF	Orientation Distribution Function
PECS	Pulsed Electric Current Sintering
PF	Pole Figure
PVA	Polyvinyl Alcohol

RD	Rolling Direction
SEM	Scanning Electron Microscope
SPS	Spark Plasma Sintering
TD	Transverse Direction
TGG	Templated Grain Growth
V	Volts
W	Tungsten
WC	Tungsten Carbide
XRD	X-ray Diffraction
ZnO	Zinc Oxide

TABLE OF CONTENTS

Page

LIST OF FIGURES

Page

LIST OF TABLES

Page

1. INTRODUCTION

1.1 OBJECTIVES

The objective of this research work is to develop and evaluate a fabrication procedure that enables a degree of control over the surface and sub-surface grain orientation texture of spark plasma sintered carbides, and to investigate its effects on the hardness and abrasive resistance of the material.

1.2 MOTIVATION

The primary motivation for this work is to leverage the apparent difference in hardness of the basal plane and the prismatic planes in a tungsten carbide crystal that has a hexagonal crystallographic structure. From Figure 1, it can be observed that for tungsten carbide grains, the measured hardness value on its basal plane is about 1.6 times higher than on its prismatic planes [1, 2].

Kim et al. has shown (through simulations) that the young's modulus also depends on the texture of tungsten carbide grains. For a sample with $(100)^{C}//[100]^{S}$ orientation texture, where the superscript C denotes the crystal reference frame and the superscript S denotes the sample reference frame, the modulus along the c-axis direction is invariably higher than the modulus of the randomly textured material. Also, fracture strength simulations (using a combination of mechanical and thermal load) have shown that cemented carbide sample could be strengthened between 2% and 13% by texturing the

sample with $(100)^{C}//[100]^{S}$ or $(100)^{C}//[100]^{S}$ [3]. Thus, control over the texture of WC grains has the potential to affect the mechanical and tribological properties of the bulk composite.

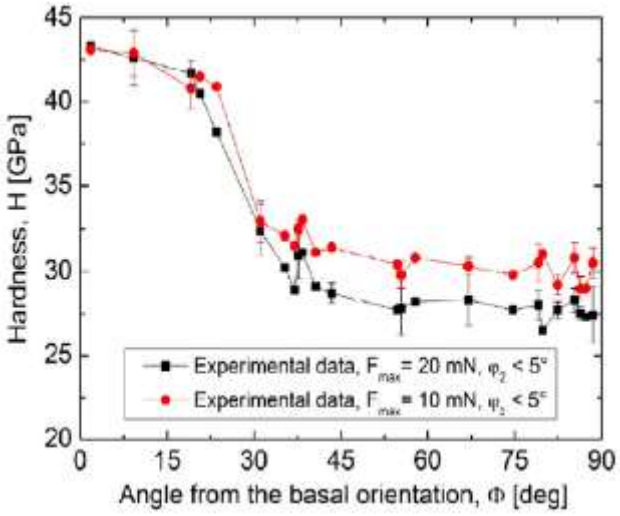

Figure 1. The hardness of WC grains as a function of grain orientation [2]

A major hurdle in achieving this objective is the inability to reliably and consistently fabricate textured sheets and/or bulk material. Previous efforts in this regard involves obtaining a textured surface in WC-Co composites by manually placing very large (average grain size of 0.5 mm) WC crystals onto a randomly oriented mixture surface with the aid of a stereomicroscope [4]. Further, no dominant orientation-texture has been achieved for WC-Co composites using any bulk-material or power-metallurgical processing, that is scalable.

1.3 METHODOLOGY

The methodology used involves mixing WC powder, Co powder, and a temporary binder (polyvinyl alcohol) to obtain high viscosity dough. This dough is subjected to a rolling-extended operation to fabricate thin (~0.5mm) sheets using high-pressure rollers and then cut into discs of diameter 40 mm. These discs are then subjected to a thermal de-binding process to remove the temporary binder. The de-bound discs are stacked in the sintering die and spark plasma sintered to obtain bulk WC-Co samples. The orientation texture and other morphology characteristics were studied through X-ray diffraction (XRD) – such evaluation was conducted for two orders of WC grain sizes as well as randomly oriented powder. These samples were then subjected to mechanical characterization testing to ascertain the effect of orientation texture and other parameters on the hardness and abrasion resistance of the material.

1.4 EXPECTED CONTRIBUTIONS

The expected contributions from this work are:

1. Development of a scalable procedure to obtain dominant grain orientation texture in a WC-Co composite,
2. A study on the effect of processing parameters on the intensity of grain orientation texture of the WC-Co samples,
3. Comparison of the effect of dominant grain texture on the hardness and abrasive resistance of WC-Co composites, and,

4. Realization of the potential to use this procedure for texturing bulk/sheet hard-material composites.

2. BACKGROUND

This chapter contains the relevant background and associated literature review for this thesis.

2.1 CEMENTED CARBIDES

Cemented carbides are metal matrix composites in which carbide particles act as the aggregate and a metallic binder serves as the matrix. In this class, tungsten carbide (WC) with cobalt (Co) as the metallic binder comprises the majority of turning and milling cutting tools.

2.1.1 History

Karl Schröter is credited with the development of cemented carbides. His initial experiments involved making the use of tungsten carbide with nickel as the binder metal. When Schröter replaced nickel with cobalt as the binder metal, cemented carbides became more superior. The compacting and sintering process developed by Schröter laid the foundation for production of cemented carbides [5].

2.1.2 Morphology

WC has a hexagonal crystal structure at room temperature with two atoms (W and C) per unit cell as shown in Figure 2. The lattice constants are a=2.906 Å and c=2.837 Å with c/a=0.976 [6].

An image of a typical WC-Co composite is shown in Figure 3. From Figure 3, it is clear that WC surfaces are faceted when embedded in Co. Three types of facets are generated: two types of prismatic $\{10\bar{1}0\}$ facets and one type of basal facets. WC primarily grows on the prismatic and basal surfaces which leads to the faceting of WC grains [7]. WC grains also have a tendency of forming truncated corners which originate from an energetic difference between the two prismatic WC/Co interfaces [8]. A schematic WC grain with truncated corners is shown in Figure 4.

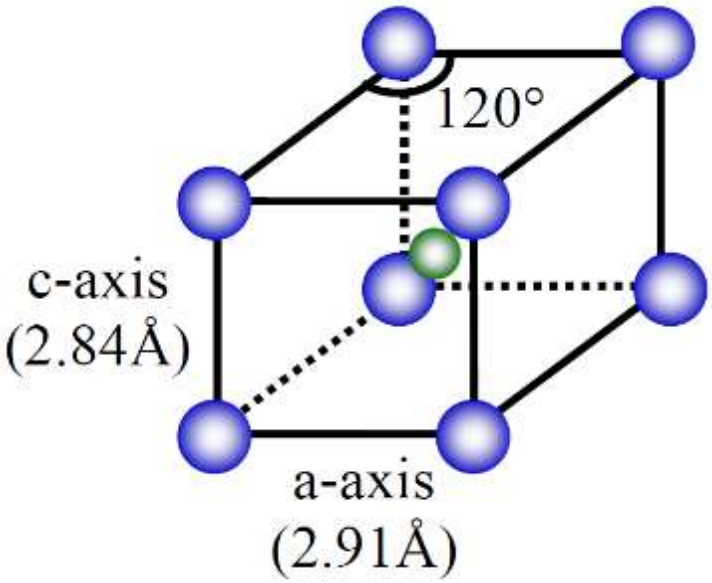

Figure 2. Crystal structure of WC. Blue atom represents W and green atom represents C. W atoms are at (0, 0, 0) and C atoms are at (1/2, 2/3, 1/2) positions in the unit cell [9].

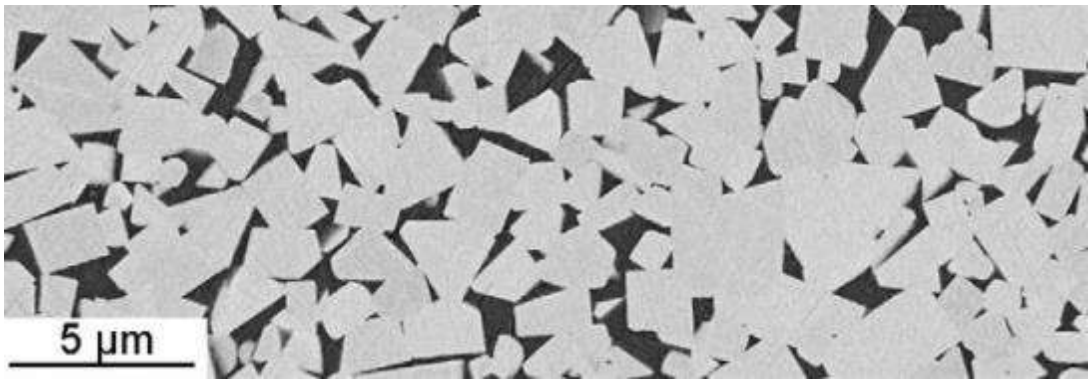

Figure 3. SEM micrograph of a typical WC-Co composite. Light grey represents WC grains and dark grey represents Co phase [10].

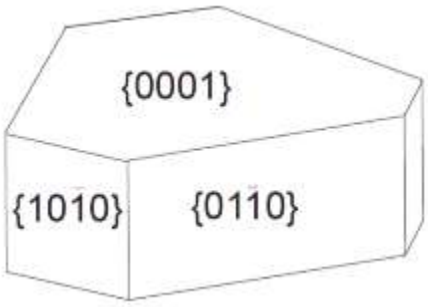

Figure 4. Schematic of the equilibrium shape of a WC particle in Co binder [11].

2.1.3 Mechanical Properties

The microstructure of cemented carbides hugely influences the physical properties. Some of the key microstructural characteristics are grain sizes, size distributions, grain shapes, grain orientation, grain misorientation, composition and the binder fraction. A few mechanical properties of WC-Co as a function of Co content are shown in Figure 5. Since hardness is directly related to compressive strength, it is inversely related to wear as shown in Figure 5. The tensile strength in bending for WC-Co increases

with increasing Co content. In addition, it is known that the wear resistance of WC-Co is five to ten times higher than that of a typical tool steel.

The hardness of carbides decreases with temperature just like any other materials as shown in Figure 6. The wide range in each group of materials in Figure 6 is due to the variety of compositions and treatments available for that group.

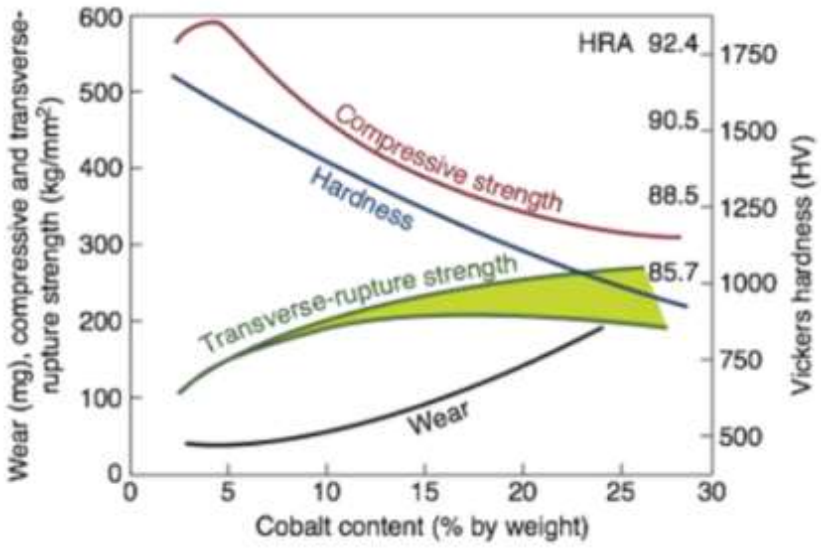

Figure 5. The effect of cobalt content on a few mechanical properties of WC-Co [12]

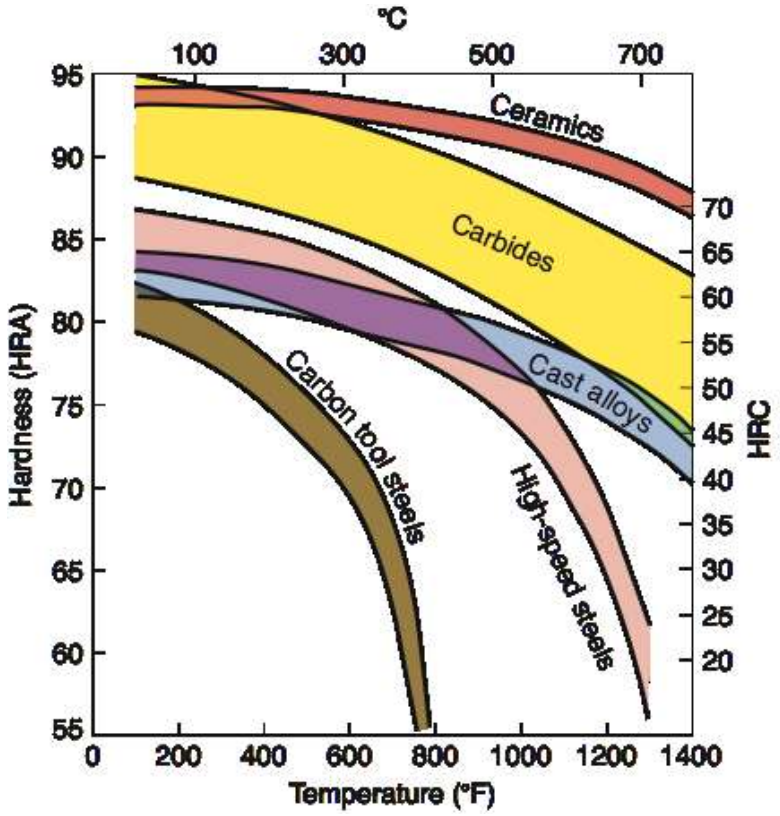

Figure 6. Hardness of a few cutting tool materials with respect to temperature (Reprinted from [12])

2.1.4 Applications

Cemented carbides are of great importance in the manufacturing industry. The unique combination of high hardness and good toughness gives rise to their extensive engineering and tooling applications. The highly wear resistant grades are used for machining and cutting of cast iron and nonferrous alloys. Non-cutting applications are also prevalent for cemented carbides such as mining, construction, structural components in machinery and wear resistance components.

2.2 TEXTURE

A material is polycrystalline when each of its grain is an individual crystal whose orientation differs from that of its neighbors. If all the grains are differently oriented with respect to one another and there is no commonality of orientation between them, the polycrystalline material is called a “random” material. If all the grains have the same orientation, there would be no grain boundaries, since grain boundaries, by definition, originate due to the orientation difference between adjoining crystals. Such a material would be a single crystal.

2.2.1 Description of Texture

A “textured” material is a polycrystalline material in which some of the individual crystals or grains may have nearly the same orientation, while the others may possess a host of different orientations. Since texture is a statistical concept, a material can be said to be strongly textured when 30-40% of its grains have similar orientations [13].

Texture can be described as the preferred orientation of grains (individual crystals) relative to a sample reference frame. Figure 7 (a) and (b) depicts microstructure of polycrystalline materials without and with texture respectively. The colors and arrows in the figure depict the orientation and a certain crystal plane normal (for example, <111>) of individual crystals (grains).

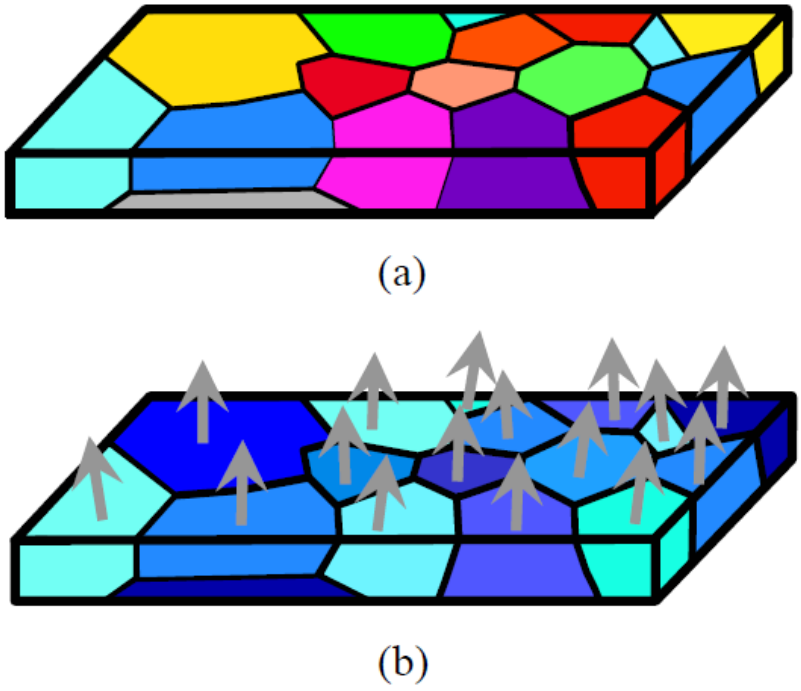

Figure 7. Schematic illustration of grain orientation texture. Similar grain colors depict texture. (a) Polycrystalline material without texture, (b) polycrystalline material with texture [9].

2.2.2 Representation of Texture

In the previous section, texture has been described as a statistical measure of the orientation of grains in a material without any thought about the location of any particular grain or group of grains. This can be said to be a macroscopic phenomenon and can be termed as "global" texture. However, texture can also have a microscopic meaning that includes measuring the orientation of each grain in a group of grains of a particular material. This kind of measurement could be termed as "local" texture. The two situations are depicted in Figure 8. X-ray diffraction (XRD) is generally used to obtain details on

global texture whereas electron backscatter diffraction (EBSD) is generally used for obtaining details about local texture in a particular group of grains of a material. To an extent, texture is also a function of the area used for data acquisition. A very small area could show lesser dominance of a particular orientation compared to a larger area of the same sample. This could be due to the localized presence of the particular orientation in other regions of the sample that were not considered while data acquisition from the very small area of the sample.

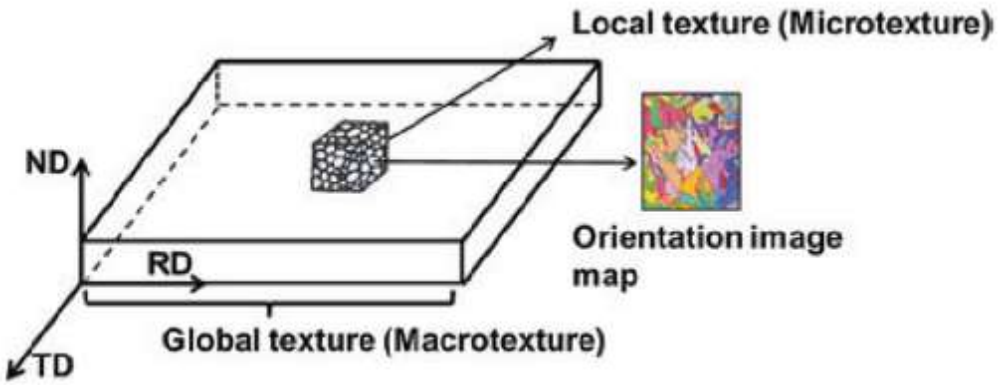

Figure 8. Schematic of the differences in local and global texture [14].

Three commonly used methods of representing texture are described in the following sections: the pole figure method, the inverse pole figure method and the orientation distribution function (ODF) method.

2.2.2.1 Pole Figure Method

A pole figure is the graphical representation of the orientation of objects in space. In the form of two-dimensional stereographic projections, pole figures plot the positions and intensities of specific crystallographic orientations in relation to the specimen geometry [13]. A pole figure shows the position of a crystal plane normal (pole) relative to the sample reference frame. A particular pole is plotted in a pole figure from all the crystallites in a polycrystalline material as shown in Figure 9. For a polycrystalline material with a large number of grains, poles may overlap so that the true orientation density in not truly represented. In such a case, contours can be used instead. Regions of high pole density have a high number of contours, while regions with low pole density have a few, greatly spaced contours.

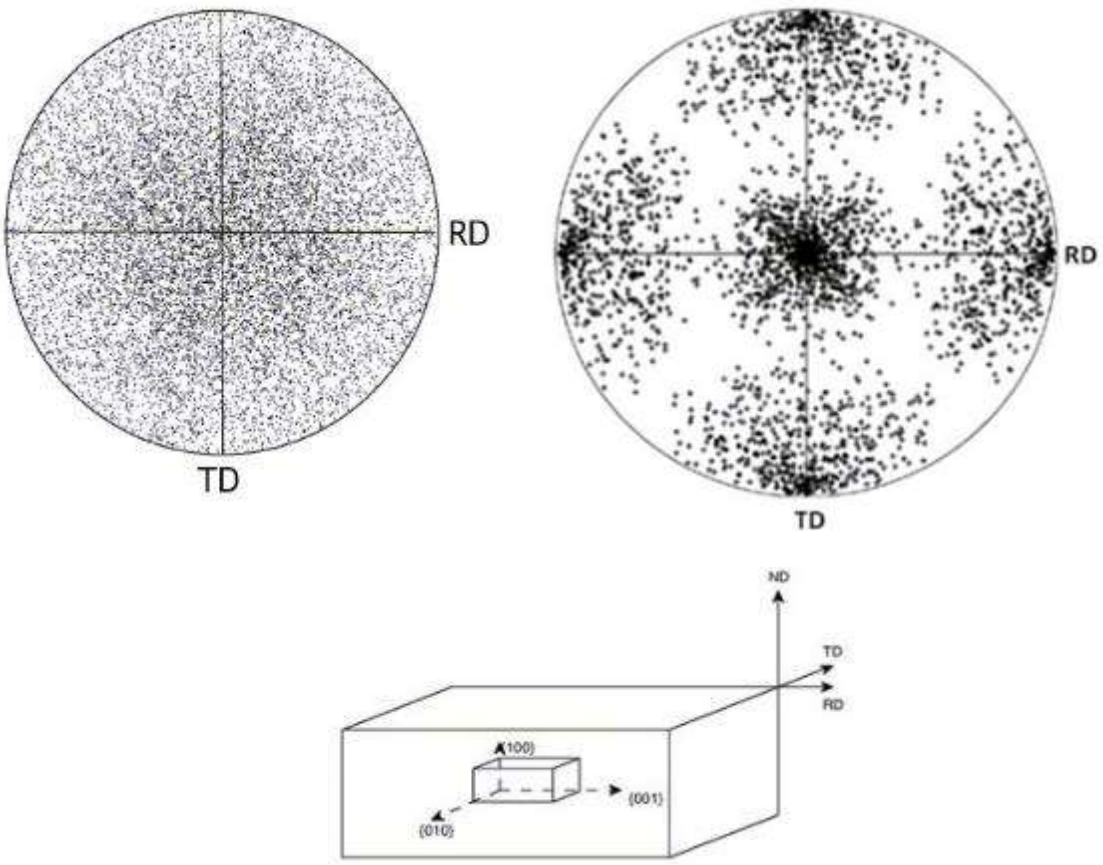

Figure 9. A {100} pole figure for a polycrystalline material showing random orientation (Left) and a {100} pole figure for a materials whose crystals are aligned with the rolling direction (RD), the transverse direction (TD), and the normal direction (ND) (Right). [15].

2.2.2.2 Inverse Pole Figure Method

An inverse pole figure (IPF) is the opposite of a PF. An IPF shows the position of a sample direction relative to the crystal reference frame. For a rolled sample, a rolling direction IPF will help to understand which crystal directions (or crystal plane normal) in a polycrystalline material are most likely parallel to the rolling direction (RD). Due to

symmetry in a crystal, a complete IPF contains many areas where the same information is repeated. Hence, only a standard stereographic triangle is generally plotted.

For example, 24 unit triangles are crystallographically similar for cubic crystal symmetry in a wire as shown in Figure 10 (a). Therefore, Figure 10 (b) which represents the data over 1/24th of the complete stereographic projection is sufficient for inverse pole figure representation. Figure 10 (b) shows the 001 inverse pole figure for the wire axis. Here, the contour lines show the frequency with which the wire axis coincides with the crystallographic axes, ⟨100⟩, ⟨110⟩, and ⟨111⟩. The figure shows that most of the grains have their ⟨101⟩ axis nearly aligned toward the wire axis [13].

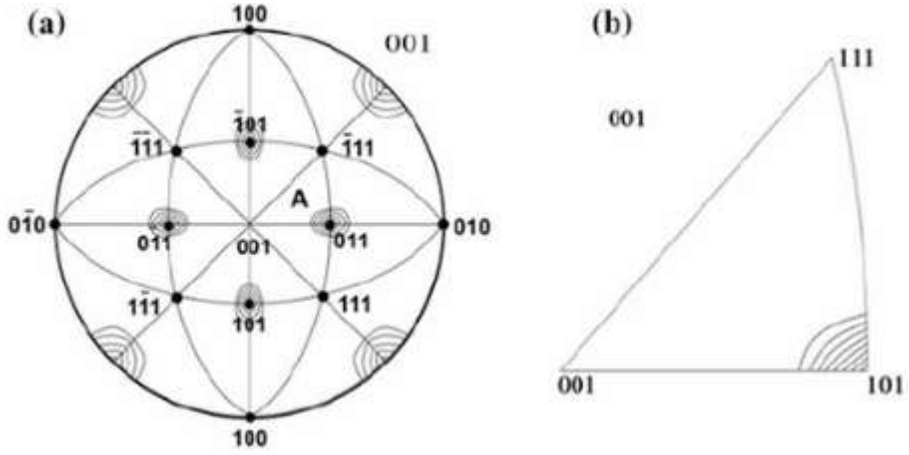

Figure 10. (a) A complete 001 inverse pole figure, showing ⟨110⟩ parallel to the wire axis, superimposed on a standard (001) stereogram. (b) A unit stereographic triangle is separated out [13].

2.2.2.3 Orientation Distribution Function (ODF) Method

Although, pole figures and inverse pole figures provide a useful description of the texture in a material, information that could be obtained from them is insufficient and at best semi-quantitative. This is because the crystal is a three-dimensional entity and pole figure and inverse pole figures use only two angles to describe the orientation distribution leading to lower resolution. Orientation distribution function (ODF) is used to mitigate these problems.

The orientation distribution function is a mathematical function that describes the frequency of occurrence of particular crystal orientations in a three-dimensional Euler space whose coordinates are defined by three Euler angles. For polycrystalline materials, the orientation of grains is described using the sample (or laboratory) reference frame and the crystal reference frame (see Figure 11). Euler angles are the three angles used for transforming the sample reference frame to the crystal reference frame.

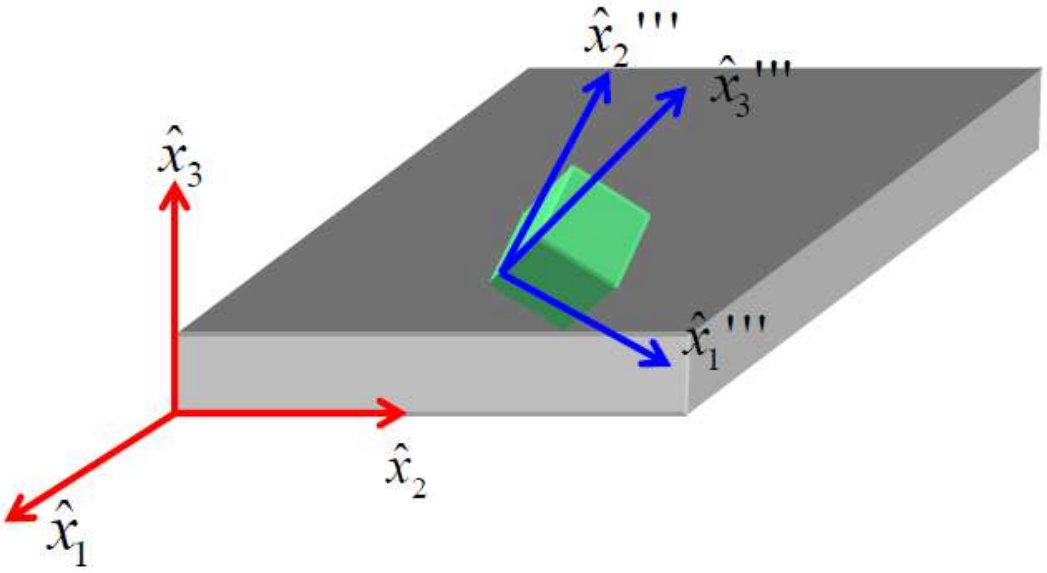

Figure 11. Illustration of the sample reference frame (red) and the crystal reference frame (blue). $\hat{x}_i$, $\hat{x}_i'''$ represent vectors in the sample and crystal reference frames, respectively [9].

Euler angles given in Bunge's notation by (ϕ_1, Φ, ϕ_2) define a sequence of rotation from one reference frame to another. If $\hat{x}_i$ denotes a basis unit vector in sample coordinates, using three consecutive rotations, we can obtain $\hat{x}_i'''$- a basis unit vector in crystal coordinates (see Figure 12). In Figure 12, $\hat{x}_i'$ and $\hat{x}_i''$ denote basis unit vectors in intermediate coordinates between the sample and crystal reference frame.

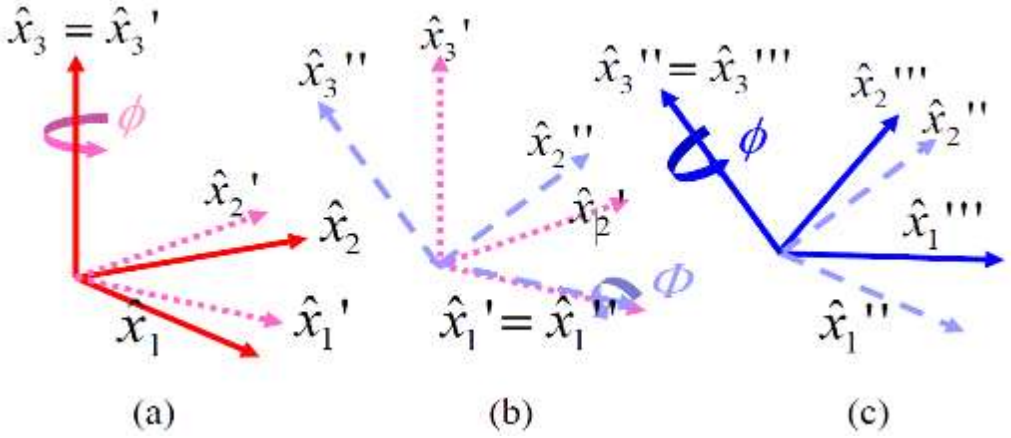

Figure 12. Schematic representation of transformation from the sample (red) reference frame to crystal (blue) reference frame. (a) Rotation from the sample reference frame, $\hat{x}_i$, to a new reference frame, $\hat{x}_i'$ (pink), (b) rotation from $\hat{x}_i'$ to another new reference frame, $\hat{x}_i''$ (purple), (c) rotation from $\hat{x}_i''$ to the crystal reference frame, $\hat{x}_i'''$ [9].

Texture is generally quantified in units of a multiple of a random distribution (MRD). ODF describes the orientation texture by specifying the Euler rotation angles that transform the sample reference frame to the crystal reference frame. Using Euler space (see Figure 13), each orientation can be uniquely represented by a single point.

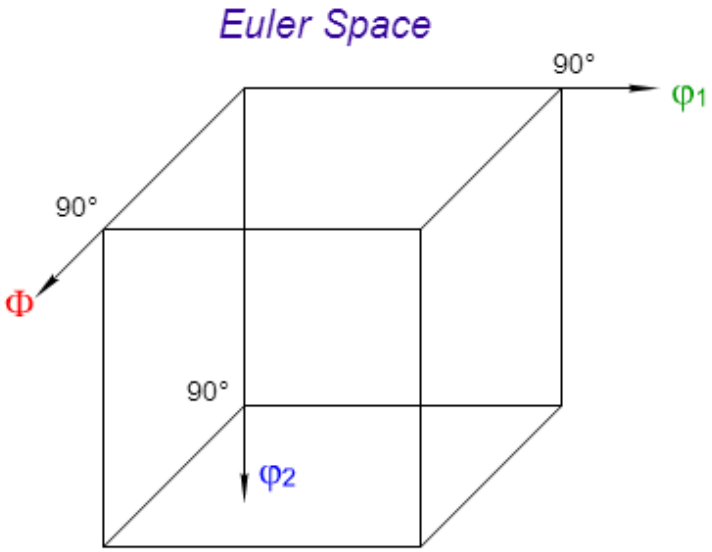

Figure 13. Representation of Euler space in three dimensions [16].

Since 3D graphs are not always easy to interpret, an ODF is generally used. ODF is the 2D representation of this 3D space by dividing the Euler space into slices at fixed intervals. The ODF is then shown in each of these slices for easier interpretation of the data as shown in Figure 14.

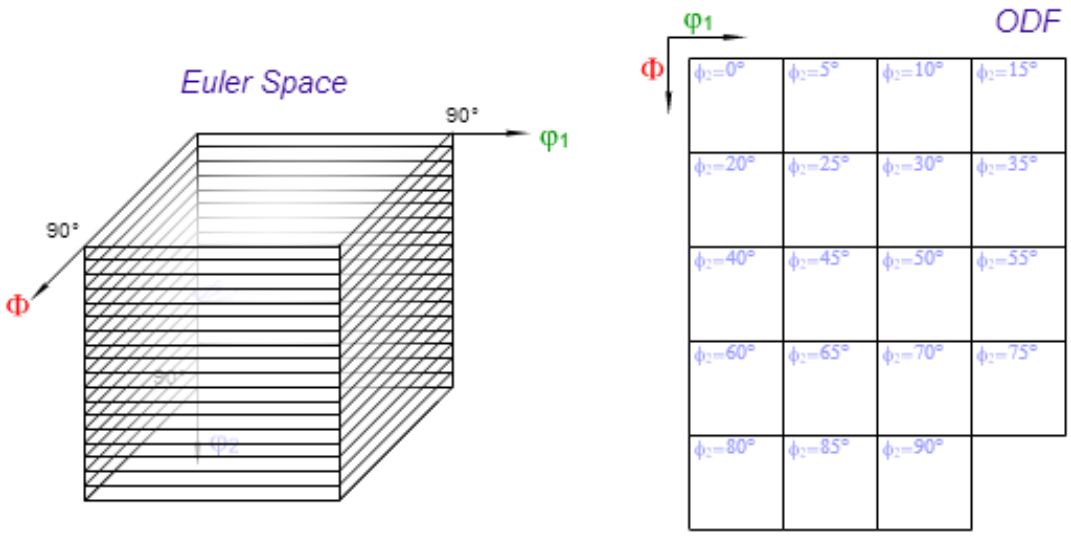

Figure 14. Slicing of Euler space at ϕ_2=5° intervals (Left), Arrangement of slices a grid known as ODF (Right) [16].

2.2.3 Development of Texture

Texture development in polycrystalline materials occurs in almost every stage of materials processing and it very difficult to avoid texture completely at any stage of processing. Metals and alloys possess texture even in the cast state. In addition, texture modification occurs during further processing which includes hot deformation, cold deformation and annealing. Texture development also takes place during other processes like powder metallurgy, electrodeposition and thin film deposition techniques. Nonmetallic materials such as ceramics, composites and polymers also develop texture during the different stages of manufacturing.

Texture in materials can be classified into four different types based on the processing technique: (1) solidification texture, (2) transformation textures, (3)

deformation texture, and (4) recrystallization (annealing) texture. They are described briefly in the following sections.

2.2.3.1 Solidification Texture

Melting and casting of materials leads to textured grains in certain regions of the casting and the texture obtained is called solidification texture. In pure solids, the texture obtained is completely columnar when solidification occurs a very slow rate without much turbulence. On the other hand, alloys develop mostly equiaxed textures under certain conditions. During the solidification process, shape and texture of the grains will depend on whether is a condition favoring growth of existing grains or nucleation of new grains. Thus, solidification texture can be controlled during casting by changing the solidification conditions or the chemistry of the material.

2.2.3.2 Transformation Texture

Solidification texture is formed during a liquid-solid transformation. The texture of this newly formed solid can further change when the solid further cools down due to phase transformation. In solid-state phase transformation, the crystals (grains) of the product phase generally have different crystal symmetry compared to the parent phase. If the parent material is textured, then the product material also acquired a texture that is related to the texture of the parent material. This texture is called transformation texture, which can also occur during thermomechanical processes, when a material is hot worked in a phase field.

2.2.3.3 Deformation Texture

The most important texture developments occur during plastic deformation and recrystallization that follows the deformation [17]. The nature of the deformation texture depends on the crystal structure and flow characteristics of a given material. For example, hot rolled aluminum is seen to have sharper texture than cold rolled aluminum [17]. This phenomenon can be attributed to better flow rates achieved during hot rolling. At times, the initial texture due to solidification also plays a role in the nature of the deformation texture [18].

In industrial practice, rolling is the most commonly used method for plastic deformation. Among the different crystal structures, hexagonal close-packed (HCP) materials show a wider variety of rolling textures compared to face centered cubic (FCC) or body centered cubic (BCC) metals. The observed rolling textures in HCP materials depends on their c/a ratio and the slipping and/or twinning modes [13].

Other deformation methods include uniaxial plastic deformation due to tension, compression, or extrusion that generally lead to textures that are of fiber type. Nonetheless, in some cases, unusual textures have been observed. For example, in a magnesium alloy subjected to extrusion, unusual basal texture was observed [19]. This texture was attributed to the high extrusion ratio and dynamic recrystallization. In dynamic recrystallization, as opposed to static recrystallization, the nucleation and growth of new grains occurs during deformation rather than afterwards as part of a separate heat treatment. In the recent past, texture development due to shear induced plastic deformation has been studied [13].

2.2.3.4 Recrystallization (Annealing) Texture

During annealing, three fundamental structural processes termed as (a) recovery, (b) recrystallization, and (c) grain growth take place. Recovery includes all the phenomena that occur before the appearance of new strain-free grains. Recrystallization includes the phenomena of nucleation and growth of these strain-free grains and the gradual consumption of the cold-worked matrix. When the deformed matrix has completely transformed into an aggregate of small strain-free grains, there may be a competition between the grains to grow, based on their sizes or orientations. This phenomenon is called grain growth.

The annealing processes described above give rise to changes in the crystal orientation or texture of different materials [18, 20] and the texture so obtained is called recrystallization texture. Recrystallization texture depends on the rate of nucleation, the immediate environment of the nuclei, and the nature, energy, and mobility of boundaries between grains of different orientations. The recrystallization texture will also depends on the starting texture of the material before deformation, the amount of strain during deformation, the purity of the material, and the extent of grain growth that occurs after primary recrystallization.

2.2.3.5 Other Methods

A combination of different solidification, solid-state transformation and plastic deformation methods have been used to obtain textured metals and alloys. Methods combining rolling and shear such as equal angular channel rolling (ECAR) and asymmetric rolling have been used with silicon steels [21], aluminum alloys [22] and

magnesium alloys [23] to obtain a high degree of texture. A method called twin roll casting combines a solidification process (casting) and a plastic deformation process (rolling) and is used to obtain textured silicon steel [24]. A severe plastic deformation method called half channel angular extrusion has been observed to reduce the degree of texture obtained after rolling in a magnesium alloy [25]. Finally, other methods like large strain extrusion machining and friction stir welding have also been used to obtain textured metals and alloys [26-29]. For tungsten carbide-cobalt composites, an orientation textured surface has been obtained by using large (average size-0.5mm) and oriented WC crystals. These crystals were placed on the surface an non-textured sample using a stereomicroscope [4]. However, no significant orientation-texture has been observed using any post-processing method.

2.3 Fabrication of Cemented Carbides

Cemented carbides are composed of a metal matrix composite where carbide particles act as the aggregate and a metallic binder (for example, cobalt) serves as the matrix. Since they have very high melting temperatures, it is quite impractical to fabricate carbide parts by casting. Powder metallurgy is generally used for combining the carbide particles with the binder (matrix) as the properties obtained are very high and unparalleled compared to other fabrication methods [30].

Consolidation of the powders can be in the form of sintering and/or compaction. Sintering is defined as the bonding of particle packing into a coherent, predominantly solid structure by the application of heat to enable one or more mechanisms of atomic

movement to the particle contact interface to occur [31]. Whereas, compaction is the process of condensing powder by application of pressure.

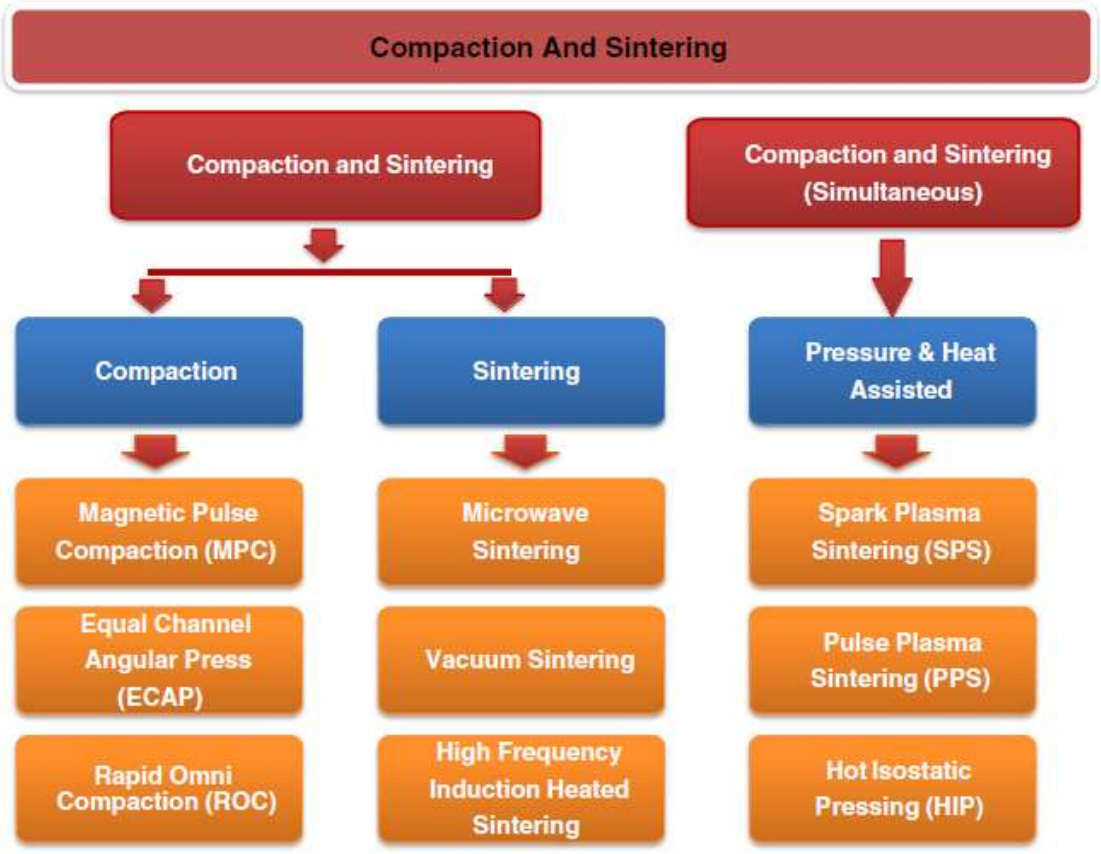

Figure 15. Classification of compaction and sintering processes. For SPS, PPS and HIP, it possible to compact and sinter the powders separately [30].

The classification of consolidation techniques is shown in Figure 15. Amongst these techniques, spark plasma sintering (SPS) is one of the most widely used techniques for the consolidation of cemented carbides. It involves simultaneous application of heat and pressure. It also includes the application of rapid heating which results in the

bypassing of low temperature regions where surface transport controlled sintering is dominant. This results in rapid material compaction without excessive grain growth. Since grain size is known to have a direct relationship to the properties of cemented carbides [9, 31, 32], SPS was selected as the technique for consolidation in this thesis.

2.3.1 Spark Plasma Sintering

Spark plasma sintering (SPS), also known as field assisted sintering technology (FAST) or pulsed electric current sintering (PECS) is a sintering technique utilizing uniaxial force and a pulsed (on-off) direct electrical current (DC) under low atmospheric pressure to perform high speed consolidation of the powder.

2.3.1.1 Basic System Configuration of SPS

A schematic of the SPS system is shown in Figure 16. The system consists of a sintering machine with vertical axis pressurization and a vacuum and water cooling chamber, a DC pulse generator and a sintering controller. The powder mixture is directly loaded between a graphite die and graphite punches on the stage in the chamber and held between electrodes.

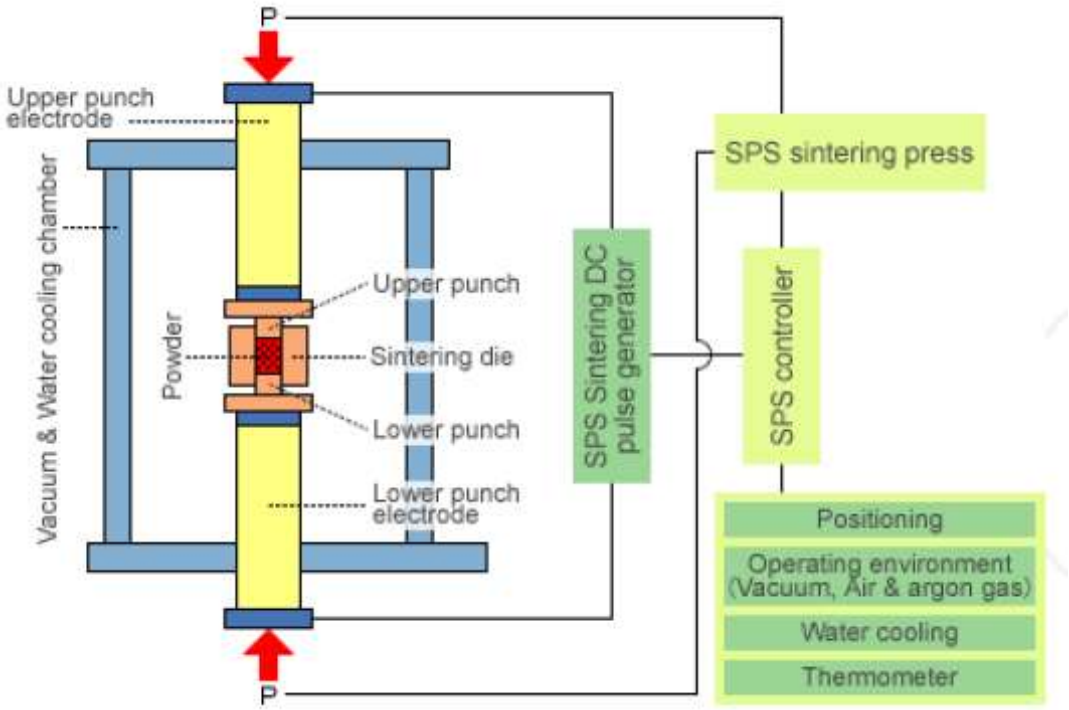

Figure 16. Schematic of the SPS system [33].

The pressure on the powder can be constant or increased gradually. Pulse discharge is normally achieved by the application of a voltage of about 30V and a current of 600-1000A. The duration of each pulse can be varied between 1-300ms [34]. Heating rates of about 1000°C/min can be achieved depending upon the shape, thermal properties and electrical properties of the sample as well the electric power. Such high heating rates reduce the processing time to merely a few minutes.

2.3.1.2 Principles and Mechanism of SPS

The basic mechanisms of neck formation during SPS are shown in Figure 17, even though the details of for these processes are still being debated. The occurrence of a plasma discharge is primarily debated, but it is widely accepted that occasional electric discharges may take place on a microscopic level [33]. The electric current and force lead to the microscopic electric discharge, which accelerates material diffusion. Since very weak or no current passes through non-conducting samples, the discharge originates from the electric field of the pulsed current used. The intensity of this discharge depends not only on the electric current but also on particle size, pore size and density of the green compact. The exact role of the current is not clearly known. The conductive powders are heated owing to the Joule effect due to the current. Non-conducting powders are heated due to the heat transfer from the die and punches.

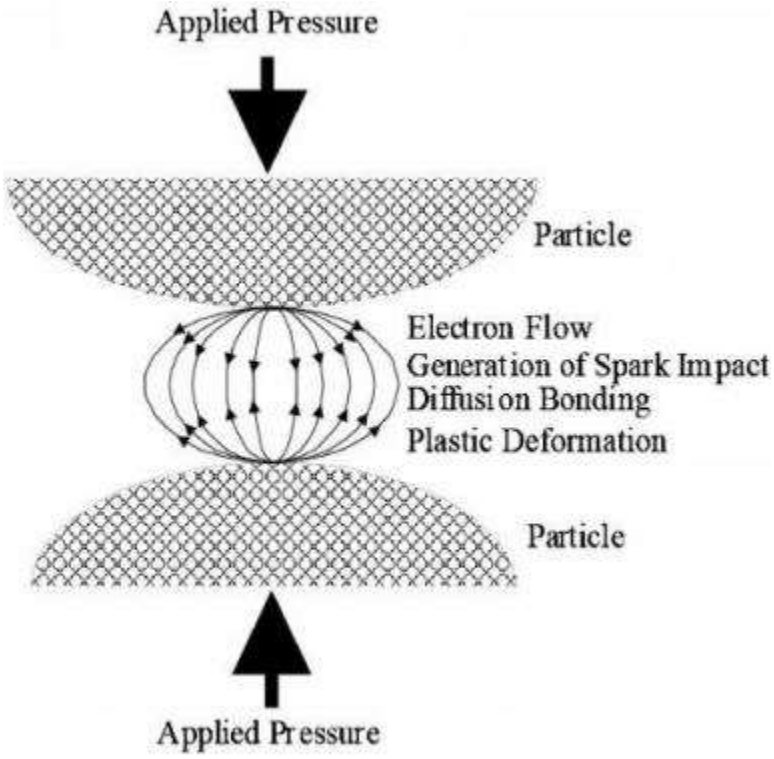

Figure 17. Basic mechanisms of particle contact neck formation [31].

SPS offers many advantages over conventional sintering processes, including ease of operation and accurate control of sintering energy as well as high sintering speed, high reproducibility, safety and reliability [33]. SPS can also offer a very small grain size while still achieving full densification. Temperature and pressure are the two parameters of SPS which significantly affect densification [35].

2.4 TEXTURE - PROPERTY RELATIONSHIPS OF CEMENTED CARBIDES

Tungsten carbide grain size and contiguity of the carbide phase are parameters known to predominantly affect hardness and toughness of cemented carbides [9].

Kim et al. have shown (through simulations) that the young's modulus also depends on the texture of tungsten carbide grains. In Figure 18, the dotted horizontal line shows the experimentally measured modulus of the material with no orientation texture. In the case of the [100] textured sample, the modulus along the c-axis direction ($[010]^S$) is invariably higher than the modulus of the randomly textured material, and the modulus along the direction perpendicular to the c axis ($[100]^S$) is lower than the randomly textured value.

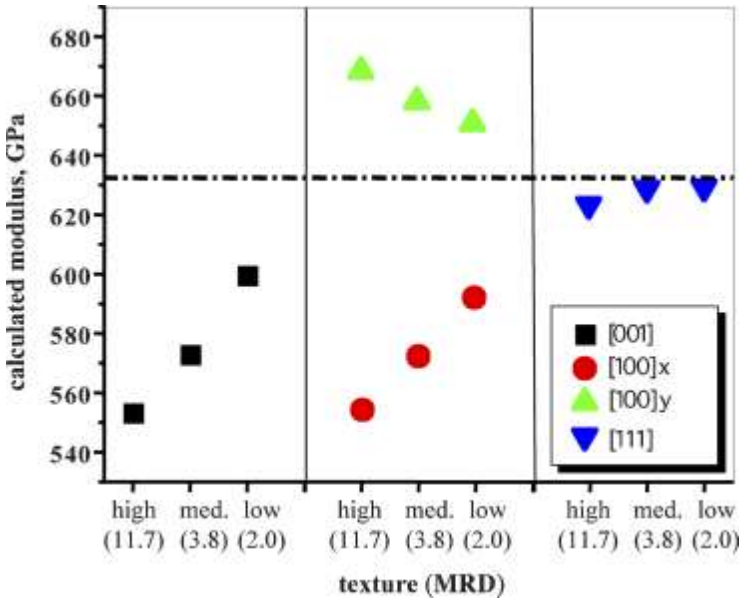

Figure 18. Calculated elastic modulus for hypothetical cemented carbide samples with [001], [100], and [111] orientation textures. The dotted line indicates the experimentally measured modulus of a randomly textured sample. As the sample becomes less textured (the multiples of a random distribution [MRD] value decreases), the calculated modulus approaches the experimentally measured modulus. In the legend, x denotes elongation in the $[100]^S$ direction and y denotes elongation in the $[010]^S$ direction [3].

Fracture strength simulations (using a combination of mechanical and thermal load) have shown that cemented carbide sample could be strengthened between 2% and 13% by texturing the sample in the [001] or [100] directions (Figure 19) [3].

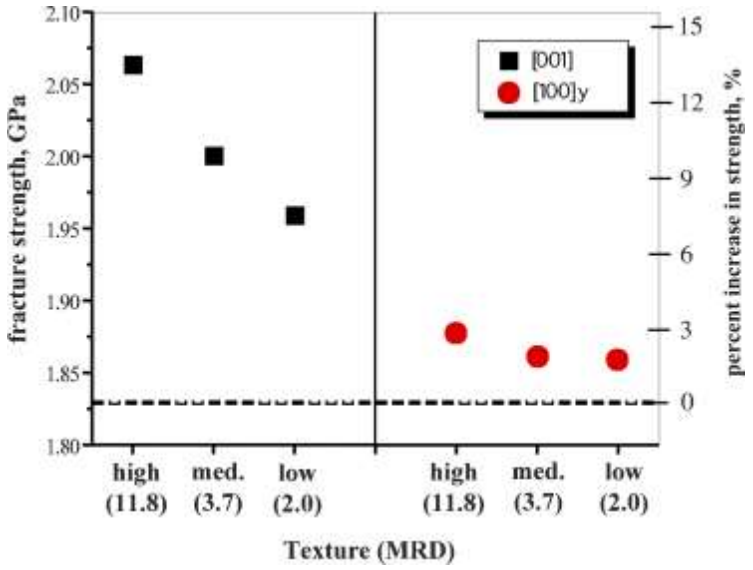

Figure 19. Calculated fracture strength (left ordinate) and fracture strength increase (right ordinate) for [001] and [100] orientation textures. The dotted line represents the calculated strength of the real microstructure with no texture [3].

Modeling studies have shown that the change of the shape of WC crystals to a flatter triangular prism could increase the hardness of WC–Ni cemented carbides by 8–15% [36]. For tungsten carbide crystals, it has also been shown that the measured hardness value is about 1.6 times higher on the basal planes than on prismatic planes [1, 2].

3. RESEARCH METHODOLOGY

The objective of this research work is to develop and evaluate a fabrication procedure that enables a degree of control over the surface and sub-surface grain orientation texture of spark plasma sintered carbides, and to investigate its effects on the hardness and abrasive resistance of the material. This chapter outlines the research methodology that was used for achieving this objective. In addition to the research questions, this chapter lists their associated tasks, methodology and outputs.

In order to obtain control over grain orientation texture of WC-Co composites and study its effect on the hardness and abrasion resistance properties of the material, two research questions (RQs) are asked:

3.1 What are the Parameters for Achieving Dominant Grain Orientation Texture in Sintered WC-Co Bulk Composites? (RQ 1)

The objective of RQ1 is to develop and evaluate a viable procedure that allows a degree of control over the grain orientation texture of WC-Co composites, and confirm evidence of a dominant orientation texture. The tasks, methodology and outputs for RQ1 are listed below:

Task 1A**:** Develop and refine a procedure for obtaining strong texture in WC-Co samples.

Task 1B: Characterize the morphology and confirm evidence of dominant texture in material.

Methodology**:** Two uniform WC-10%Co mixtures are obtained by mixing two types of tungsten carbide (WC) powders (of two different grain sizes) with cobalt (Co) powder. Each of the WC-Co mixture is combined with a binder & plasticizer to obtain a thick paste, which is then rolled into thin sheets. Discs are cut out from the rolled sheets, which are then stacked and subjected to thermal debinding. After debinding the discs, they are subjected to spark plasma sintering. The texture of the sintered WC-Co samples is studied using X-ray diffraction (XRD) and electron backscatter diffraction (EBSD).

Outputs: The major output from these tasks will be the development of a scalable procedure that is viable to obtain textured WC-Co sheets (coatings) or bulk composites.

3.2 What is the Effect of Grain Orientation Texture on the Hardness and Abrasive Resistance of Sintered WC-Co Composites? (RQ2)

The objective of RQ2 is to subject the textured WC-Co sample to hardness and other mechanical characterization testing to evaluate the correlation between the dominant texture of WC grains and the hardness and abrasion resistance of the WC-Co bulk composites. The tasks, methodology and outputs for RQ2 are listed below:

Task 2A: Subject the WC-Co samples to mechanical characterization tests.

Task 2B: Evaluate the hardness and abrasion resistance and wear quantification through metallographic evaluation.

Methodology: Appropriate sections of the sintered WC-Co bulk samples are subjected to nano-indentation and scratch tests. These samples are then evaluated using a scanning electron microscope (SEM) and related EDX, interferometry, and an optical microscope to study the details about the wear of the samples.

Outputs: The major outputs from the tasks listed in RQ2 will be evaluation of the effect of orientation texture on the hardness and abrasion resistance and the realization of the potential to use this procedure for reliably texturing bulk/sheet hard-material composites.

3.3 SUMMARY

For an organized view of the research methodology, a summary of the two research questions, and their associated tasks, and outputs is outlined in Figure 20.

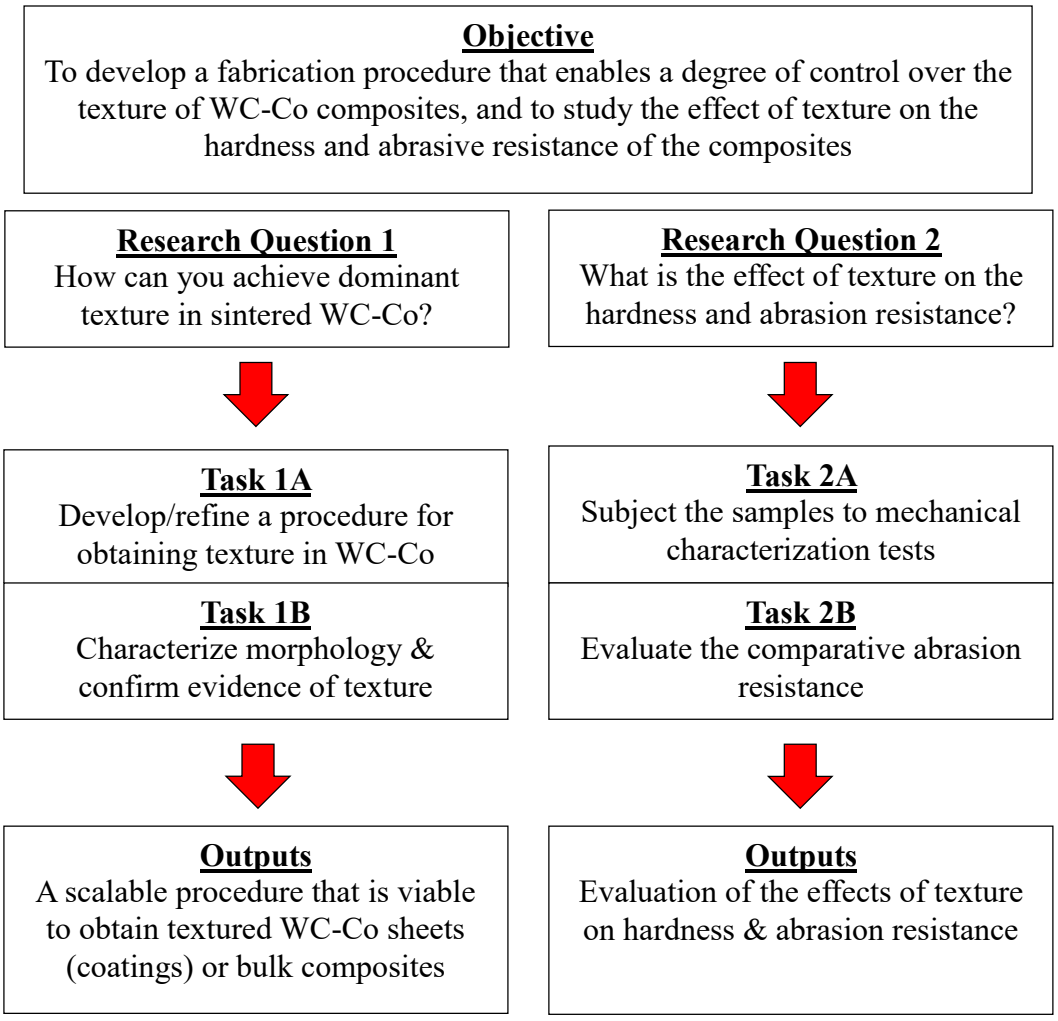

Figure 20. Flowchart summarizing the research methodology used in this thesis

4. ACHIEVING DOMINANT GRAIN ORIENTATION TEXTURE IN SINTERED WC-CO (RQ1)

This chapter answers research question 1 (RQ1), i.e., "What are the parameters for achieving dominant grain orientation texture in sintered WC-Co bulk composites?" It details the procedure that would allow a certain degree of control over the grain orientation texture of WC grains in a WC-Co composite. Additionally, it elaborates on the methods used to confirm the presence of a dominant grain orientation texture.

4.1 Previous Efforts on Texturing Bulk Composites

An extrusion-spark plasma sintering process has been used to obtain textured bulk zinc oxide (ZnO) ceramics [37]. This method involved kneading a dough of ZnO powder, a binder, a plasticizer, and a lubricant for extrusion into sheets as shown in Figure 21. After stacking the sheets along the extrusion direction, round pieces were cutoff and subjected to debinding in open air. A spark plasma sintering (SPS) machine was used to sinter the debonded round sheets. The direction for sintering of the round sheets is shown in Figure 22.

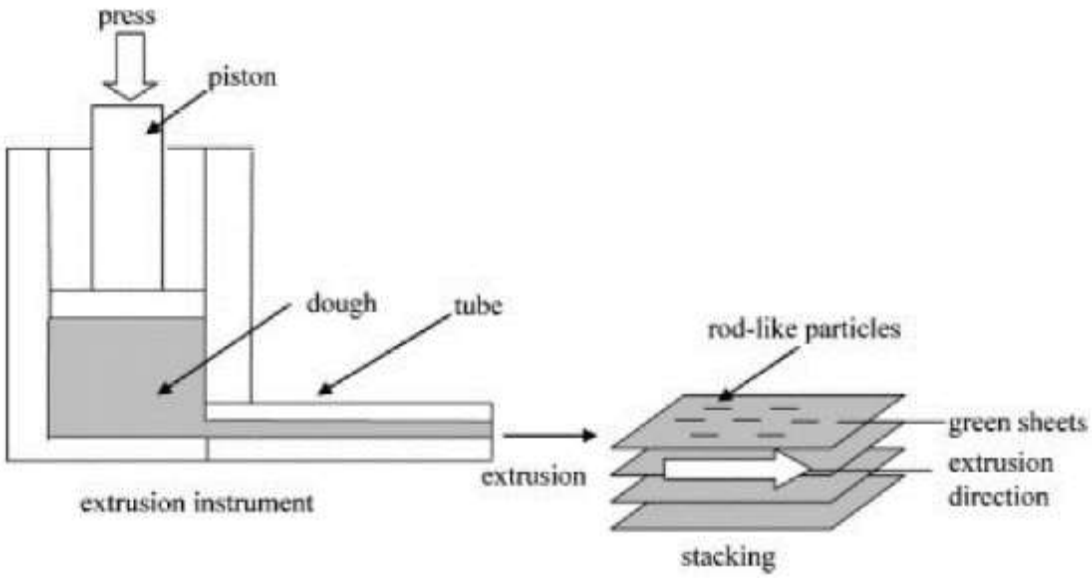

Figure 21. Schematic illustration of extrusion procedure and stacking of green sheets following extrusion direction [37].

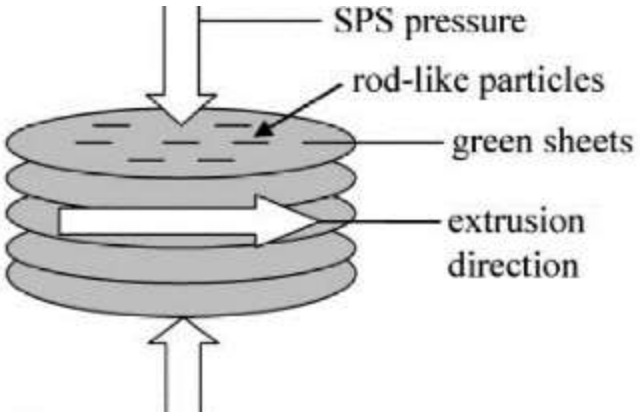

Figure 22. Illustration of round sheets subjected to SPS [37].

For bismuth-layer-structured ferroelectrics (BLSF), magnesium oxide (MgO) ceramics and $Ca_{0.85}(LiCe)_{0.075}Bi_4Ti_4O_{15}$ ceramics, a rolling-extended method utilizing templated grain growth (TGG) has been used to obtained orientation-textured samples

[38-40]. Templates are generally large plate-like crystals of the materials, which are mixed with the powdered materials, binder, plasticizer and lubricant. The mixture is then damp dried to obtain a clay-like dough. This dough is sandwiched between two separating films and rolling-extended into sheets as shown in Figure 23. The rolling-extension process is repeated until the desired thickness of the sheets is achieved. The sheets are then stamped out into disks. Disks piled on top of each other are subjected to pressure to achieve a cylindrical shape. The cylindrical green compacts are subjected to debinding and finally sintered to achieve the final orientation-textured product.

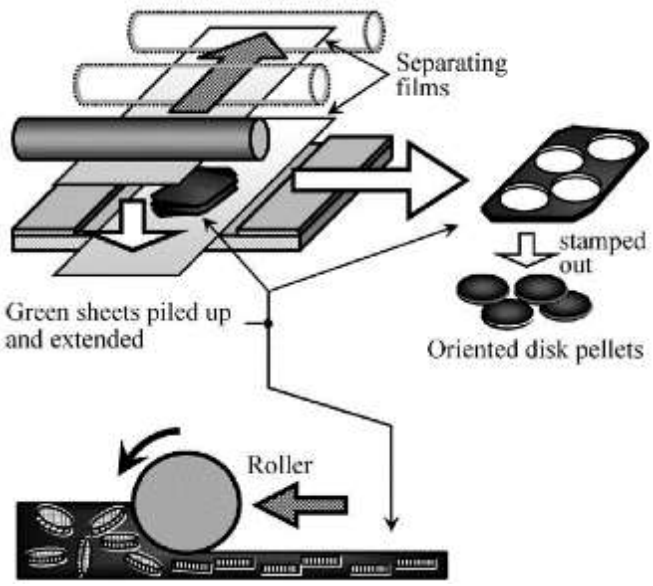

Figure 23. Illustration of the rolling-extended orientation method [38].

4.2 Development of the Procedure to Obtain Texture in WC-Co Composites

After a thorough literature review, various possible methods to obtain grain orientation texture in WC-Co composites were analyzed for feasibility and scalability. The rolling-extension method explained in section 4.1 was then developed and refined for WC-Co samples. Different options were considered for binding the WC-Co powder. The purpose of the binder is to make the WC-Co powder malleable enough to be drawn into thin sheets.

4.2.1 Rolling-extension using Paraffin Wax as a Binder (Type-1 Trials)

Figure 24 shows a preliminary sample that was made by mixing WC-10%Co powder with 5% (by weight) paraffin wax and rolling them at pressure of about 30 psi. The procedure planned using paraffin wax as binder is shown in Figure 25. When the sample is heated to about 40°C, it becomes quite malleable and hence, it could be easily drawn into thin sheets. However, the malleability of the sample was very sensitive with respect to temperature and slight over heating or under heating would create problems in rolling the sample. This would make the process very difficult to control on a large-scale production plant. The samples obtained were quite brittle. This made the further processing of the discs difficult unless they were subjected to heat. These issues lead to the rejection of paraffin wax as the binder for the rolling-extension process.

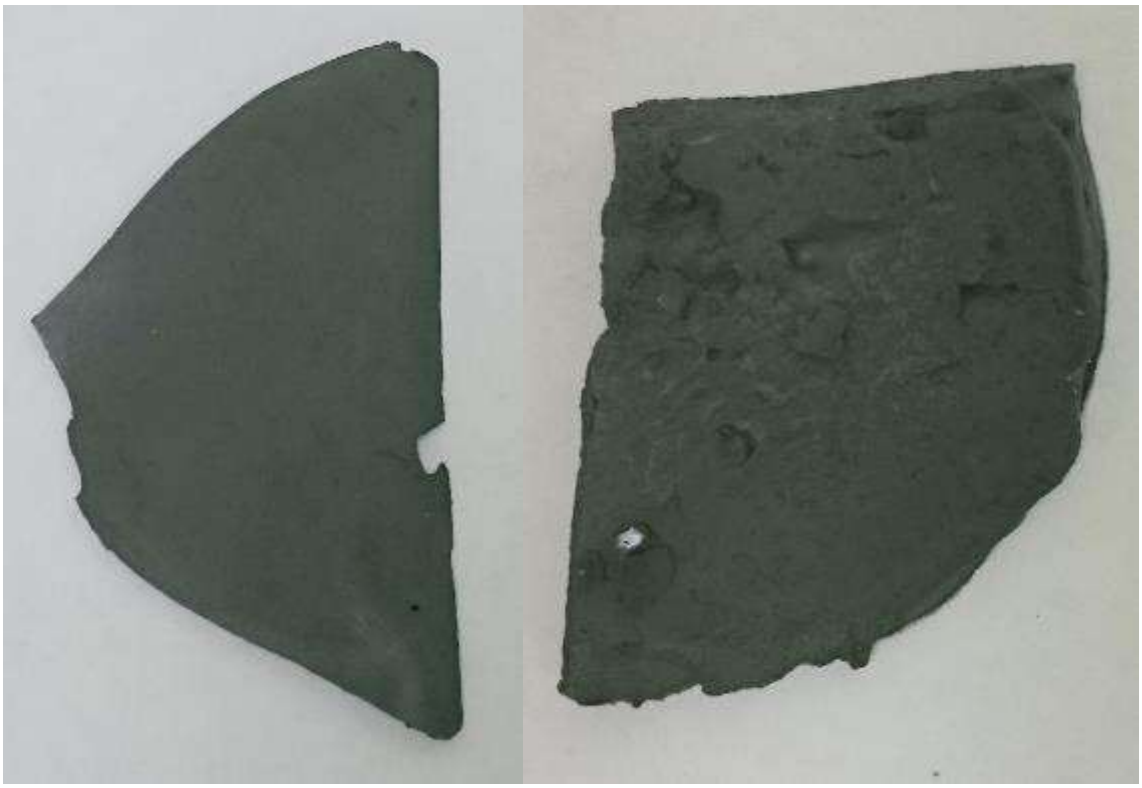

Figure 24. Rolled samples of WC-Co powder mixed with paraffin wax having approximate dimension of 50mm(length)*30mm(width)*1mm(thickness)

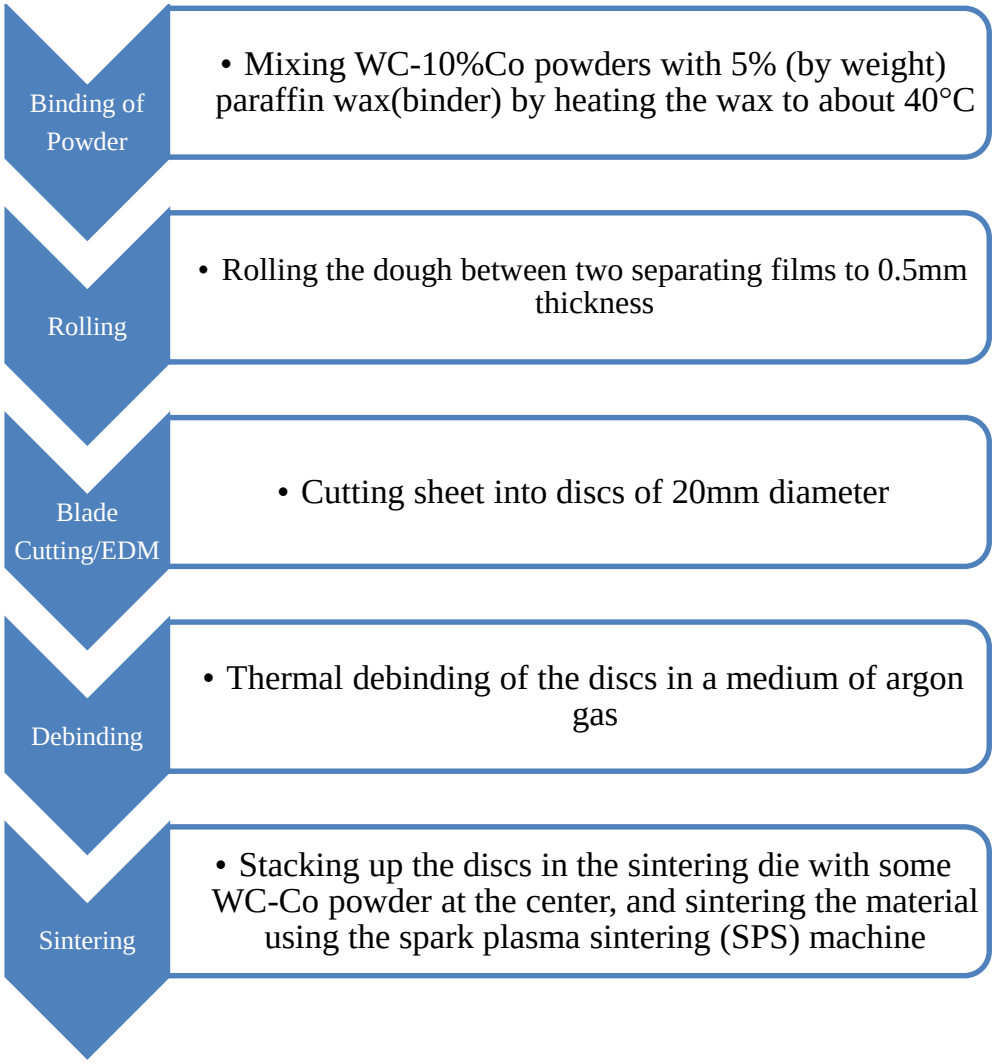

Figure 25. Flow chart of fabrication steps for the preliminary WC-Co sample with paraffin wax as a binder

4.2.2 Combination of a Binder, Plasticizer, & Lubricant for Rolling (Type-2 Trials)

Another combination of materials was tried to make the WC-Co powders malleable. This combination involved the use of polyvinyl alcohol (PVA) as a binder, glycerin as a plasticizer and liquid paraffin as a lubricant. The dough meant to be used for the rolling-extension process was prepared by mixing the WC-Co powders with 10% (by

weight) PVA, 3% (by weight) glycerin, and 2% (by weight) liquid paraffin which was used by Ning et al [37]. However, this dough was flaky and not very malleable. The dough would break apart when subjected to rolling under pressure. Hence, the procedure was further refined to resolve this issue of malleability and flakiness.

4.2.3 Final Procedure using Polyvinyl Alcohol as a Binder for Rolling (Type-3 Final)

A few trial samples were then made by mixing WC-10%Co powders with 20% (by weight) of a PVA solution in water. The PVA solution was prepared by mixing 20 grams of PVA in 100 grams of water. The PVA used is in the form of small pellets and is first mixed in cold water using a magnetic stirrer. After that, it is heated to a temperature of about 90°C while stirring continuously. The temperature is then kept constant at about 90°C until the PVA is mixed completely. The solution is then air cooled to room temperature to obtain a malleable dough.

The WC-10%Co powder is added to the water along with PVA pellets itself so as to achieve an even distribution of the powder in solution. If the WC-10% powder is added after making the PVA solution, there is an uneven distribution of the WC-Co powder which is shown in Figure 26. The samples were made using WC grains having average grain sizes 4 μm and 0.4 μm. The average grain size of the Co powder used is 0.5 μm.

Figure 26. Images of the preliminary dough where the WC-Co is not evenly dispersed in the PVA solution. The lighter (yellowish) regions in the dough are areas with lesser amount of the WC-Co powder. The samples had approximate dimensions of 30-40mm (length)*25-50mm (width)*1.5mm (thickness)

The refined method used for making the sample involved the following steps:

1. A uniform WC-10%Co mixture were obtained by mixing tungsten carbide (WC) powder with cobalt (Co) powder in a ratio of 9:1 (Figure 27). The WC and Co powders were mixed using a hand blender. For mixing the powders, wet ball milling is generally recommended to achieve an even 'coating' of cobalt over the tungsten carbide particles. However, wet ball milling requires the use of an organic solvent and it is essential to ensure the complete removal of the solvent after the ball milling. The possibility of contamination due to the addition of solvent was the reason why ball milling was not used. The WC powder had an average particle size of 4 μm. The Co particles had an average size of 0.5 μm. The morphology of the 4 μm WC powder is shown in Figure 28. It can be seen that the WC powder has a predominantly spherical

shape. The particles which have a size much larger than 4 μm are multiple WC particles which have adhered together.

Figure 27. Mixed WC-Co powder in the ratio 9:1 by weight. The WC powder has a dark gray color and the Co powder has a lighter gray color

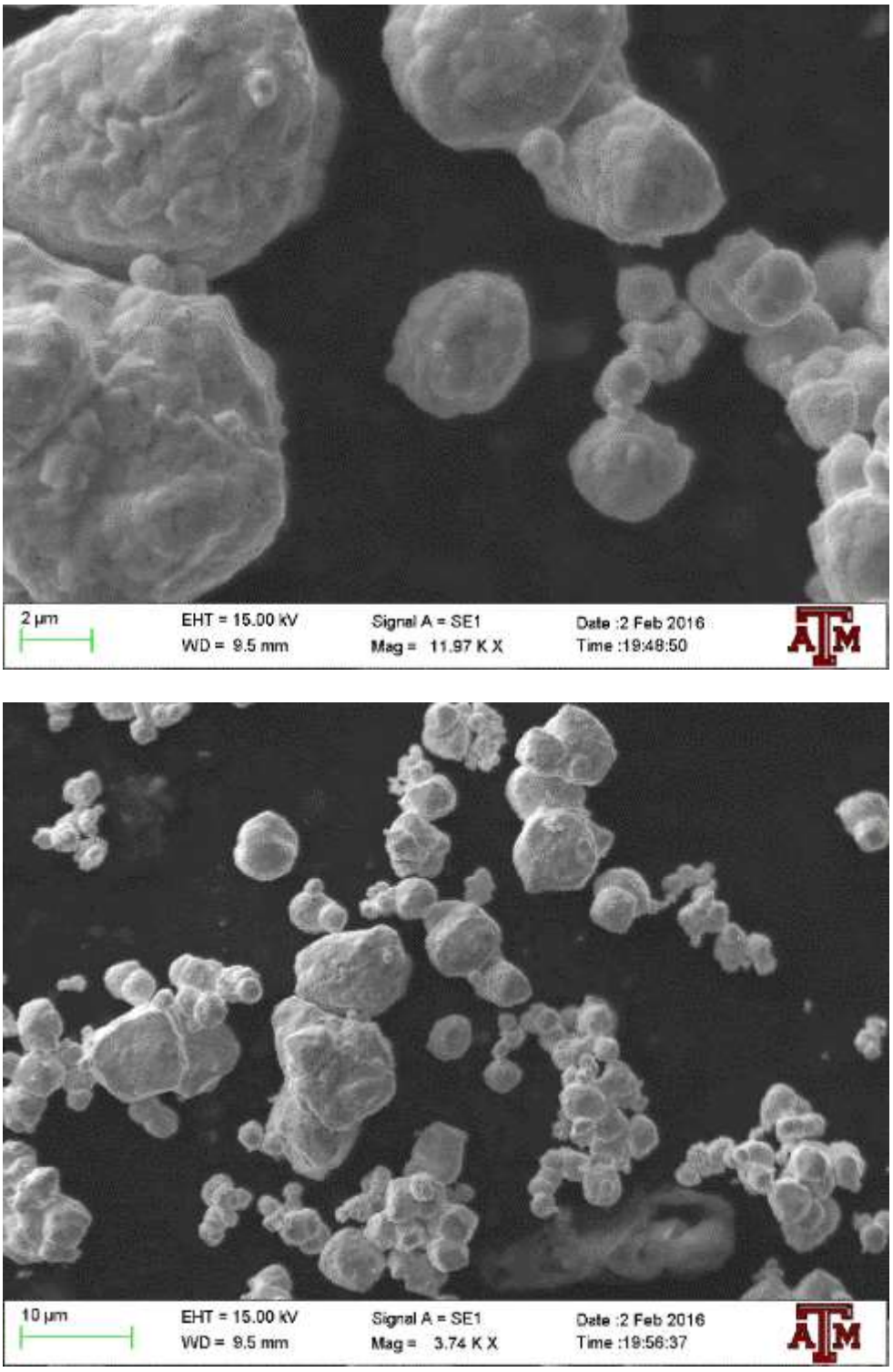

Figure 28. SEM images of the WC powder having average particle size of 4 µm (top image- at high magnification, and bottom image- at low magnification)

2. The dough for rolling was obtained by mixing the WC-10%Co mixture with the thick polyvinyl alcohol (PVA) paste in the weight ratio of 4:1. The PVA paste was a 20% solution of PVA in water and had high viscosity. (Note: Some of the WC-10%Co mixture was kept aside for later use.)
3. The doughs made of PVA paste and WC-Co particles was then damp-dried until it reached a clay-like softness.
4. The clay-like dough was placed between two separating films and rolling-extended into thin sheets. The rolling-extension process was accomplished by passing the dough multiple (8 to 10) times in between two rollers having a pressure of about 40 psi between them. Figure 29 shows the Cheminstruments Hot Melt Coater Laminator that was used for the process of rolling-extension. The sheets had a thickness between 0.5-0.8 mm as shown in Figure 30.

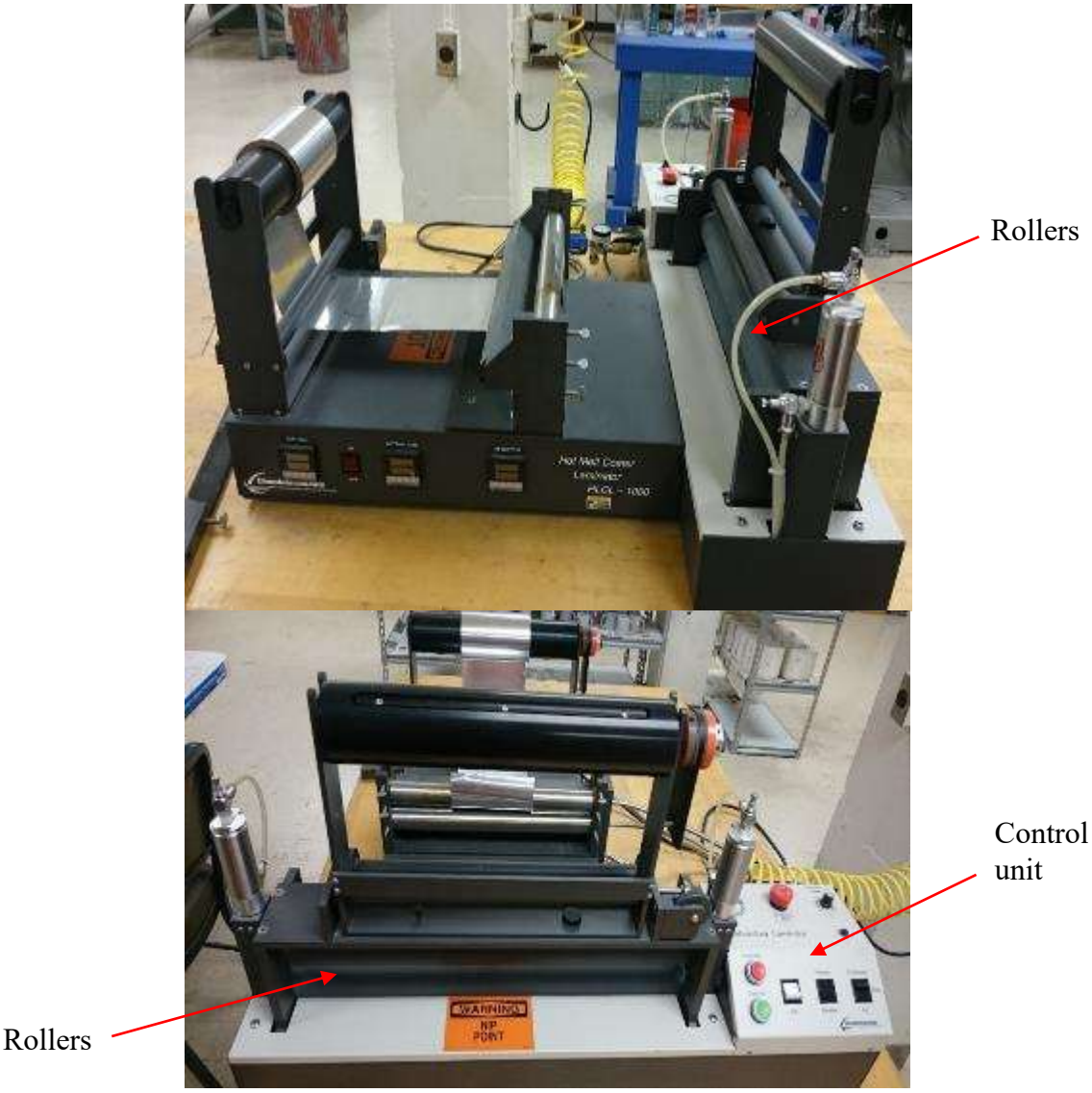

Figure 29. The equipment used for the rolling-extension of the bonded WC-Co dough. The control unit is used to control the movement of the rollers and the pressure between them.

Figure 30. Rolling-extended thin sheet having approximate dimensions of 230-245mm (length)*150-180mm (width)*0.5-0.8mm (thickness)

5. The rolled sheets were cut using a blade cutter into discs of diameter 20mm (Figure 31).
6. The discs were stacked up to get to get multiple columns of discs and wrapped in aluminum foil.

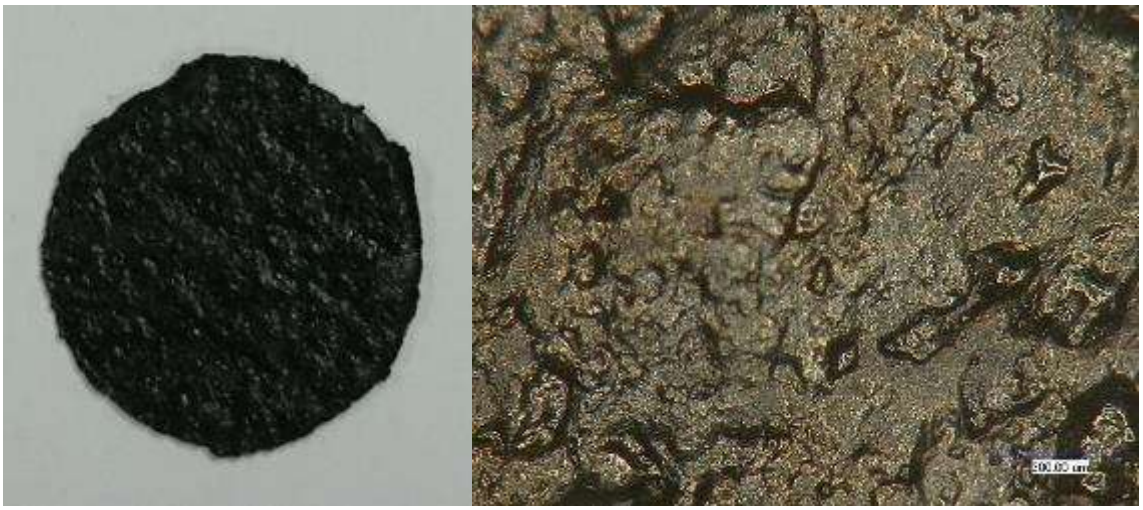

Figure 31. A disc having WC-Co & PVA solution in with an approximate diameter of 20mm (left), a magnified image at 200x of the disc (right)

7. The stacked discs were subjected to thermal debinding in an argon gas atmosphere using a tube furnace. The tube furnace used is a MTI GSL 1600X and is shown in Figure 32. The debinding procedure for the PVA paste had been developed using thermogravimetric analysis (TGA) data given by Youseffi et al. [41] and is given below:

    i) Heating from room temperature to 200°C at 10°C/minute

    ii) Heating from 200°C to 270°C at 5°C/minute

    iii) Holding at 270°C for 15 minutes

    iv) Heating from 270°C to 350°C at 2°C/minute

    v) Holding at 350°C for 15 minutes

    vi) Heating from 350°C to 650°C at 5°C/minute

    vii) Holding at 650°C for 30 minutes

Figure 32. The equipment (tube furnace) used for debinding of the WC-Co and binder discs

8. The debonded discs were then transferred to a 20mm sintering die & punch (shown in Figure 33) in the following order: one column of WC-Co discs at the bottom of the die, WC-Co powder mixture in the center of the die for a height of about 10mm, and the second column of WC-Co discs at the top of the die.

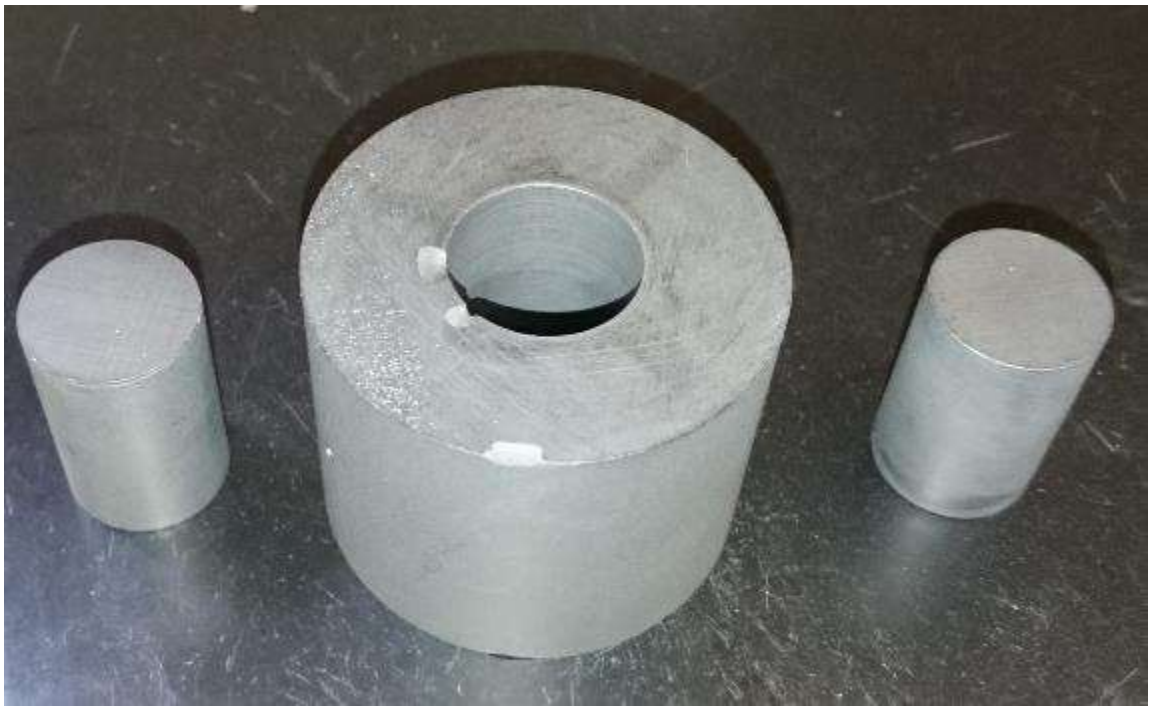

Figure 33. Die & punches used for sintering. The cylindrical rods in the left and the right are the two punches and the hollow cylindrical piece in the center is the die.

9. The material was finally subjected to field assisted sintering technology (FAST) which is also known as spark plasma sintering (SPS). The sintering die and punch setup inside the SPS machine and the heating area of the SPS machine is shown in Figure 34. The sintering procedure used is an optimized process proven to help achieve minimum growth and fully dense WC-Co samples [35]. The temperature and pressure curves for the sintering procedure are shown as the two solid paths represented by the number 15 in Figure 35. High starting vacuum of about 1e-6 Torr was used during the sintering process. The final sintered sample is shown in Figure 36.

The final procedure was used to make this sample is summarized in the flow chart given in Figure 37.

Figure 34. Sintering die and punch setup inside the SPS machine (left); SPS machine's heating setup (right)

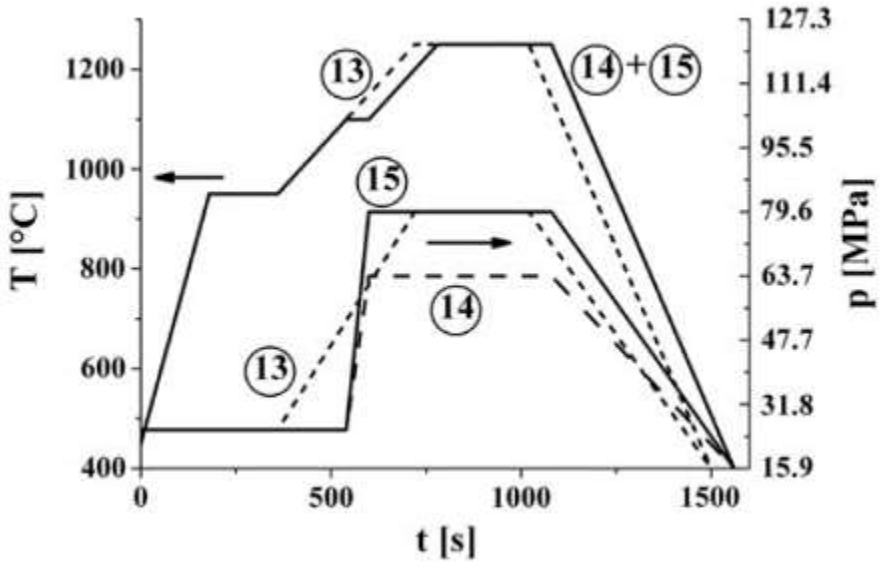

Figure 35. Temperature and pressure histories of the sintering processed used to optimize the sintering of WC-Co samples. The solid set of temperature and pressure lines shown by number 15 are used in this work [35].

Figure 36. WC-10%Co compact sintered using the spark plasma sintering machine. The compact had a diameter of 20mm and a thickness of about 7mm.

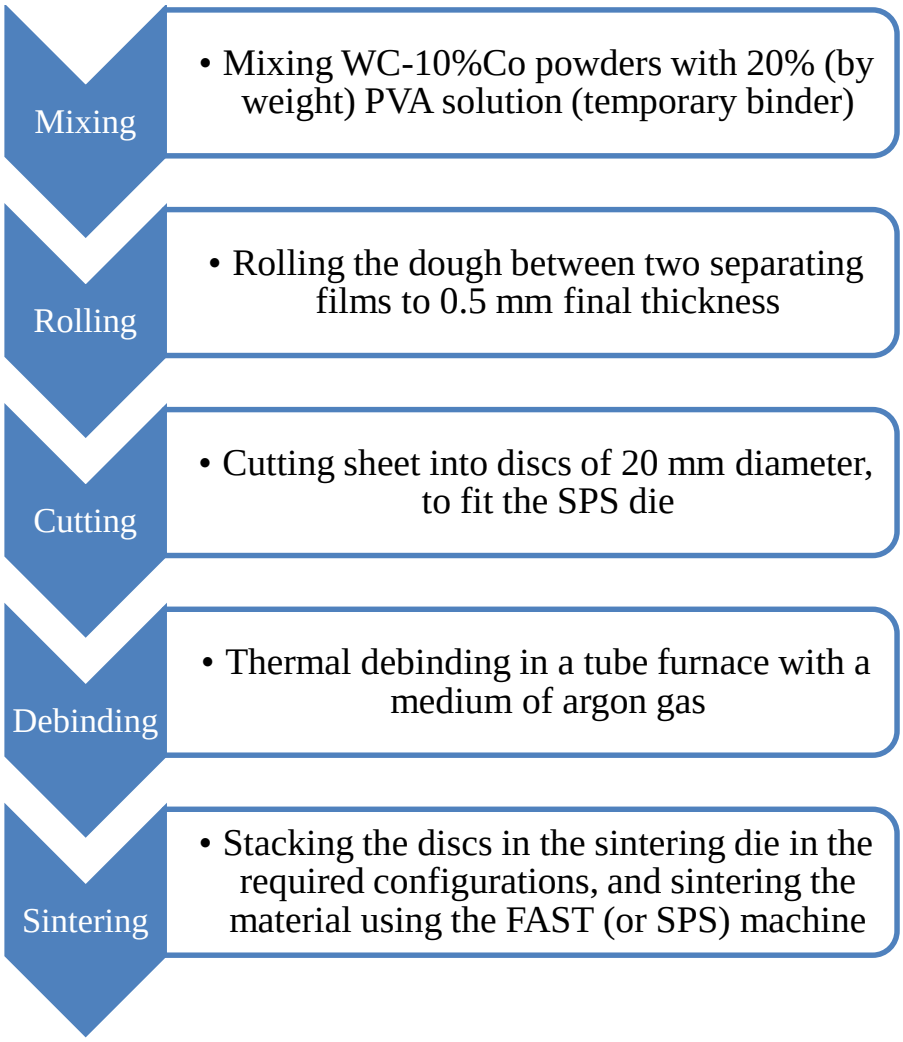

Figure 37. Flow chart of fabrication steps for the final WC-Co sample

4.3 Characterization of Morphology of the Sintered WC-Co Bulk Composites

The sintered sample was sectioned using a precision sectioning saw that has a diamond wafering blade. The sectioning is done so to cut a piece that would reveal an area with the rolled WC-Co discs and an area with the WC-Co powder (as shown in the top-left region of Figure 38). The sectioned piece is shown in the top-right region of Figure 38. A schematic of the front view of the sectioned piece in shown in the bottom of Figure 38. According to this front view, the sectioned piece is further sliced at the dotted line given by (1) in Figure 38 to obtain a surface having the rolled WC-Co discs. The sample is further sliced at the dotted line (2) to expose a surface having the WC-Co powder.

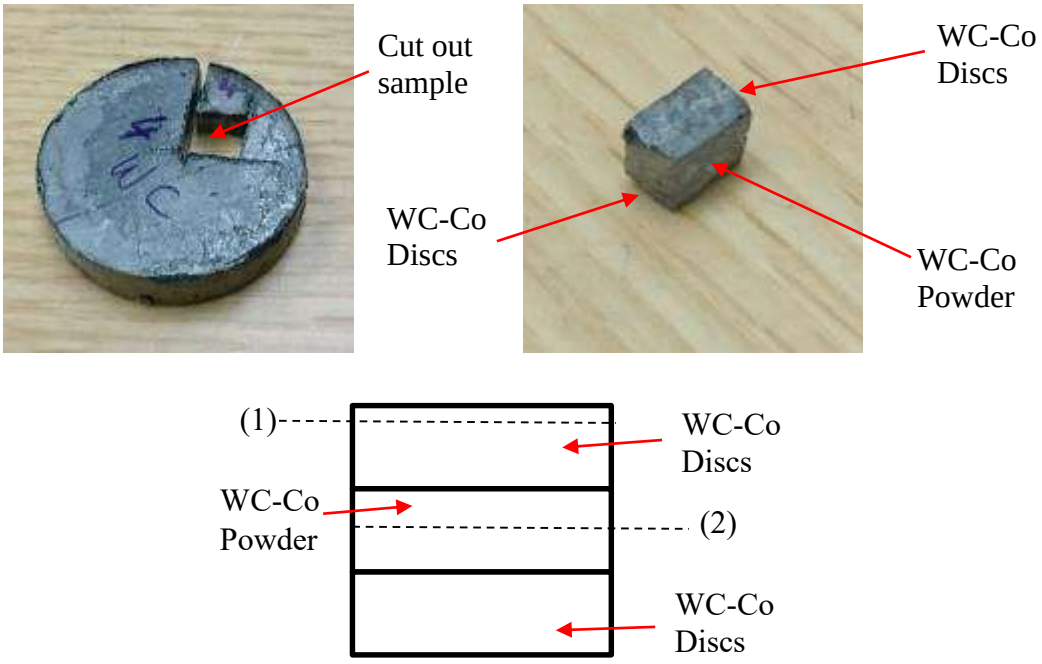

Figure 38. A representative sample showing region where a cut out was made (top-left), the cut out section revealing the rolled WC-Co disc areas and the WC-Co powder areas (top-right), and, a schematic of the front view of the cut out section showing the different areas of the sintered sample (bottom)

The sectioned WC-Co samples were mounted in a cold-curing thermosetting material for polishing purposes. The two mounted specimens were then prepared on the Struers LabPol-5 semi-automatic polishing machine which is shown in Figure 39. The sample preparation steps are as follows:

1. Grinding using 1200 grit silica carbide (SiC) paper until the WC-Co surface is exposed from the epoxy.
2. Polishing using 9 μm diamond suspension on a flat woven cloth which has no nap for 5 minutes. The speed of rotation of the platen is set to 180 rpm and the speed of the polishing arm is set to 30rpm.

3. Polishing using 6 μm diamond suspension on a flat woven cloth which has no nap for 4 minutes. The speed of rotation of the platen is set to 180 rpm and the speed of the polishing arm is set to 30rpm.
4. Polishing using 1 μm diamond suspension on a flat woven cloth which has no nap for 3 minutes. The speed of rotation of the platen is set to 180 rpm and the speed of the polishing arm is set to 30rpm.
5. Polishing using 0.06 μm colloidal silica suspension on a low nap cloth which for 5 minutes. The speed of rotation of the platen is set to 180 rpm and the speed of the polishing arm is set to 30rpm.
6. Polishing using 0.06 μm colloidal silica suspension on a low nap cloth on a vibratory polisher for 40 minutes.

Figure 39. The equipment used for the polishing of the WC-Co samples for studies in the SEM and EBSD

The SEM images of the sample having the rolled WC-Co discs are shown in Figure 40. Similarly, the SEM images of the sample having WC-Co powder are shown in Figure 41. On comparison of Figure 40 and Figure 41, it can be observed there is a higher number of large grains in the area with the rolled WC-Co discs when compared to the area with the WC-Co powder. This could be due to higher rates of grain growth in certain orientations. The EDX of a representative area of the sample containing rolled WC-Co discs is shown in Figure 42. From Figure 42, we can observe that the Co is more or less evenly distributed between and around the WC grains.

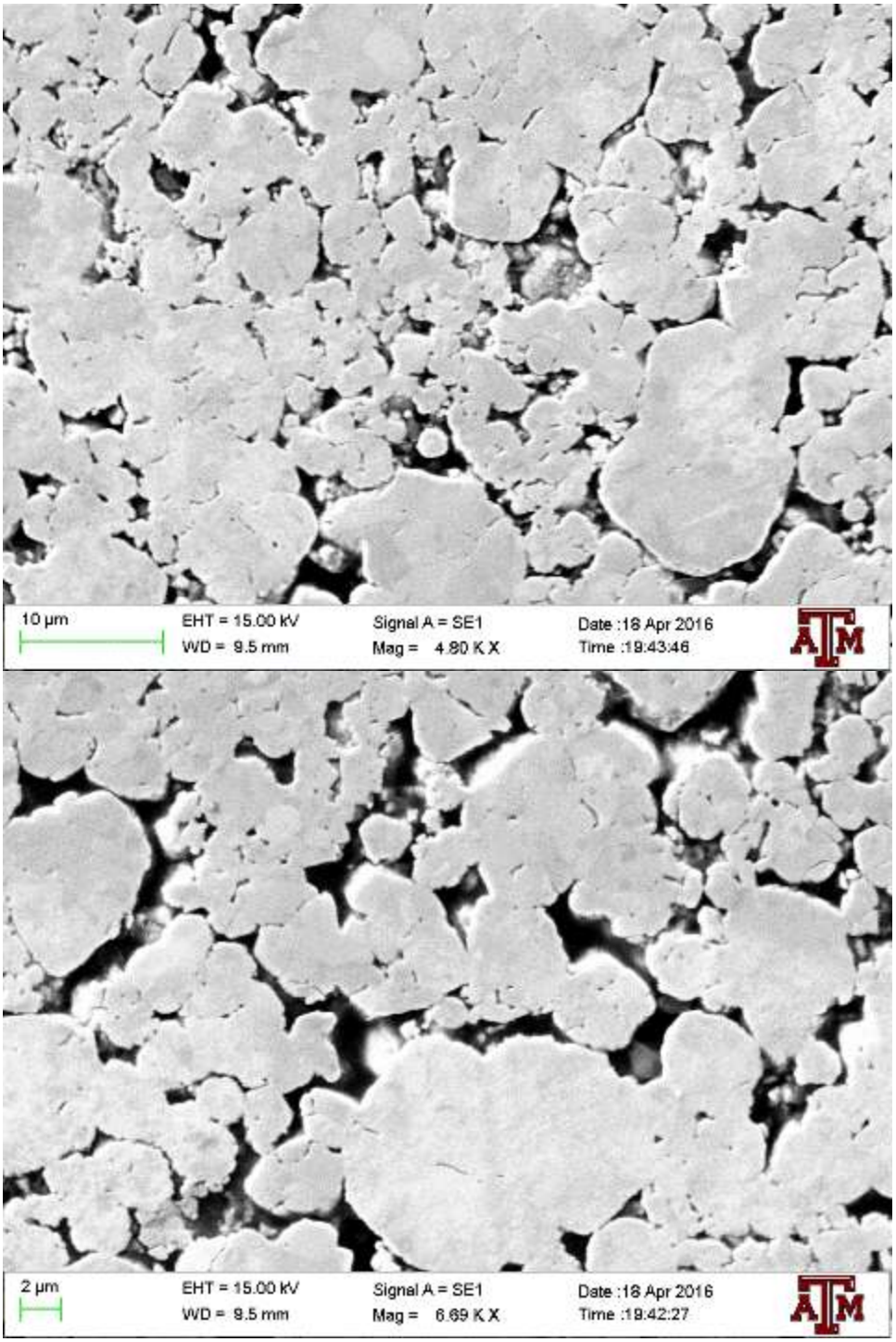

Figure 40. SEM images of the sample having the <u>rolled WC-Co discs</u> (top picture is at a low magnification, and bottom picture is at a high magnification). The particle size of the WC powder used is 4 µm and the particle size of the Co powder used is 0.5 µm

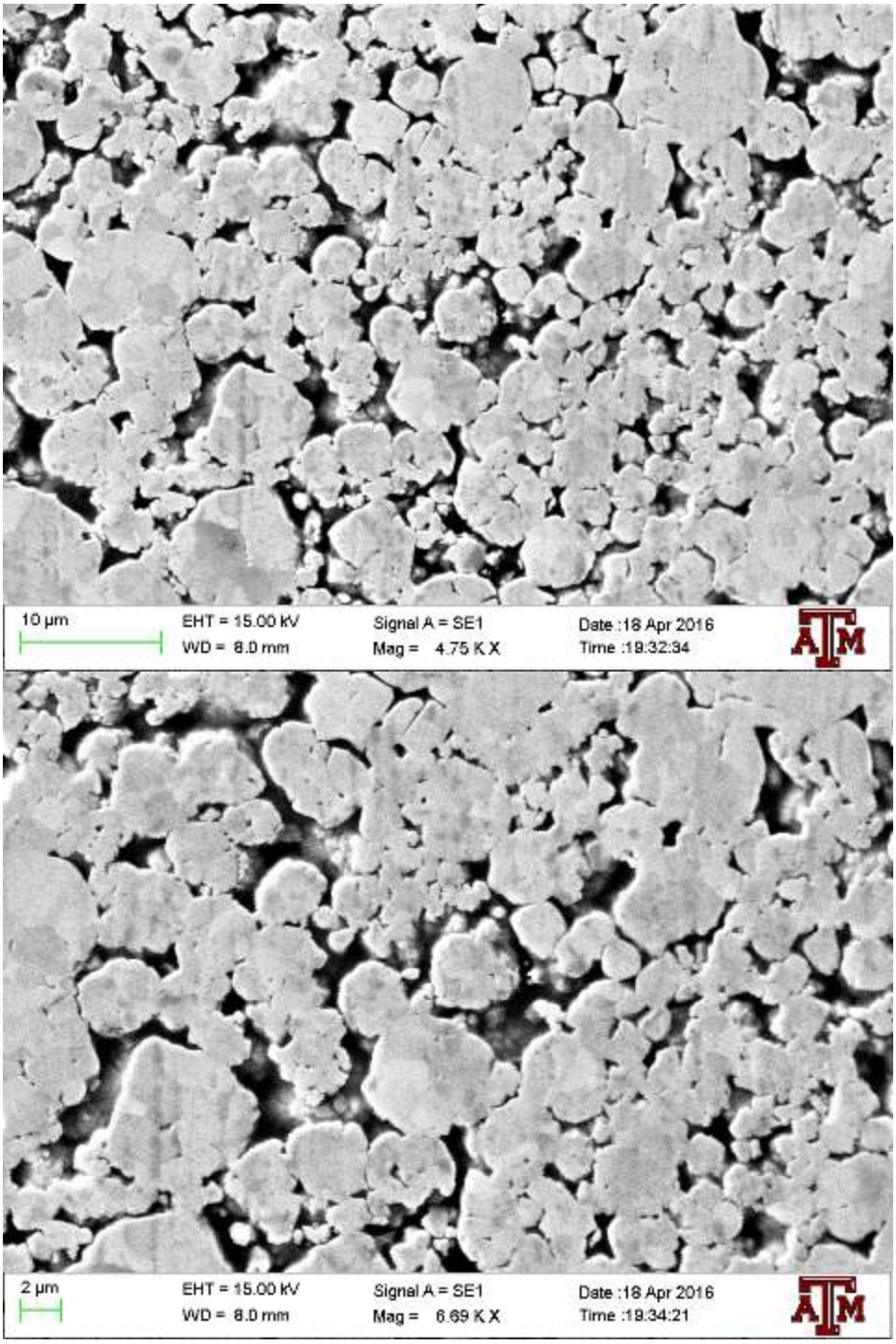

Figure 41. SEM images of the sample having <u>WC-Co powder</u> (top picture is at a low magnification, and bottom picture is at a high magnification). The particle size of the WC powder used is 4 µm and the particle size of the Co powder used is 0.5 µm

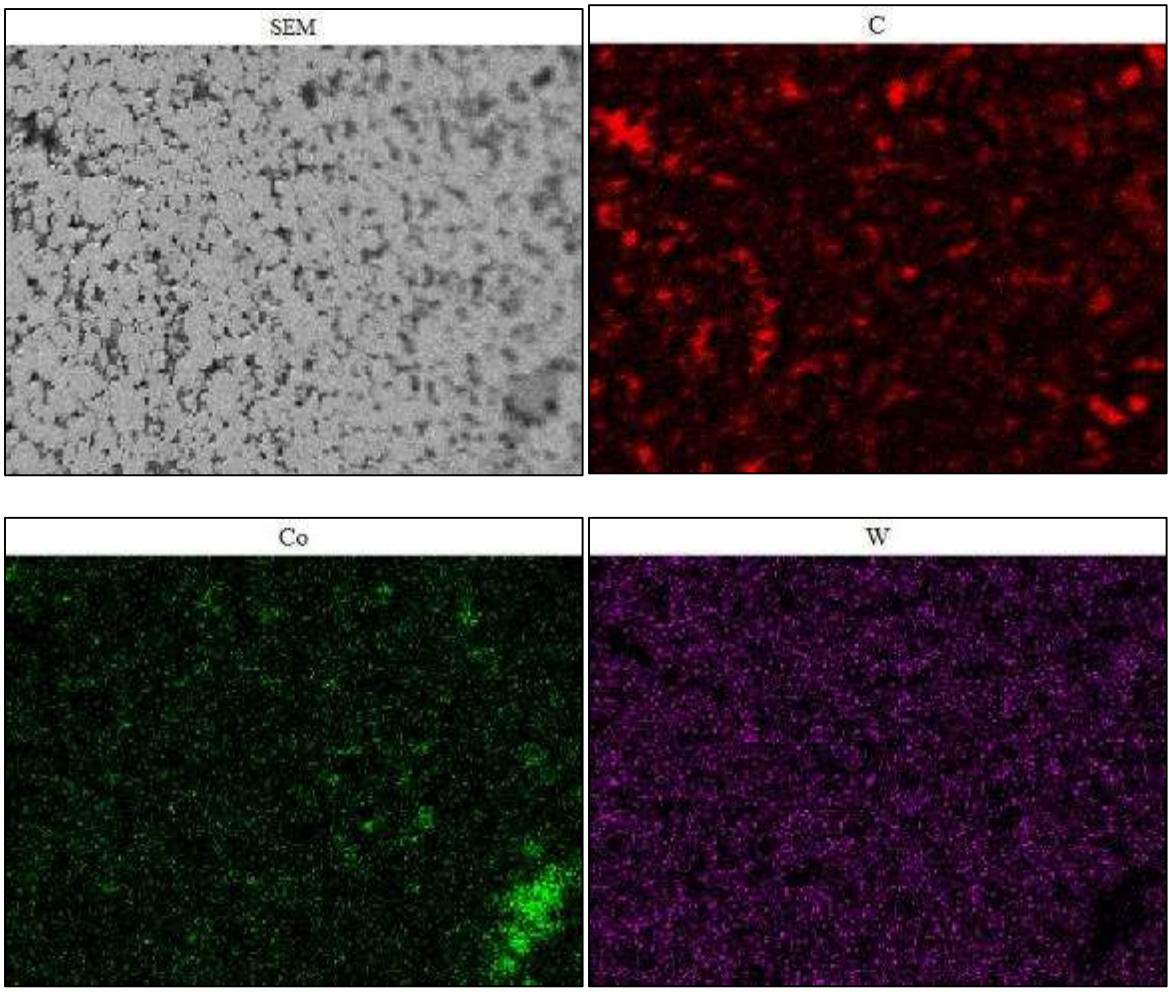

Figure 42. EDX area scans of a representative part of the sample having the rolled WC-Co discs (The top-left image is the SEM image, the red dots in the top-right image show carbon, the green dots in the bottom-left image show cobalt)

Bulk texture analysis of the areas with the rolled WC-Co discs and WC-Co powder was performed using an X-ray diffractometer. A Bruker D8 X-ray Diffractometer was used which is shown in Figure 43. Cu K_α radiation (which has a wavelength of 1.5418 Å) was using for obtaining the X-ray diffraction (XRD) results. The XRD patterns of the two samples are shown in Figure 44. The diffraction peaks primarily belonged to the WC phase

in both the samples. The basal (0001) planes and two of the prismatic planes: $(1\bar{1}00)$ & $(10\bar{1}1)$ are the generally the most dominantly observed planes in bulk WC-Co composites as was observed in Figure 44.

Defining the relative intensity of the strongest peak in one XRD pattern as 100%, the relative intensity of WC (0001) plane in the area with WC-Co powder shown in Figure 44 (a) is 46%. Similarly, the relative intensity of WC (0001) plane in the area with the rolled WC-Co discs shown in Figure 44 (b) is 67%. Figure 44 implies that the area ratio of basal (0001) planes is higher in Figure 44 (b) when compared to Figure 44 (a). Hence, a more dominant basal (0001) plane texture has been observed in the sample that had the rolled WC-Co discs. An XRD pattern of a vertical section of the region having the rolled WC-Co discs is shown in Figure 45. The relative intensity of WC (0001) plane in Figure 45 is about 43%. The relative intensity of basal planes in the vertical section should be lesser than that of the sections shown in Figure 44 because it is parallel to the rolling and sintering direction. Hence, the patterns obtained in Figure 45 do not contradict the expected results.

Figure 43. The equipment (X-Ray Diffractometer) used for obtaining details about bulk texture of the WC-Co composite

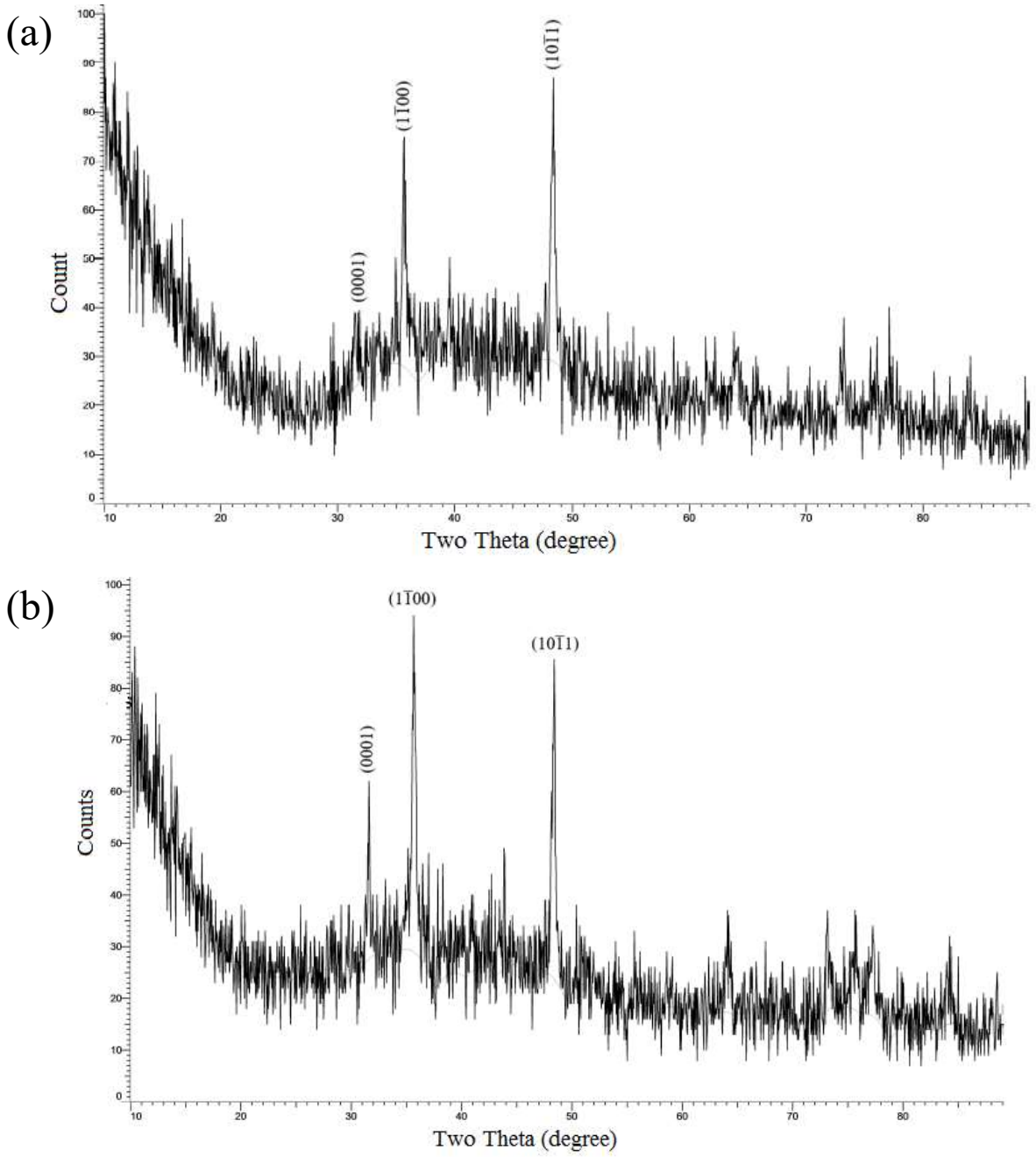

Figure 44. XRD patterns of (a) the sectioned sample with the randomly oriented WC-Co powders and (b) the sectioned sample with rolled WC-Co discs showing a more dominant grain texture of the basal plane (0001)

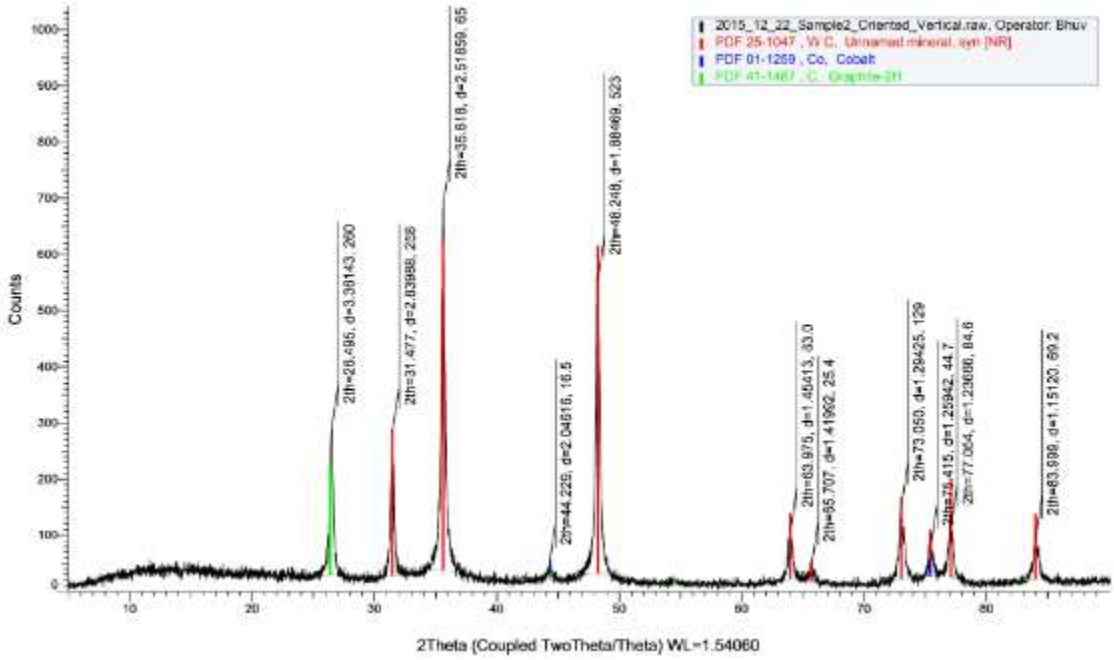

Figure 45. XRD pattern of a vertical section of the region having the rolled WC-Co discs. The peak at about 32° is for the basal plane (0001)

Additionally, the samples was subjected electron back scattering diffraction (EBSD) to obtain area maps of about 50µm side as shown in Figure 46. From these area maps, Kikuchi bands (shown in the left of Figure 47) were obtained. The Kikuchi bands seen in Figure 47 correspond to different diffracting crystal planes. Each of these bands were then indexed individually by the Miller indices of the diffracting plane that formed it as shown in the bottom right of Figure 47. However, due to inconsistencies in the very stringent polishing requirements for EBSD, only a ~75% hit rate was achieved. These specimens will be polished to specification in the future to deduce results from EBSD maps, which further confirm the macro/global orientation results obtained through XRD.

A focused ion beam SEM could also be used for better polishing and EBSD results compared to mechanically polished samples.

It is further possible to obtain the Euler angles and related data need to characterize the orientation of each grain using a post-processing software. This data can then be converted in form of inverse pole figures (IPF) or orientation distribution functions (ODF) to identify the crystallographic orientation of each of the grains. This helps in obtaining further and highly accurate evidence regarding the presence/absence of dominant grain orientation texture.

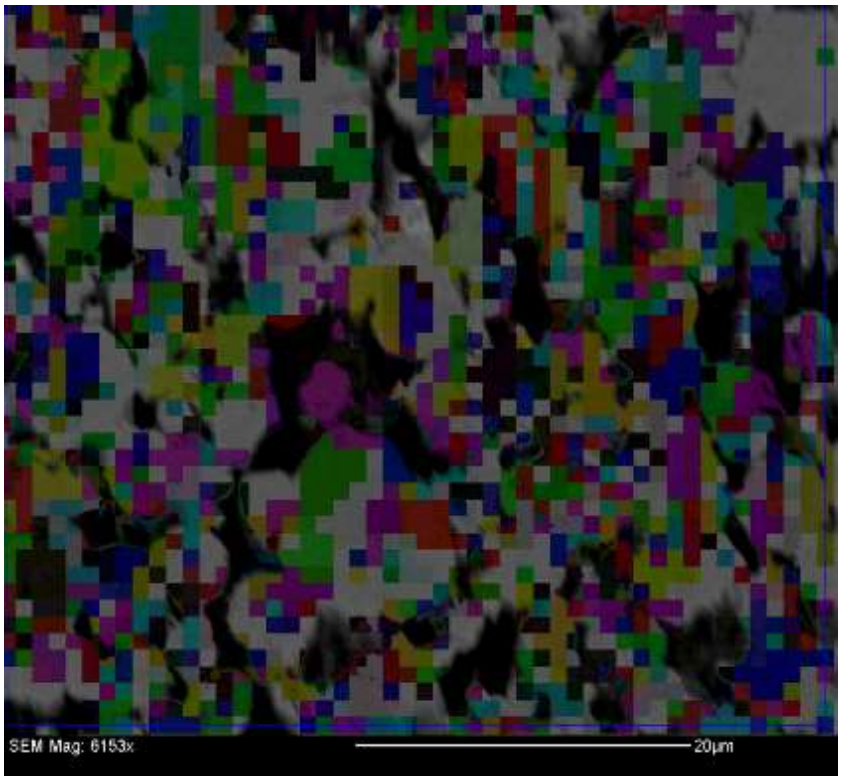

Figure 46. Area scan to identify orientation of the grains in WC-Co composite using EBSD on the SEM. Due to inconsistencies in the very stringent polishing requirements for EBSD, only a ~75% hit rate was achieved which needs further rectification.

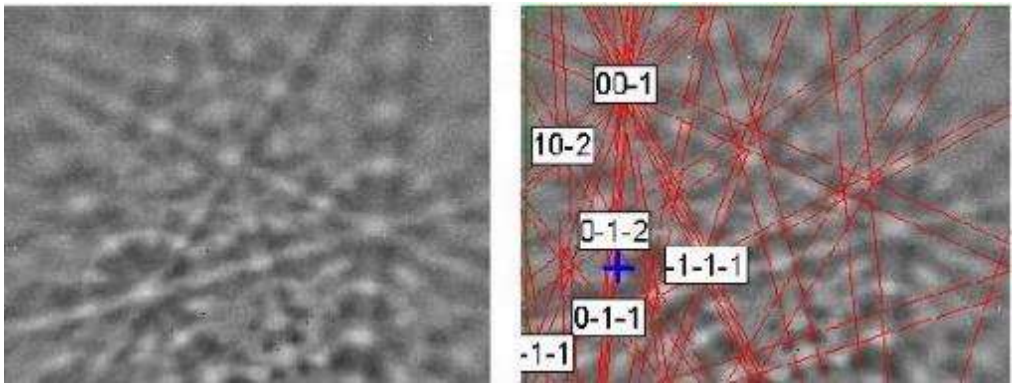

Figure 47. Kikuchi bands of a particular spot in the sample (left), and identification of miller indices that the bands correspond to (right)

4.4 Discussion of Results

This chapter served to answer RQ1. A procedure for obtaining bulk orientation texture in WC-Co composites was developed and refined. This procedure involved the preparation of a malleable dough using WC-Co powders, and a temporary binder by subjecting the dough to multiple pressurized rolling operations. The thin sheets obtained were cutout into discs to match the sintering die dimensions, debound in an inert atmosphere to remove the majority of the temporary binder and finally sintered in a SPS machine. The comparative dominance of a basal-plane texture of the samples subjected to rolling (vs. powder) was confirmed through XRD results.

5. EFFECT OF GRAIN ORIENTATION TEXTURE ON THE HARDNESS AND ABRASION RESISTANCE (RQ2)

This chapter serves to answer research question 2 (RQ2), i.e., "What is the effect of grain orientation texture on the hardness and abrasion resistance of sintered WC-Co composites?" It elaborates on the procedures used to study the hardness and abrasion resistance of the material including nano-indentation, microhardness testing and scratch testing. Additionally, the scribed surfaces are analyzed using high-resolution microscopy and interferometry to identify any differences in the wear mechanisms involved as well as to obtain a quantification of the relative wear volumes.

5.1 EFFECT OF HARDNESS ON ABRASIVE WEAR (KRAMER'S MODEL [42])

The abrasive wear of a tool dramatically decreases when the hardness of the tool material approaches that of the abrasive. Larsen–Basse [43] has shown that there is a transition in the wear mechanism when the hardness of the abrasive decreases below 1.2 times the hardness of the surface being abraded.

To predict abrasive wear rate, Rabinowicz's quantitative results [44] are the starting point. The abrasive wear behavior may be separated into three regions, depending on the ratio of the hardness of the abrasive to that of the abraded surface. In each hardness regime, the wear volume (V_m) that is removed from the surface in sliding a distance x is:

$$V_m = \frac{xLTan\theta}{3P_t}, \text{for } P_t / P_a < 0.8 \quad (1)$$

$$V_m = \frac{xLTan\theta}{5.3P_t}\left(\frac{P_t}{P_a}\right)^{-2.5}, \text{for } 1.25 > P_t / P_a > 0.8 \quad (2)$$

$$V_m = \frac{xLTan\theta}{2.43P_t}\left(\frac{P_t}{P_a}\right)^{-6.0}, \text{for } P_t / P_a > 1.25 \quad (3)$$

where L is the applied normal force between the surfaces, $Tan\theta$ is the average tangent of the roughness angle of the abrasive grains (a measure of the particle shape or sharpness), P_t is the hardness of the material, and P_a is the hardness of the inclusions. A database containing the hardness as a function of temperature for different materials and abrasive particles is needed.

From the above formulation, the absolute abrasive wear rate can be calculated. The abrasive wear volume is dependent on the distance slid. It is reasonable to assume that the abrasive wear rate will be proportional to V (cutting speed in feet/min). The abrasive wear rate is also proportional to $K\frac{P_a^{n-1}}{P_t^n}$, where P_a and P_t are at the cutting temperature of interest. The constant, n, depends on the relative tool to abrasive hardness.

- For $P_t/P_a < 0.8$, n = 1.0 and K = 0.333
- For $1.25 > P_t/P_a > 0.8$, n = 3.5 and K = 0.189
- For $P_t/P_a > 1.25$, n = 7.0 and K = 0.416

The absolute abrasive wear rate has been calculated as: $AVK\frac{P_a^{n-1}}{P_t^n}$, where, A is a calibration constant to be determined by best fit, and V is the cutting speed in feet/min. In all, it can be said that abrasive wear is inversely proportional to hardness, and hence

quantifying the hardness of a material offers a good estimation of its resistance to abrasive wear.

5.2 Mechanical Property Characterization of WC-Co Composites

5.2.1 Hardness Testing of Bulk WC-Co Composites (Nano-indentation and Micro-indentation)

5.2.1.1 Nano-indentation Testing

Two samples of the sintered WC-Co bulk samples were cut out using a precision sectioning saw that has a diamond wafering blade. One of the samples was an area having the rolled WC-Co discs and the other sample was an area having the randomly oriented WC-Co powder.

The two samples were mounted in a cold-curing thermosetting material. Both the mounted samples were then polished using the procedure listed in section 4.3. The two samples were then subjected to nano-indentation testing at room temperature on a Fisherscope HM2000 Nano-indentation Tester to obtain hardness values across various tungsten carbide (WC) grains (Figure 48). A diamond Berkovich tip having a nominal radius of curvature of about 1 μm was used for the hardness measurements.

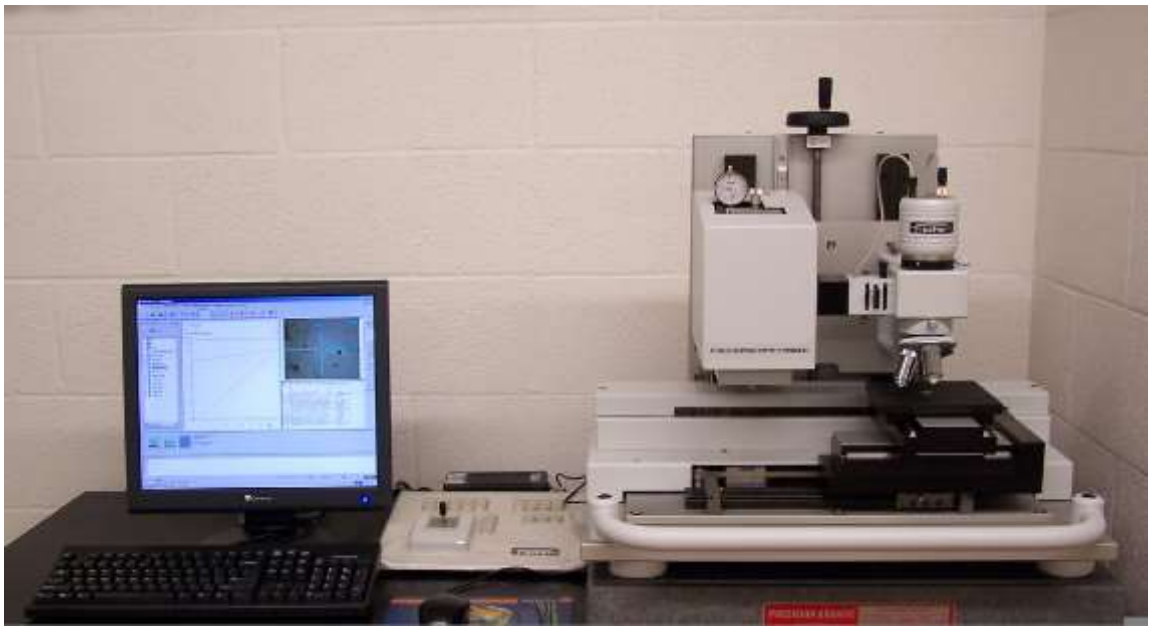

Figure 48. The equipment used for nano-indentation testing of the WC-Co composite

The nano-indentation tester has an optical microscope that is used to select the approximate points where the hardness testing has to be performed. Before using the WC-Co samples, the machine was calibrated carefully on a known sample, which assured reliability of measuring data. The indentation depth was set to 200 nm [2].

The WC-Co samples were then placed on the stage beneath optical microscope and focused to an area where hardness readings would be taken. An example of one of the focused areas is shown in Figure 49.

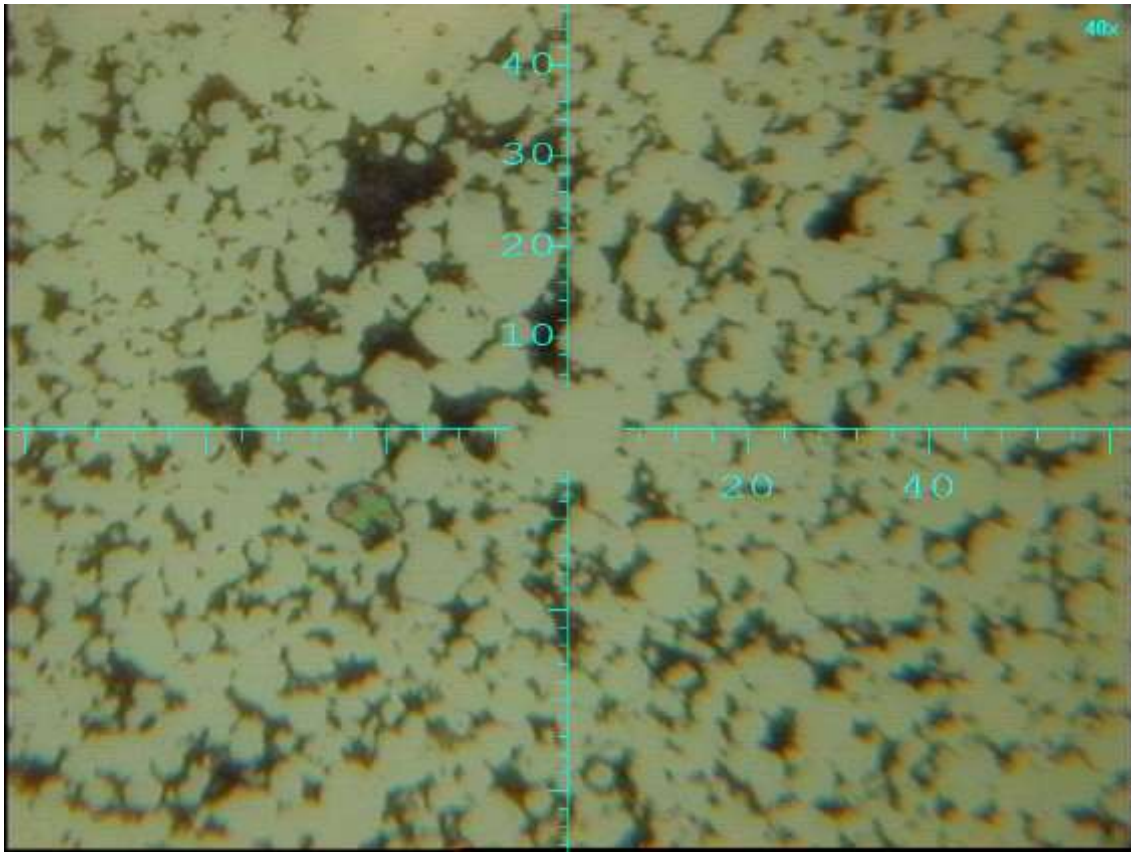

Figure 49. Focused area in the piece having the rolled WC-Co discs

After selecting a required number of points (40 points in this case), indents were performed on those 40 spots across both the samples. The indents had enough distance between them to avoid interaction of the generated stress fields. SEM images of the indentation marks on the samples with the rolled WC-Co discs and the randomly oriented WC-Co powders are shown in Figure 50 and Figure 51 respectively. Due to the large size of the indentations, most the hardness values were measured across multiple WC grains that would include the area between grains having a weaker cobalt as well. Some of the

indentations were completely on the epoxy, and some indentations were on a localized cobalt region as shown in Figure 52.

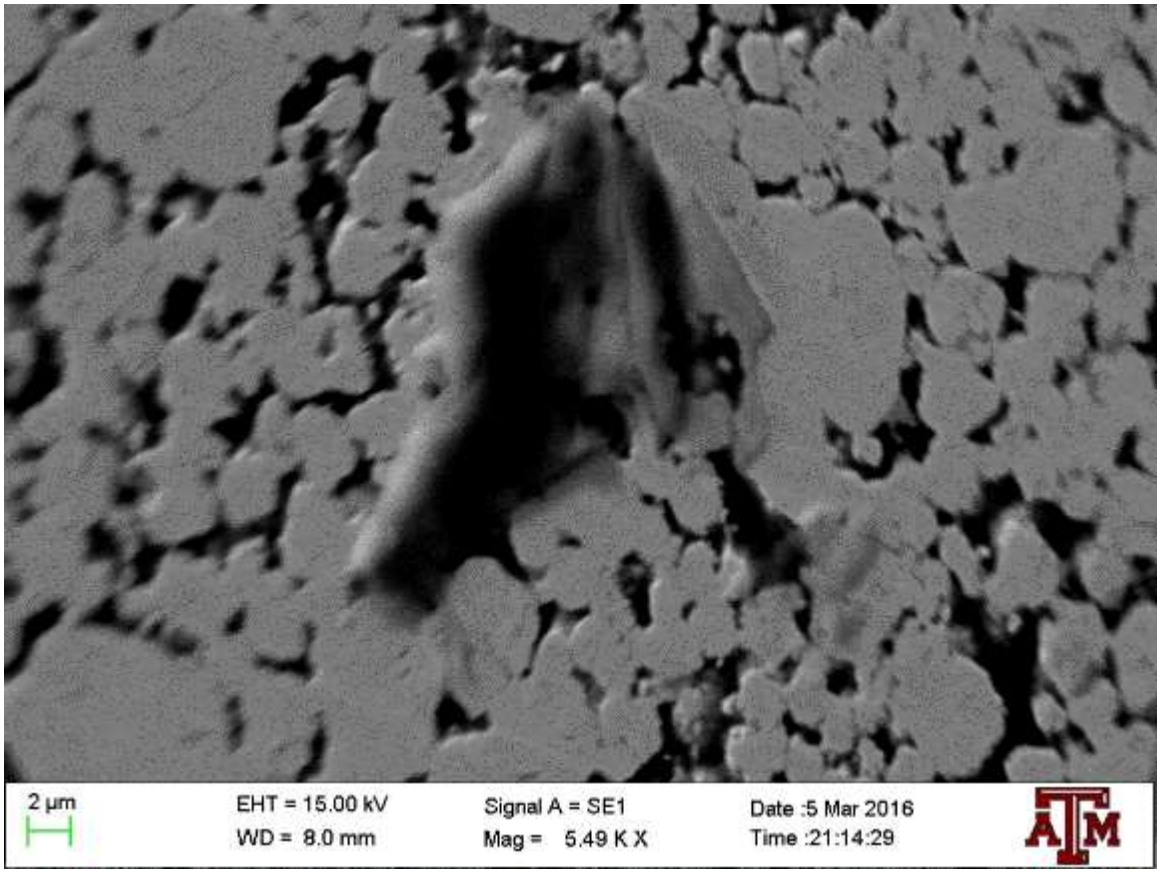

Figure 50. SEM image of an indentation mark in the sample having the rolled WC-Co discs

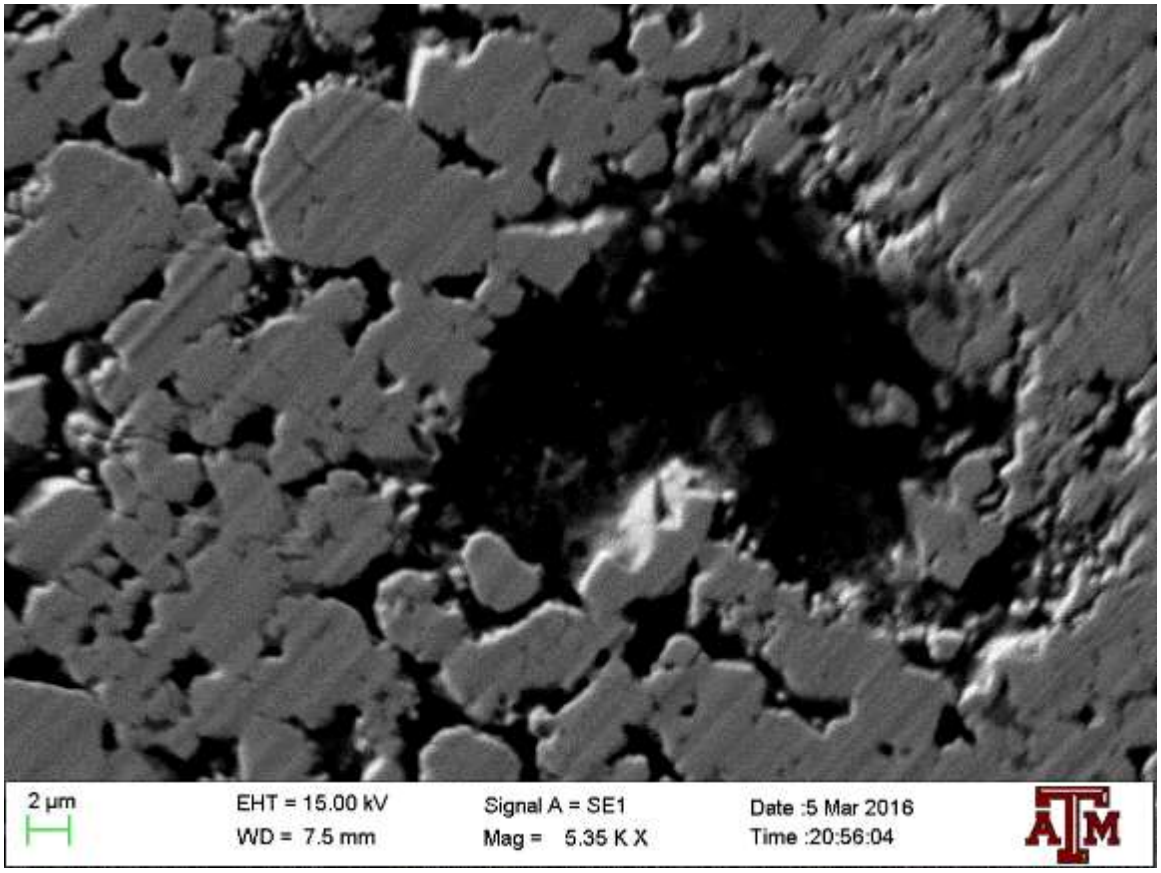

Figure 51. SEM image of an indentation mark in the sample having the randomly oriented WC-Co powder

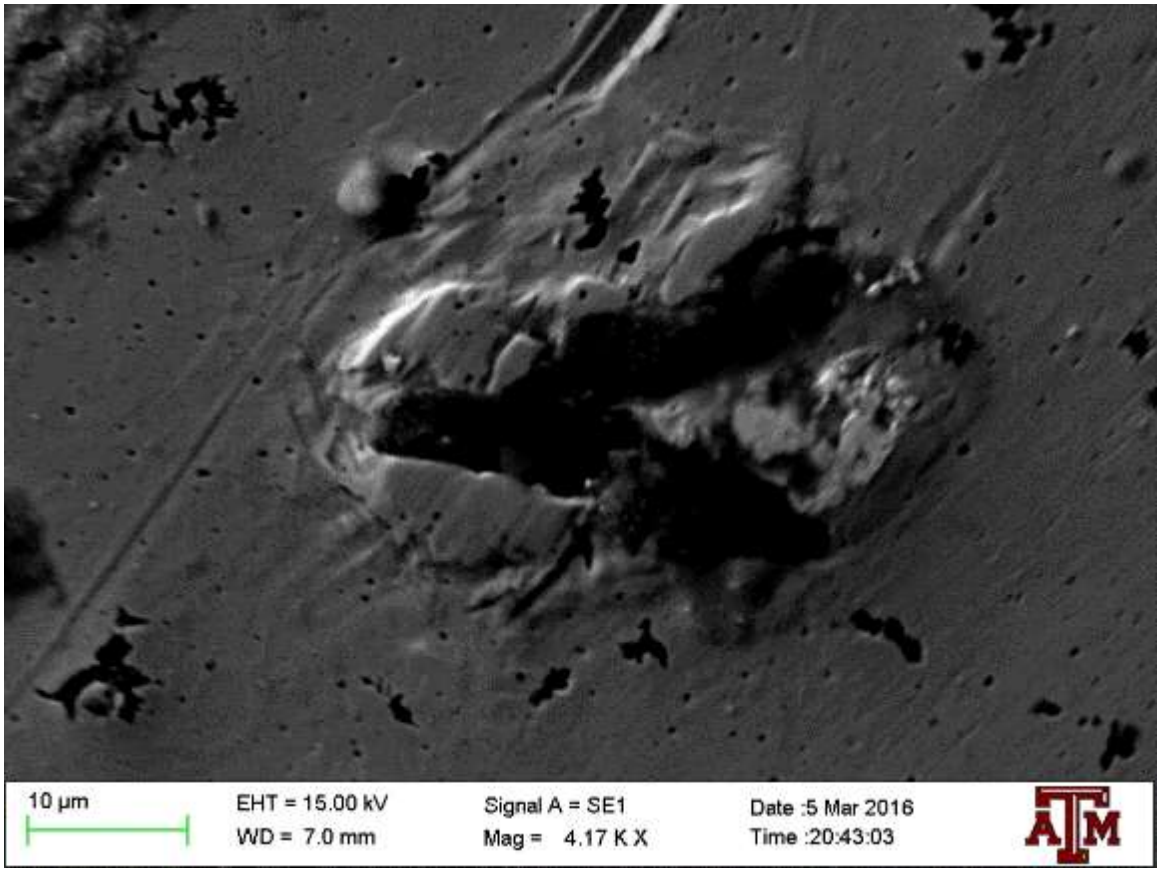

Figure 52. SEM image of an indentation mark in a localized cobalt region in the sample with the randomly oriented WC-Co powder

Some of the hardness values were very close to zero. This was because some indentation marks were on the mounting material that was quite soft and had many porosities in it. Some other hardness values were lower than 5.5 GPa. Since the hardness of cobalt measured with the same indenter under similar loading conditions is known to be around 5.5 GPa, no values below that were considered. Some of the typical load displacement curves obtained for the area having WC grains is shown in Figure 53.

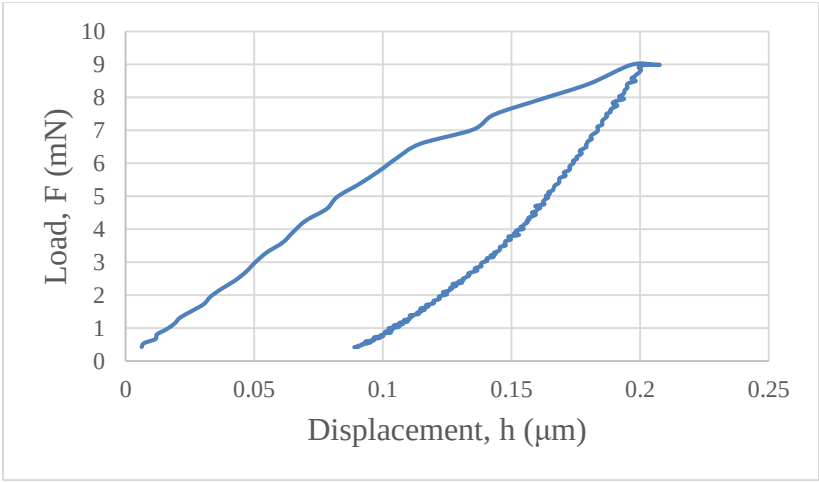

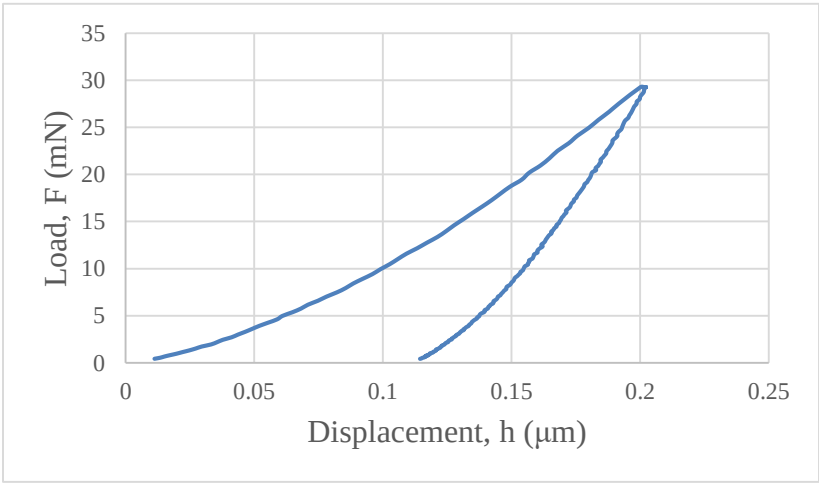

Figure 53. Two of the various load-displacement curves obtained for the indentations on the WC-Co samples

16 hardness and indentation modulus readings were obtained for the sample having the rolled WC-Co discs and they are shown in Table 1. The mean hardness obtained for the sample with the rolled WC-Co discs is 18.739 GPa with a standard deviation of 13.163 GPa.

Table 1. Hardness and indentation modulus values of the sample having the rolled WC-Co discs

Reading Number	Hardness, H (GPa)
1	6.30592
2	8.73213
3	47.7181
4	7.72476
5	18.1399
6	39.3566
7	13.5843
8	19.5256
9	35.1839
10	77.9185
11	34.5543
12	11.9845
13	13.2366
14	19.0566
15	9.70626
16	7.22002

Similarly, 23 hardness and indentation modulus readings were obtained for the sample having the randomly oriented WC-Co powders and they are shown in Table 2. The mean hardness obtained for the sample with the rolled WC-Co discs is 13.779 GPa with a standard deviation of 5.460 GPa.

Table 2. Hardness values of the sample having the randomly oriented WC-Co powders

Reading Number	Hardness, H (GPa)
1	11023.4
2	10419.8
3	9594
4	14568.6
5	16518.6
6	8143.6
7	9213.78
8	7211.11
9	20390.6
10	23572.8
11	8458.19
12	25247.7
13	14591.7
14	14857.1
15	7804.13
16	13600.3
17	9831.98
18	18942
19	17394.6
20	8502.39
21	21303.3
22	8558.67
23	17185

The average composite hardness of the sample having the rolled WC-Co discs is hence about 36% higher than the average composite hardness of the sample having the randomly oriented WC-Co powder. This increase in hardness can be attributed to the higher area ratio of basal planes in the sample having the rolled WC-Co discs.

The high standard deviations observed could be due to various reasons. Since indented area had a maximum dimension in the range of 15 μm and the average grain size was about 5 μm, the indentations were across multiple grains with some softer area of cobalt as well. Different indentations could cover varying amounts of cobalt thus affecting the hardness readings. Additionally during polishing of the samples, cobalt is more easily removed as it has a comparatively lower hardness and this develops recessed areas of cobalt.

Further, five individual tungsten carbide (WC) grains were also analyzed using another Berkovich tip having a tip radius of about 150 nm. The low tip radius helps in indenting single grains of WC, as the average grain size of WC in the samples is about 5 μm. An atomic force microscope (AFM) image of one of the indents is shown in Figure 54. The hardness reading obtained for the 5 grains are shown in

Table 3. The average of these readings is about 20.71 GPa with a standard deviation of 2.88 GPa.

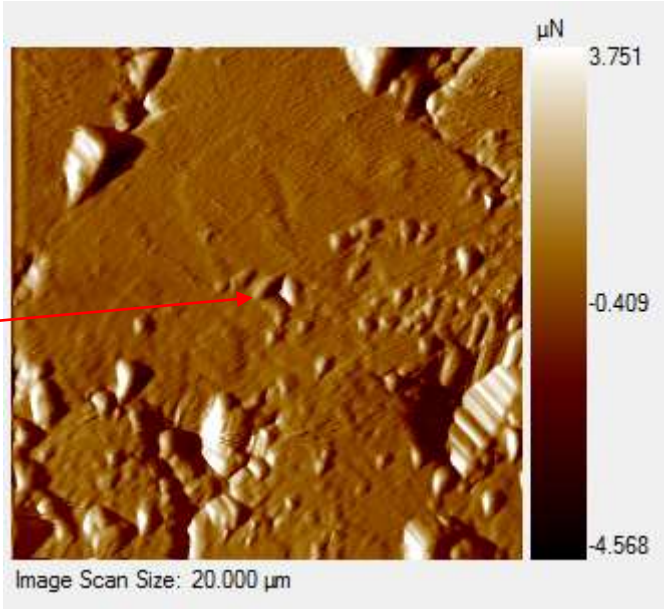

Figure 54. AFM image of the one of the indents located in the center of the image

Table 3. Nano-hardness values on 5 individual grains of tungsten carbide

Indentation Number	Hardness (GPa)
1	24.54228
2	17.06274
3	18.80845
4	21.38502
5	21.76528

5.2.1.2 Micro-hardness Testing

The two samples are subjected to micro-hardness testing using a Vickers diamond indenter as shown in Figure 55. The machine used for the micro-hardness testing is shown in Figure 56.

Figure 55. Vickers indenter used for micro-hardness testing of the WC-Co samples

Figure 56. Micro-hardness testing machine used for indenting and measuring the microhardness of the WC-Co samples

The Vickers hardness indenter has the form of a right pyramid with a square base and an angle of 136° between opposite faces as shown in the top region of Figure 57. The indentations formed have a rhombic shape as shown in the bottom region of Figure 57. For this rhombic region, the diagonal lengths (given by d1, d2 in Table 4 and Table 5) are then measured using a microscope and their average is calculated. The Vickers hardness value is then obtained by dividing the load applied by the indenter (in kgf) by the area of

the indentation (in mm^2). The formula used for calculation of the Vickers hardness (HV) is given by:

$$HV = \frac{2F\sin(\theta/2)}{d^2} \tag{4}$$

where θ is the angle between the opposite faces of the indenter (136°), F is the load applied in kgf, and d is the arithmetic mean of the two diagonals, d1 & d2 in mm. A microscope image of on the indents is shown in Figure 58.

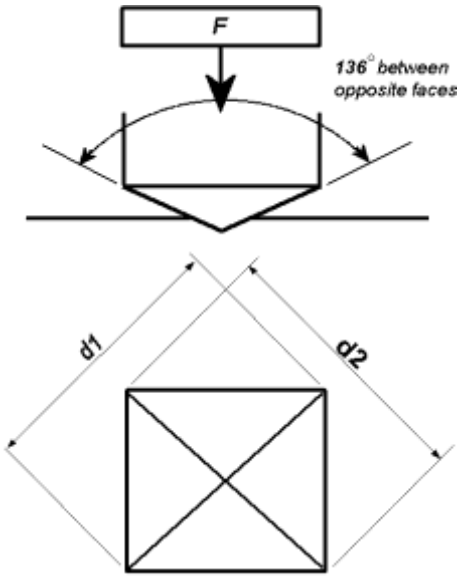

Figure 57. Representative image showing the Vickers indenter loading the sample (top); the shape of the indentation created on the sample (bottom) [45]

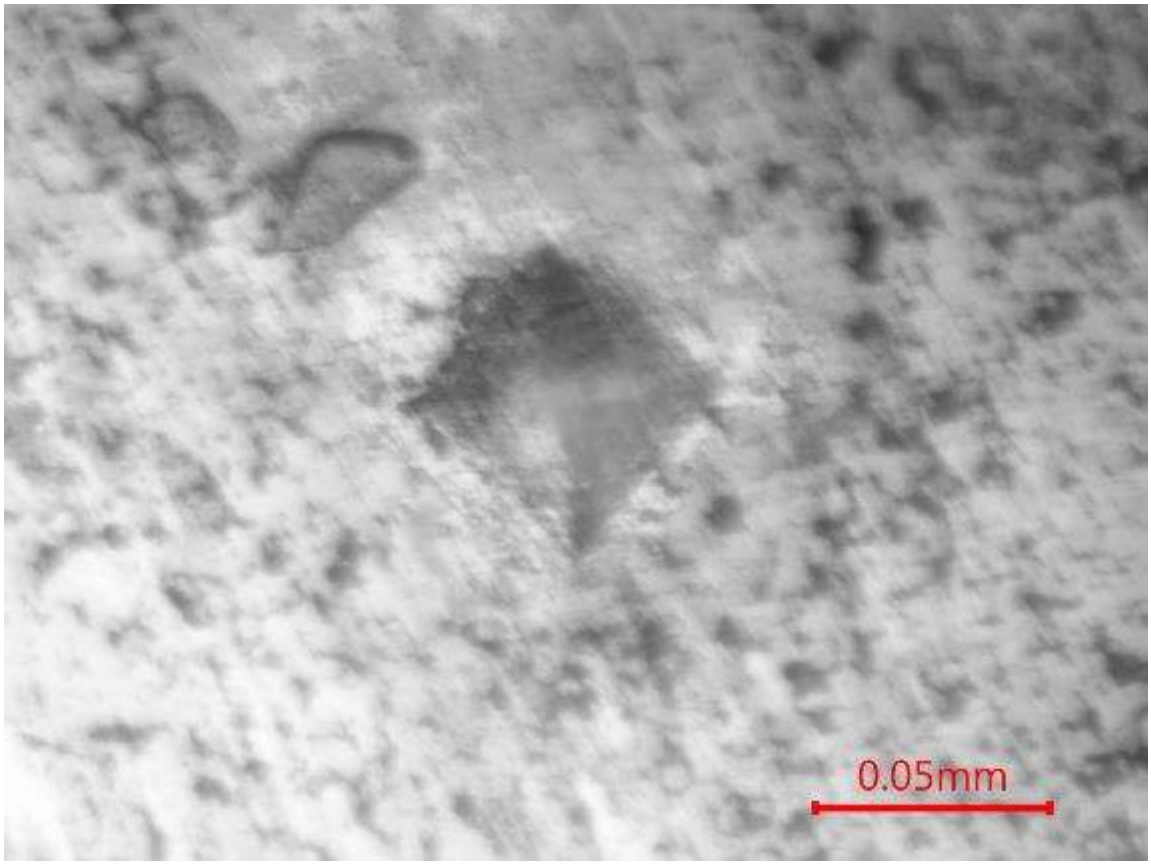

Figure 58. An image of one of the actual Vickers indentations that was obtained using an optical microscope

Ten indentations were performed on the sample having the rolled WC-Co discs as well as the sample having the randomly oriented WC-Co powder using a Vickers indenter. The load used for the indentation was 1 kgf for a duration of 15 seconds. The values of d1, d2 and HV obtained for the sample with the rolled WC-Co discs and the randomly oriented WC-Co powder are given in Table 4 and Table 5 respectively.

Table 4. Vickers hardness readings for the sample having the rolled WC-Co discs

Indentation No.	d1 (μm)	d2 (μm)	Hardness (HV)
1	51.1	52	697.8
2	42.6	43.5	1002.9
3	48.7	46.3	821.9
4	44.7	42.9	966.6
5	45.9	50.6	796.5
6	46.1	49.7	808.2
7	48	51.2	753.8
8	52.1	49.5	718.6
9	47.6	49.6	785.1
10	53	51.8	675.4

The mean micro-hardness obtained for the sample with the rolled WC-Co discs is 802.68 HV with a standard deviation of 107.68 HV. These values are equivalent to 7.87±1.05 GPa.

Table 5. Vickers hardness readings for the sample having the randomly oriented WC-Co powder

Indentation Number	d1 (μm)	d2 (μm)	Hardness (HV)
1	50.6	51.2	715.8
2	53.4	53.7	646.7
3	48.7	48.9	778.7
4	48.9	49.4	767.6
5	50.6	51.1	717.2
6	51.4	49.8	724.3
7	45.9	45.9	880.2
8	44.6	47.8	868.8
9	53	56	624.3
10	49.6	49.6	753.8

The mean micro-hardness obtained for the sample with the randomly oriented WC-Co powder is 747.74 HV with a standard deviation of 82.69 HV. These values are equivalent to 7.33±0.81 GPa.

The average composite hardness of the sample having the rolled WC-Co discs is thus about 7.5% higher than the average composite hardness of the sample having the randomly oriented WC-Co powder.

5.2.2 Abrasion Resistance Testing of Bulk WC-Co Composites

For an initial comparative estimate of the abrasive wear resistance (which is a function of the average hardness) of the surface, mounted samples having the rolled WC-Co discs and the randomly oriented WC-Co powder were subjected to a scratch test using a precision engraver having a diamond engraving bit. The average normal force applied was ~5N. Figure 59 shows an image of the scratch on the sample having the rolled WC-Co discs taken on a white light interferometer. Similarly, interferometer images of the scratch on the sample having the WC-Co powders are shown in Figure 62.

The scratches were then analyzed using the white light interferometer for finding the shape profile and maximum crater depth. The shape profile of the crater in the sample having the rolled WC-Co discs is shown in Figure 60. Similarly, Figure 63 shows the shape profile of the crater in the sample having the randomly oriented WC-Co powders.

The depth analysis plot of the scratches in the samples having the rolled WC-Co discs and the randomly oriented WC-Co powders are shown in Figure 61 and Figure 64 respectively. From the two plots, we can observe that the maximum crater depth for the sample having the rolled WC-Co discs is 41.916 μm (Figure 61). Whereas from Figure 64, we can observe the maximum crater depth for the sample having the randomly oriented WC-Co powders is 51.291 μm. Thus, the crater depth for the sample that is randomly oriented is about 25% greater than the crater depth for the sample having a dominant basal plane texture.

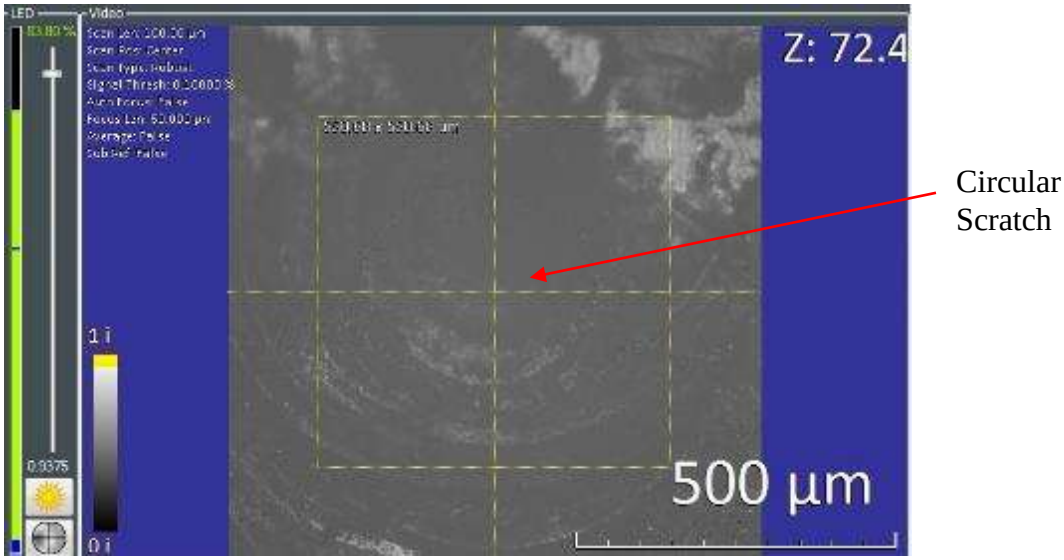

Figure 59. Interferometer image of the scratch on the sample having the rolled WC-Co discs

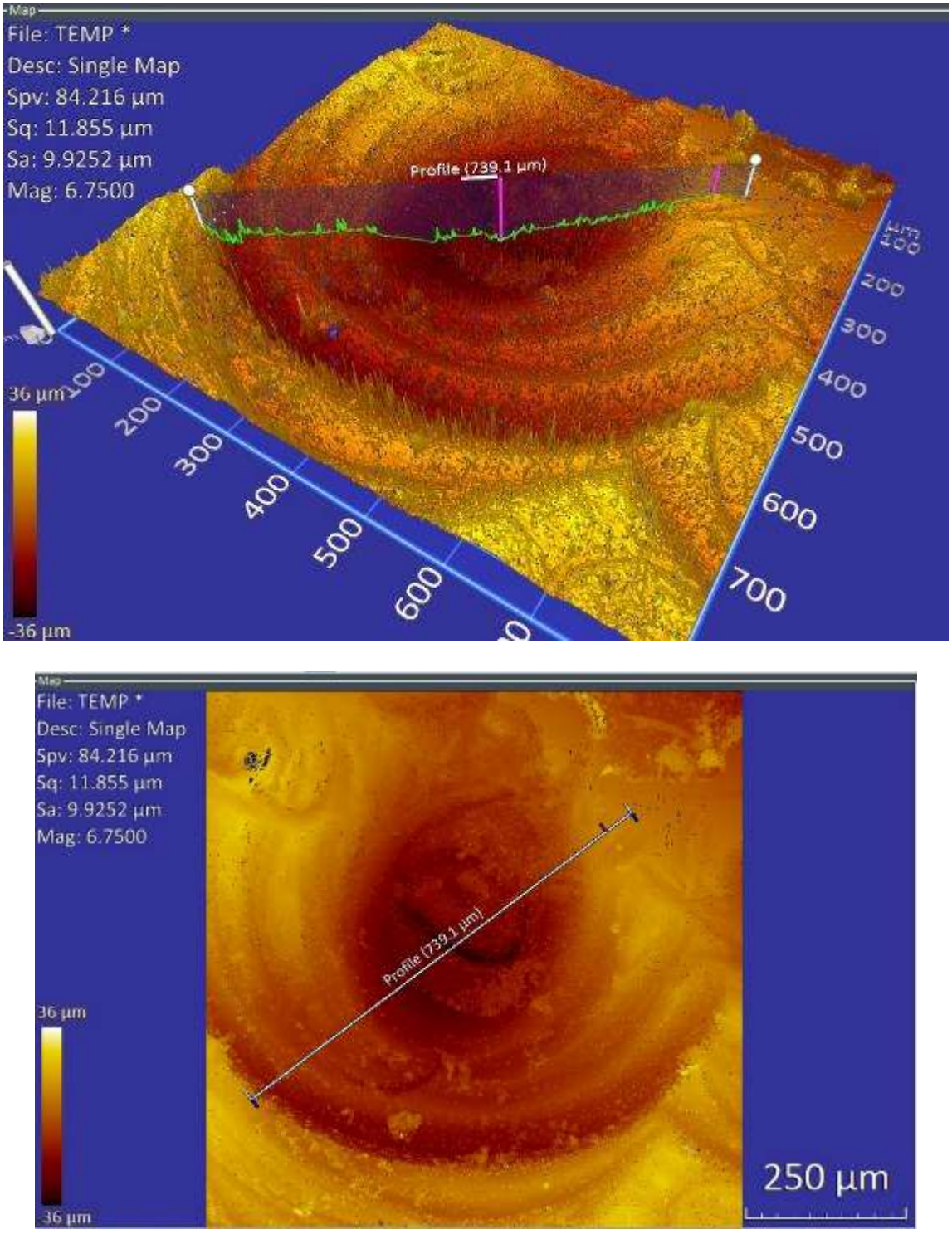

Figure 60. 3D profile of the scratch in the sample having the rolled WC-Co discs (top), 2D profile of the scratch in the sample having the rolled WC-Co discs (bottom)

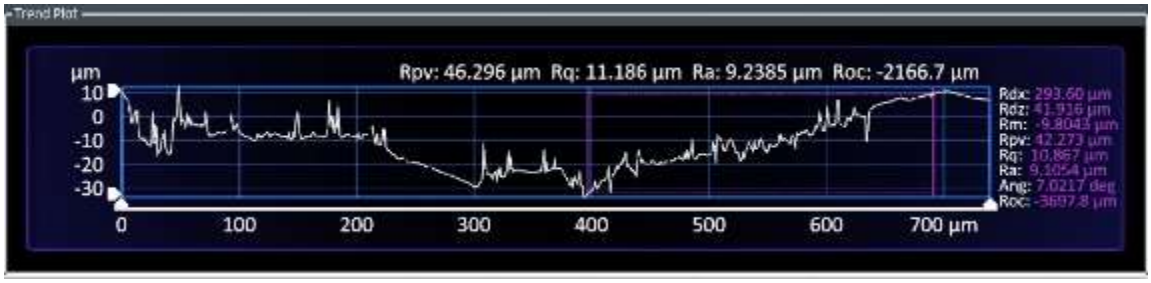

Figure 61. Depth analysis plot of the scratch in the sample having the rolled WC-Co discs. The maximum crater depth of the scratch (Rdz) is 41.916 µm.

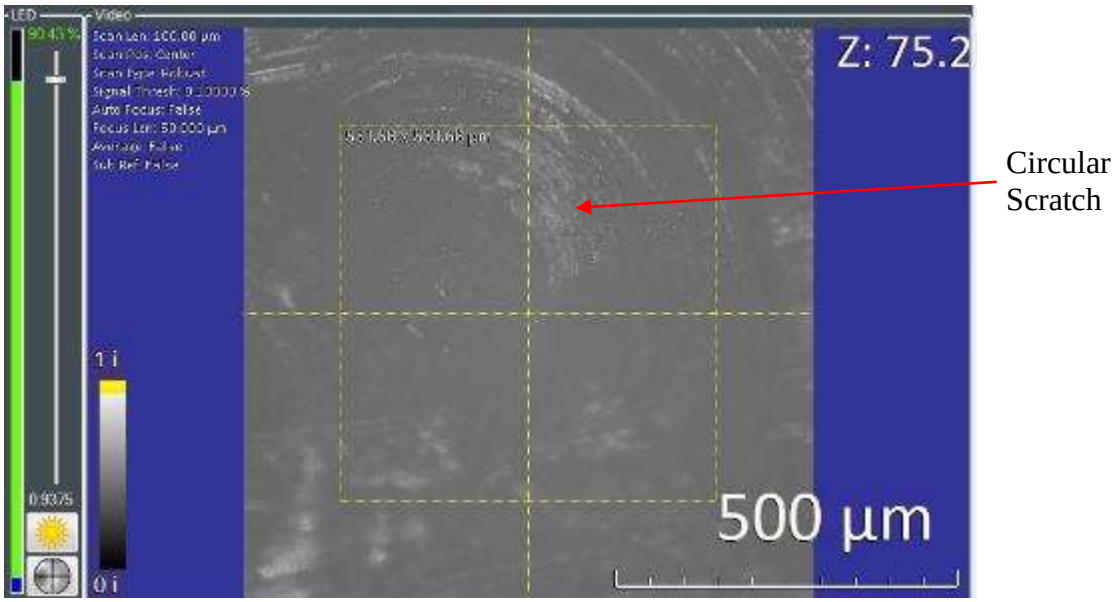

Figure 62. Interferometer image of the scratch on the sample having the randomly oriented WC-Co powders

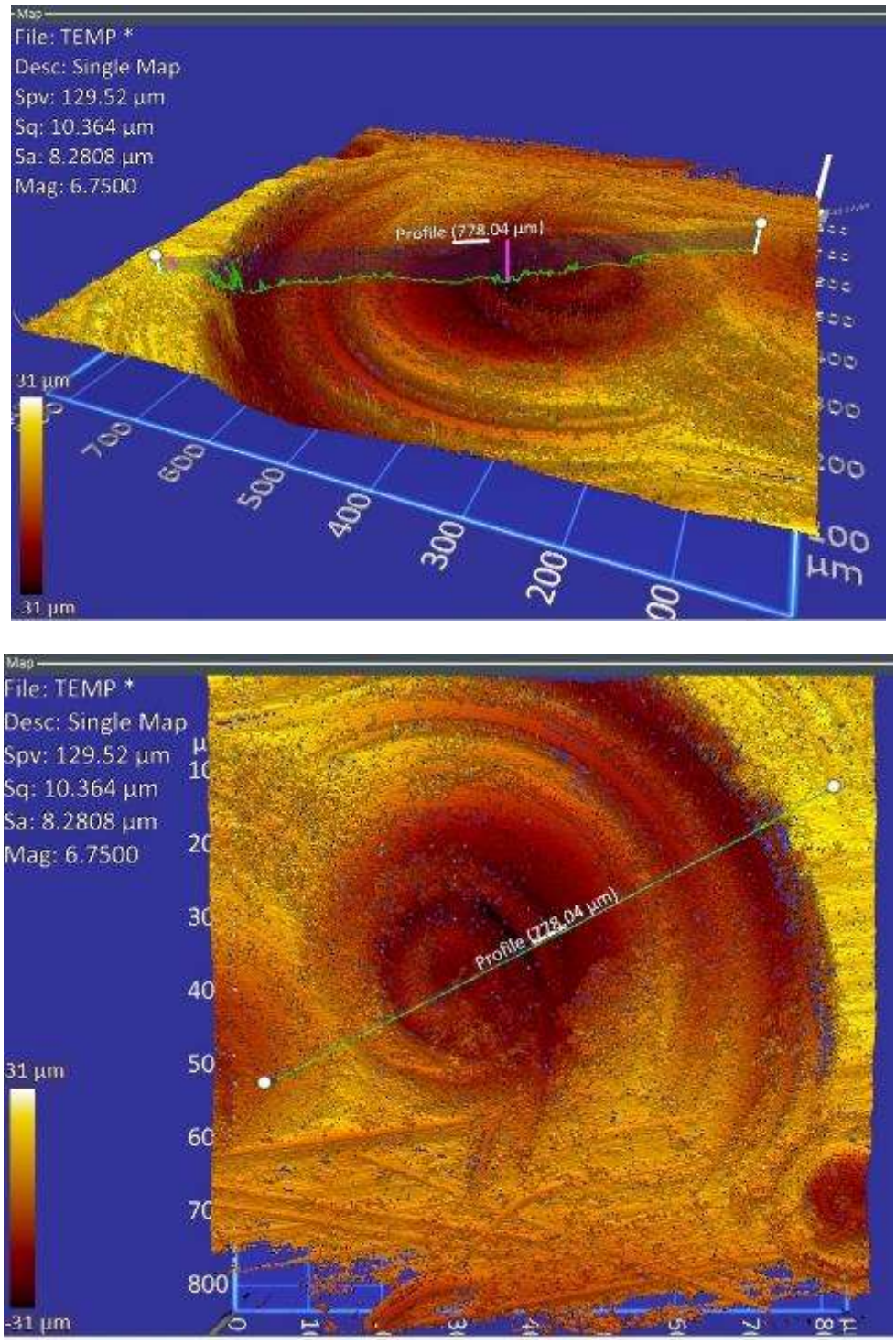

Figure 63. 3D profile of the scratch in the sample having the randomly oriented WC-Co powders (top), 2D profile of the scratch in the sample having the randomly oriented WC-Co powders (bottom)

Figure 64. Depth analysis plot of the scratch in the sample having the randomly oriented WC-Co powders. The maximum crater depth of the scratch (Rdz) is 51.291 µm.

During the scratch testing, the samples with a more random texture i.e. the sample with the WC-Co powders developed a maximum crater depth that was about 25% larger when compared to the sample having a dominant basal plane texture i.e. the sample with the rolled WC-Co discs. This higher depth in the more randomly texture sample can be associated with the lower hardness values obtained in the nano-indentation tests.

In addition, these samples were also subjected to scratch tests on a Hysitron Triboindenter. The tip used for the scratch testing has a cono-spherical profile and radius of curvature of ~5 µm. The length of the scratch was fixed at 500 µm and the average normal force applied was 100mN.

Figure 65 shows an image of the scratch on the sample having the rolled WC-Co discs taken using an optical microscope. Similarly, a microscope image of the scratch on the sample having the WC-Co powders is shown in Figure 66.

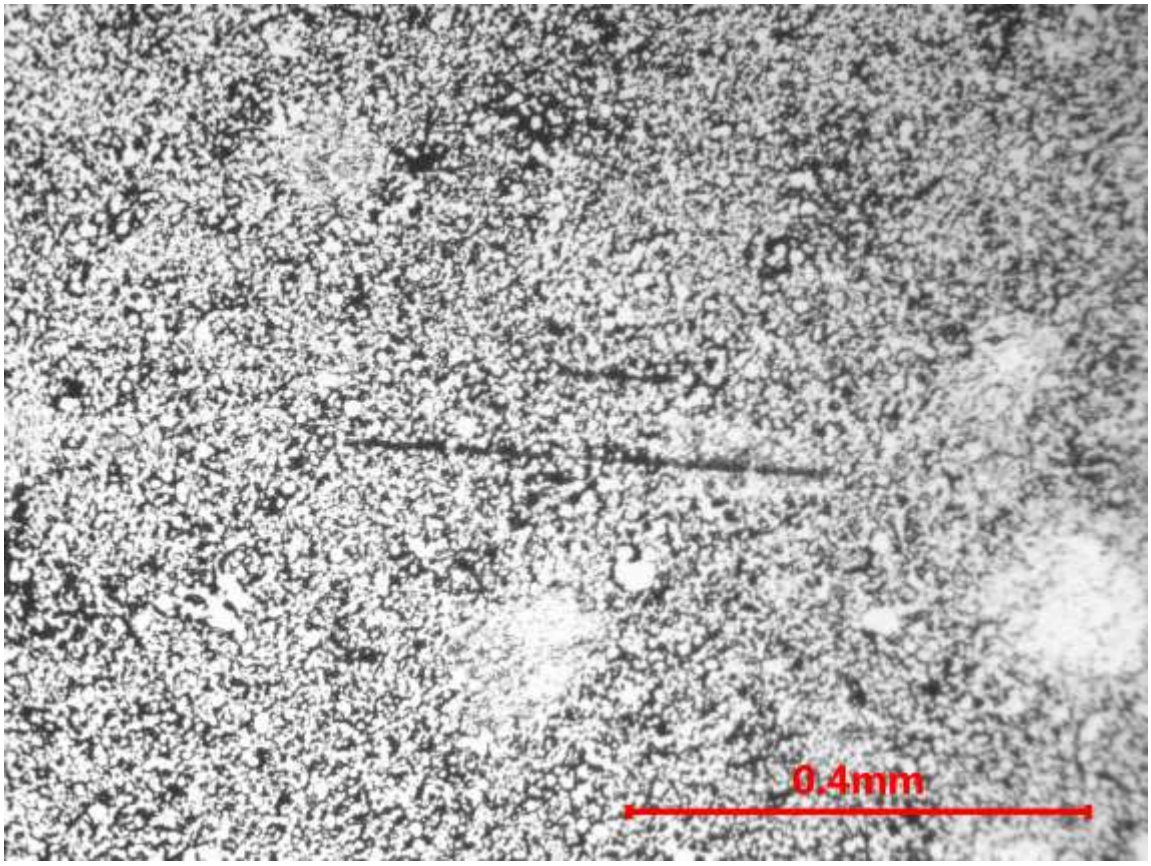

Figure 65. Microscope image of the scratch on the sample having the rolled WC-Co discs

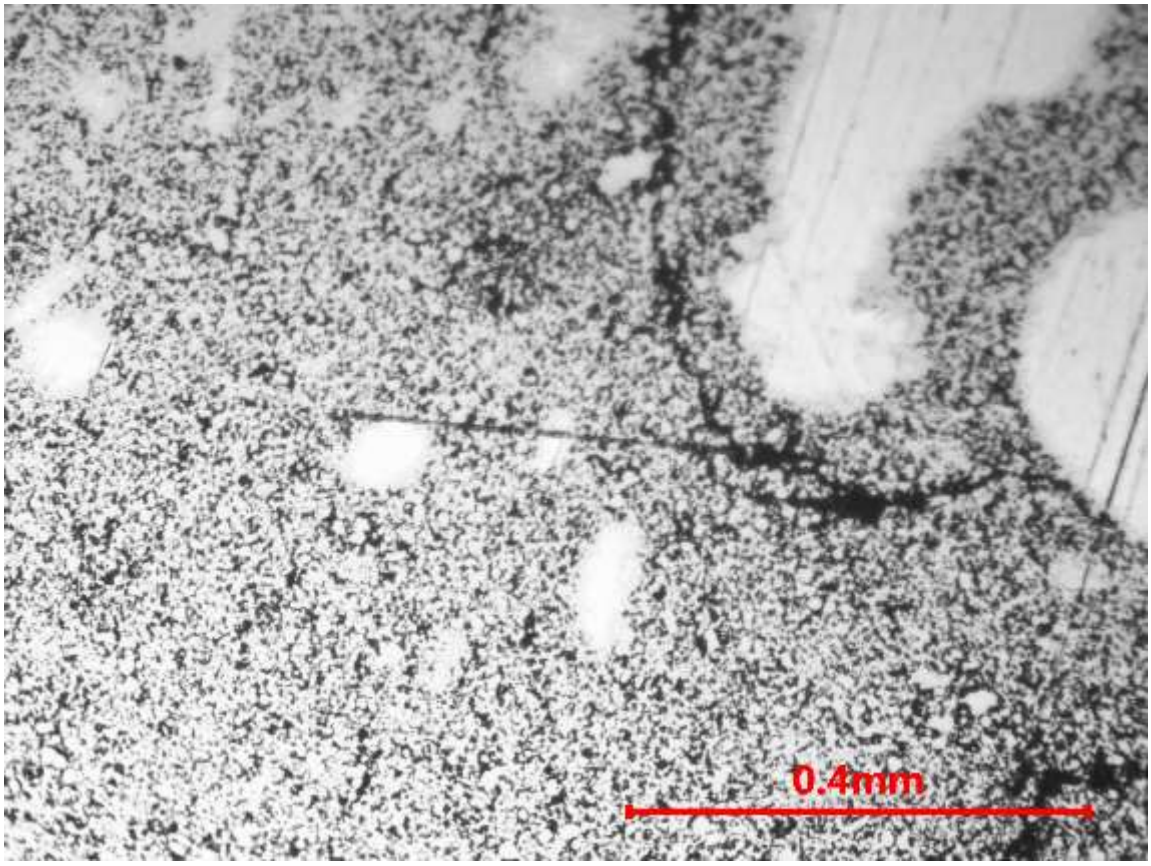

Figure 66. Microscope image of the scratch on the sample having the randomly oriented WC-Co powders

The scratches were then analyzed using a white light interferometer for finding the crater depths and width along different lines across the scratch. The shape profile and depth analysis plot for one of the craters in the sample having the rolled WC-Co discs is shown in Figure 67. Similarly, Figure 68 shows the shape profile and depth analysis plot for one of the craters in the sample having the randomly oriented WC-Co powders.

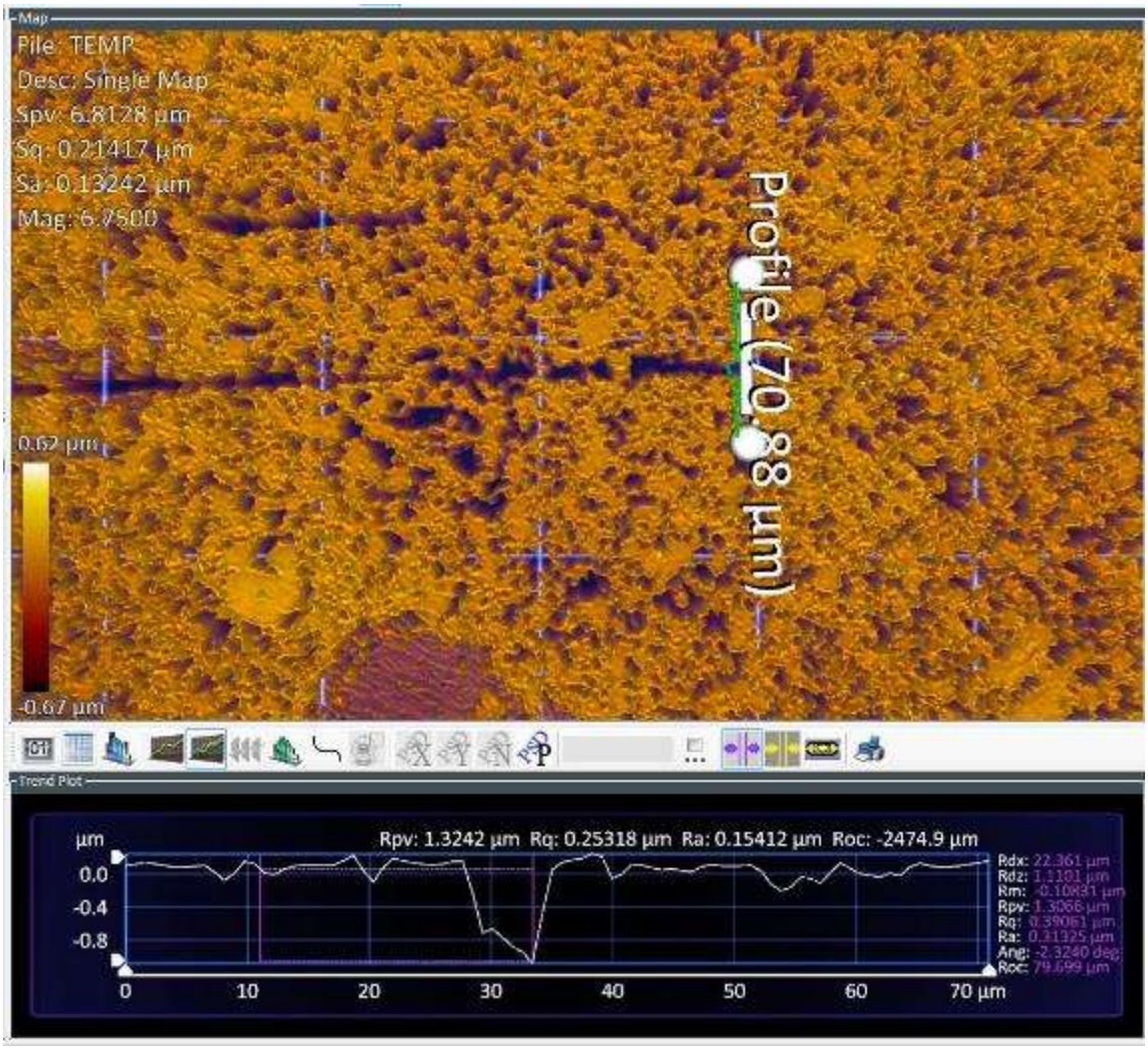

Figure 67. Shape profile and depth analysis plot of one of the scratches in the sample having the rolled WC-Co discs. The maximum crater depth of the scratch (Rdz) is 1.110 µm.

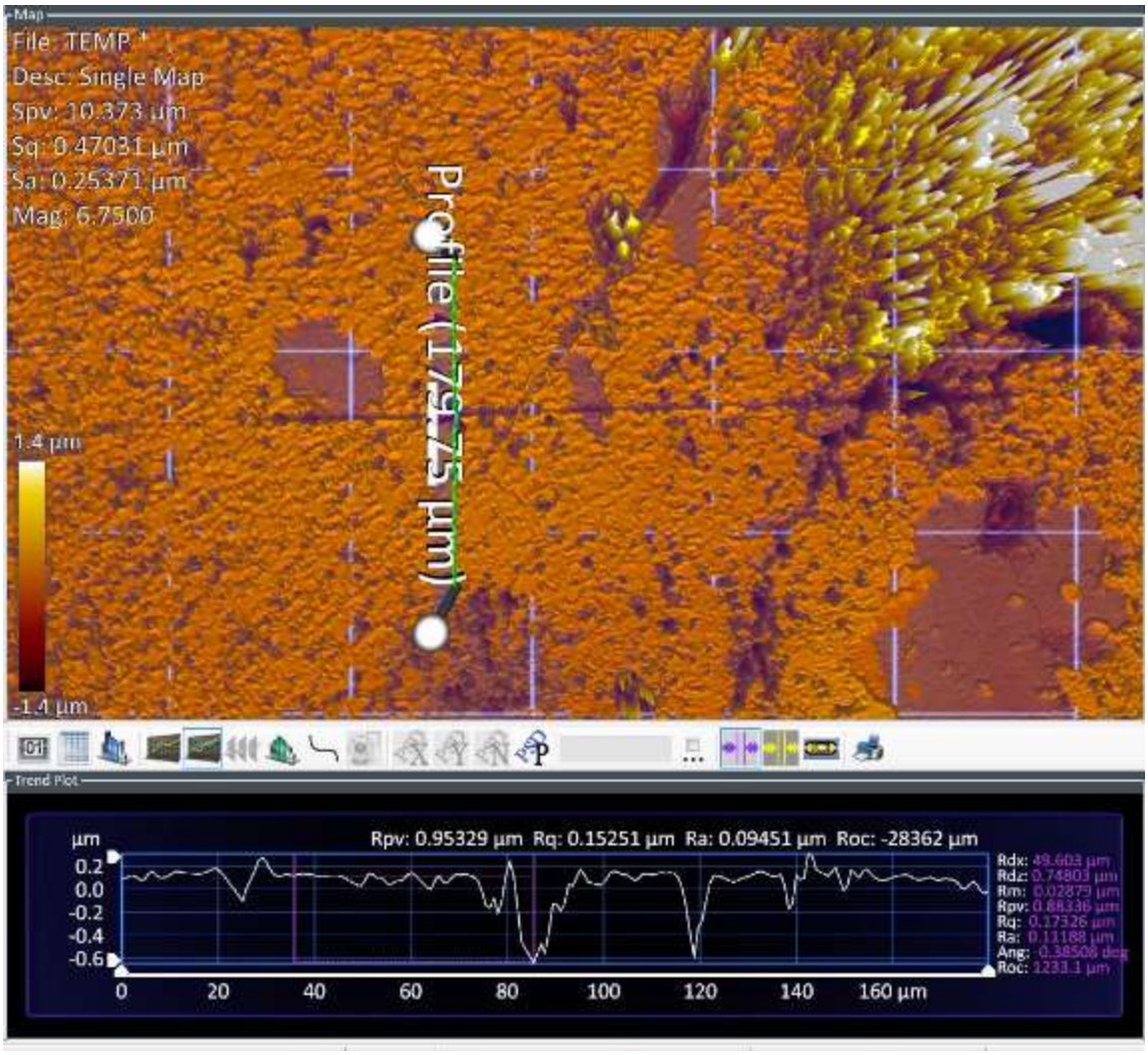

Figure 68. Shape profile and depth analysis plot of one of the scratches in the sample having the randomly oriented WC-Co powders. The maximum crater depth of the scratch (Rdz) is 0.748 µm.

Five (5) regions along the length of the scratches on both the samples are analyzed to find the depth and width of the craters and shown in Table 6 and Table 7. Plots showing the normal force and normal displacement versus time for the scratch testing on the sample having the rolled WC-Co discs are shown in Figure 69.

Table 6. Depth and width of 5 regions along the length of the scratch on the sample having the rolled WC-Co discs

Reading Number	**Depth (µm)**	**Width (µm)**
1	1.110	8.239
2	1.387	7.435
3	1.352	8.359
4	0.740	9.740
5	0.717	7.462
Mean	1.061	8.247
Standard Deviation	0.322	0.938

Table 7. Depth and width of 5 regions along the length of the scratch on the sample having the randomly oriented WC-Co powders

Reading Number	Depth (µm)	Width (µm)
1	0.748	14.648
2	0.596	15.210
3	0.317	12.536
4	0.723	6.744
5	0.443	13.356
Mean	0.565	12.499
Standard Deviation	0.184	3.385

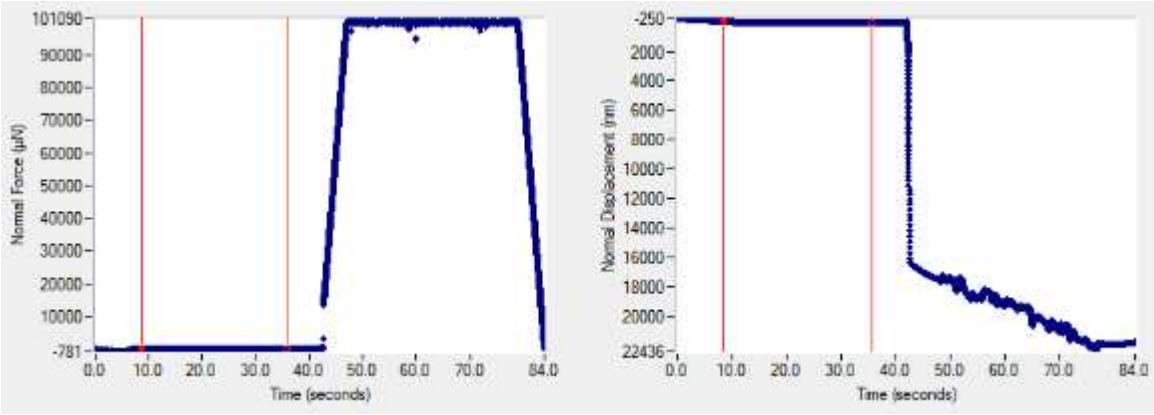

Figure 69. Plot showing the normal force versus time for the scratch testing on the sample having the rolled WC-Co discs (left), and plot showing normal displacement versus time for the scratch testing on the sample having the rolled WC-Co discs (right).

For Table 6, we can observe that the mean depth and width of the craters for the sample having the rolled WC-Co discs are 1.061±0.322 µm and 8.247±0.938 µm respectively. Similarly, from Table 7 we can observe that the mean depth and width of the craters for the sample having the randomly oriented WC-Co powder are 0.565±0.184 µm and 12.499±3.385 µm respectively. The force control as shown in the left of Figure 69 seemed good for both the samples. However for the sample having the randomly oriented WC-Co powder, inconsistencies were observed in the normal displacement versus time plot. One of the possible reason could be the presence of a tilt in the sample i.e. the sample might not have been perfectly flat. Additionally, no trend of increasing or decreasing dimensions were observed in craters on both the samples. The mean width of the crater for the sample having the rolled WC-Co discs was higher compared to the sample having the randomly oriented WC-Co powder. This was along expected lines as the hardness of this sample was higher which should have caused higher abrasion wear and hence the

higher width of craters. However, the mean depth of craters for both the samples did not compare along expected lines. Further scratch testing would be required following tilt correction to get more accuracy and consistency in the readings.

5.3 Discussion of Results

This chapter served to answer RQ2. The WC-Co samples were subjected to mechanical hardness testing and tests to measure abrasion resistance to evaluate the effect of the texture dominance of WC grains and the resulting mechanical properties of the WC-Co bulk composite.

The sample having the rolled WC-Co discs had a higher area ratio of basal planes compared to the sample having the WC-Co powder as deduced from the XRD results from RQ1. This sample with a more dominant basal plane texture *i.e.* the sample having the rolled WC-Co discs also had about 36% higher average hardness values when compared to the sample with a more random texture.

Since hardness is related to the abrasive wear resistance of a material (directly proportional), the sample with a more dominant basal plane texture would be expected to exhibit better abrasion resistance. During the scratch testing using a diamond engraver, the samples with a more random texture *i.e.* the sample with the randomly oriented WC-Co powders developed a crater that had about 25% larger maximum depth when compared to the sample having a dominant basal plane texture, *i.e.* the sample with the rolled WC-Co discs. This higher wear depth in the more randomly textured sample can be associated with the lower hardness values obtained in the nano-indentation tests.

6. CONCLUSIONS AND FUTURE WORK

The objective of this research work was to develop a procedure to obtain dominant grain orientation texture in WC-Co composites, and to study the effect of such texture dominance on its hardness and abrasion resistance.

A scalable fabrication procedure was developed and refined that involved a rolling-extended operation that helped achieve a certain degree of control over the grain orientation texture of WC-Co composites. Dominance of basal plane grain orientation was observed in the samples fabricated using the rolled WC-Co oriented discs as compared to randomly oriented powder. The SEM images point to higher rates of grain growth in the basal plane orientation in the samples fabricated from the rolled WC-Co discs. There was 21% increase (46% vs. 67%) in intensity of the basal plane peaks in the X-ray diffraction patterns of the rolled WC-Co discs area compared to the area having the WC-Co powders.

The nano-indentation results show that the sample made from the rolling-extended WC-Co oriented-sheets had a 36% average increase in the hardness value when compared to the sample made with WC-Co powders. Additionally, the micro-hardness results show that the sample made from the rolling-extended WC-Co oriented-sheets had about 7.5% average increase in the hardness value when compared to the sample made with WC-Co powders. Though hardness measurements using nano and micro indentations show higher hardness for the rolled sheets, that difference in these values could be attributed to probing individual grains vs. indenting larger composite areas consisting of multiple grans and cobalt binder. These higher hardness values could be attributed to the higher area ratio of

basal planes present on the surface of the sample having the rolled WC-Co discs. Further, scratch tests using a diamond engraver were conducted on both the samples, and it showed a 25% increase in the maximum crater depth in the sample having a more random grain orientation texture. This is attributed to the lower average hardness of the samples having the randomly oriented grains. This strengthens the argument that the samples having a more dominant basal plane texture have higher wear resistance.

Thus, evidence of the effect of dominant grain orientation texture (harder basal planes) on the hardness and abrasion resistance of WC-Co composites was obtained. This method of rolling-extension has the potential to be applied towards texturing of bulk/sheet hard-materials. Additionally, this method could be an avenue to achieve control over other mechanical properties as well.

The following future work is suggested to further this work:

- Starting with plate-like tungsten carbide particles having a high aspect ratio for the rolling-extension procedure, and comparing the effects on the mechanical properties,
- Evaluating the feasibility of the procedure to develop bulk WC-Co composites having gradients in grain sizes (please see below for preliminary results),
- Investigating the effects of dominant basal plane texture on other material properties such as ductility, impact strength, fracture resistance, etc., and
- Quantifying the dispersion of cobalt in spark plasma sintered WC-Co composites in a sample-size independent manner [46].

For fabricating gradient WC-Co samples, four WC powders having different particle sizes (~0.4 μm, ~3.35 μm, ~4 μm, and ~7 μm) were sourced from suppliers of

WC-Co cutting tools. These WC powders were then mixed with Co powder (average particle size ~1.7 µm) is the ratio of 9:1 (by weight) to obtain four sets of WC-10%Co powders. These powders were stacked up in a spark plasma sintering die (having a diameter of 20mm) with graphite sheets between different WC-Co powder layers. These powders were cold pressed and sintered using the procedure mentioned in section 4.3. A sectioned portion of the sintered sample is shown in Figure 70. SEM images of the transition of WC particle sizes from ~0.4 µm to ~7 µm and from ~4 µm to ~3.35 µm are shown in Figure 71 and Figure 72 respectively.

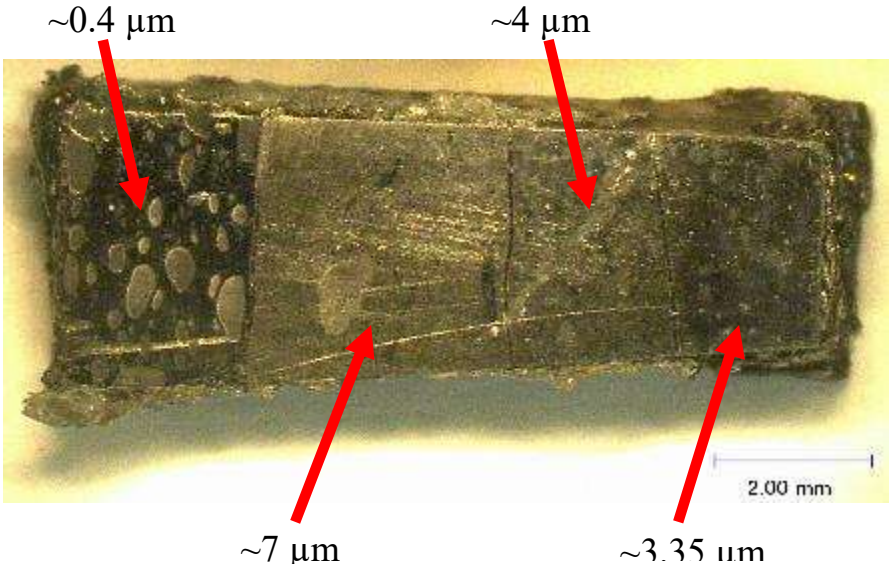

Figure 70. Image of a sectioned region of the gradient WC-Co sample. The 4 regions given the red arrows have different WC particles sizes. The particle size for the cobalt powder used is ~1.7 µm for all the regions.

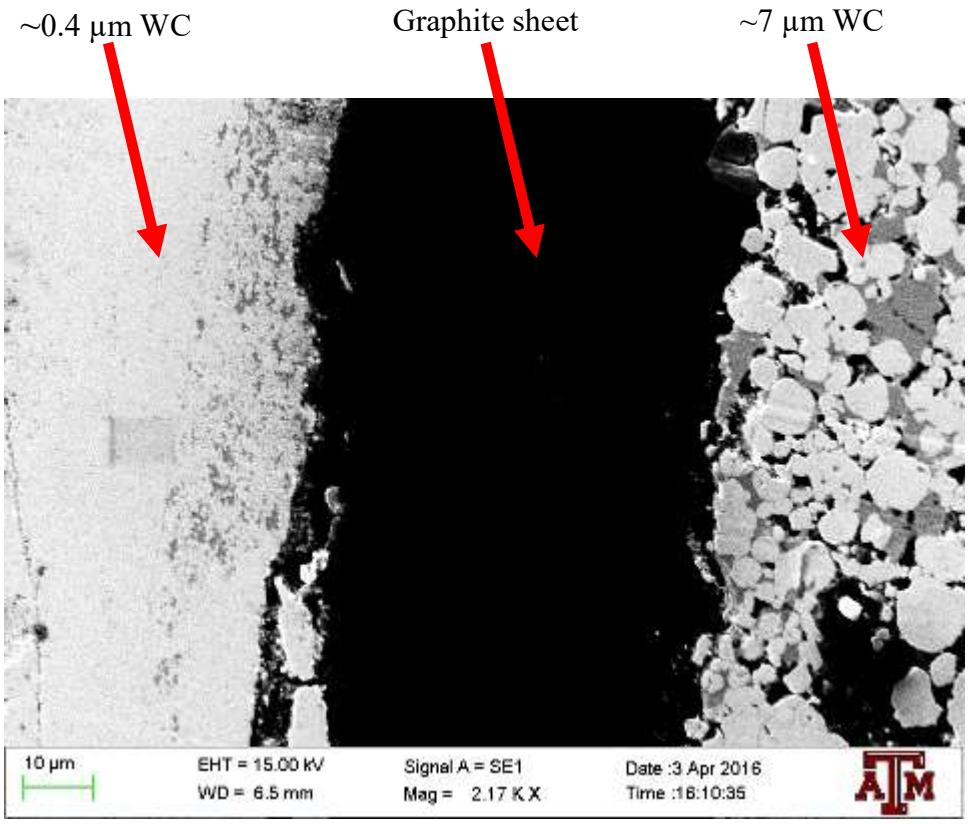

Figure 71. SEM image showing the transition from particle size of ~0.4 µm to ~7 µm in the gradient sample. The black region in the center is the graphite sheet.

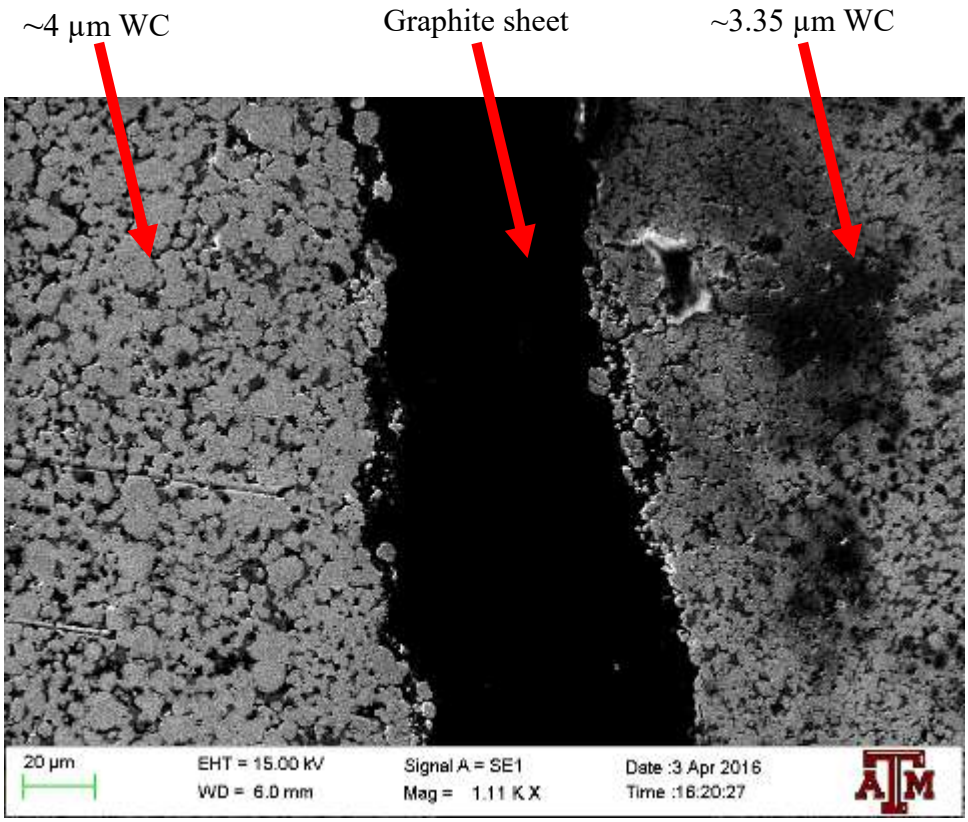

Figure 72. SEM image showing the transition from particle size of ~4 µm to ~3.35 µm in the gradient sample. The black region in the center is the graphite sheet.

REFERENCES

[1] Roebuck, B., Klose, P., and Mingard, K. P., 2012, "Hardness of hexagonal tungsten carbide crystals as a function of orientation," Acta Materialia, 60(17), pp. 6131-6143.

[2] Csanádi, T., Bl'anda, M., Chinh, N. Q., Hvizdoš, P., and Dusza, J., 2015, "Orientation-dependent hardness and nanoindentation-induced deformation mechanisms of WC crystals," Acta Materialia, 83(0), pp. 397-407.

[3] Kim, C.-S., 2007, "Modeling the influence of orientation texture on the strength of WC-Co composites," Journal of the American Ceramic Society, 90(1), pp. 199-204.

[4] Bartolucci Luyckx, S., and Katzourakis, J., 1991, "Preparation and properties of WC–Co textured components," Materials Science and Technology, 7(5), pp. 472-474.

[5] Isakov, E., 2008, Cutting Data for Turning of Steel, Industrial Press.

[6] Reeber, R. R., and Wang, K., 1999, "Thermophysical Properties of α-Tungsten Carbide," Journal of the American Ceramic Society, 82(1), pp. 129-135.

[7] Lay, S., Allibert, C. H., Christensen, M., and Wahnström, G., 2008, "Morphology of WC grains in WC–Co alloys," Materials Science and Engineering: A, 486(1–2), pp. 253-261.

[8] Exner, H. E., 1979, "Physical and chemical nature of cemented carbides," International Materials Reviews, 24(1), pp. 149-173.

[9] Kim, C.-S., 2004, "Microstructural-mechanical property relationships in tungsten carbide-cobalt composites," p. 195p.

[10] Borgh, I., Hedström, P., Persson, T., Norgren, S., Borgenstam, A., Ågren, J., and Odqvist, J., 2014, "Microstructure, grain size distribution and grain shape in WC–Co alloys sintered at different carbon activities," International Journal of Refractory Metals and Hard Materials, 43(0), pp. 205-211.

[11] Mannesson, K., 2011, "WC grain growth during sintering of cemented carbides," Royal Institute of Technology, Stockholm, Sweden.

[12] Kalpakjian, S., and Schmid, S. R., 2003, Manufacturing Processes for Engineering Materials, Prentice Hall.

[13] Suwas, B. S., and Ray, R. K., 2014, Crystallographic Texture of Materials, Springer, London, GBR.

[14] Bunge, H. J., 1999, "Texture microstructure and properties of polycrystalline materials," NASAT-97: First national seminar on the application of textures in materials research, R. K. R. a. A. K. Singh, ed., Oxford and IBH Publishing, New Delhi, Hyderabad, India, pp. 3-44.

[15] Doitpoms.ac.uk, "DoITPoMS - TLP Library Crystallographic Texture - Representing Texture," http://www.doitpoms.ac.uk/tlplib/crystallographic_texture/texture_representation.php.

[16] Aluminium.matter.org.uk, "Representing Texture | Orientation Distribution Function (ODF),"

http://aluminium.matter.org.uk/content/html/ENG/default.asp?catid=100&pageid=1050588871.

[17] Hutchinson, W. B., and Ekström, H. E., 1990, "Control of annealing texture and earing in non-hardenable aluminium alloys," Materials science and technology, 6(11), pp. 1103-1112.

[18] Wang, Q. W., Fan, G. H., Geng, L., Zhang, J., Cui, X. P., Pang, J. C., Qin, S. H., and Du, Y., 2013, "A novel fabrication route to microlaminated TiB2–NiAl composite sheet with {111}<μνω> texture by roll bonding and annealing treatment," Intermetallics, 37(0), pp. 46-51.

[19] Alizadeh, R., Mahmudi, R., Ngan, A. H. W., and Langdon, T. G., 2015, "Microstructural stability and grain growth kinetics in an extruded fine-grained Mg–Gd–Y–Zr alloy," Journal of Materials Science, 50(14), pp. 4940-4951.

[20] Shimoyama, K., Yokoyama, S., Kaneko, S., and Fujita, F., 2014, "Effect of grooved roll profiles on microstructure evolutions of AZ31 sheets in Periodical Straining Rolling process," Materials Science and Engineering: A, 611(0), pp. 58-68.

[21] Sha, Y. H., Zhou, S. C., Pei, W., and Zuo, L., 2007, "Application of Asymmetric Rolling to Texture Control of Silicon Steel," Materials science forum, 539(4), pp. 3424-3429.

[22] Sakai, T., Yoneda, K., and Osugi, S., 2005, "Microstructure and Texture Control of Al-Mg Alloy Sheets by Differential Speed Rolling," Materials science forum, 495(1), pp. 597-602.

[23] Kim, W. J., Yoo, S. J., Chen, Z. H., and Jeong, H. T., 2009, "Grain size and texture control of Mg–3Al–1Zn alloy sheet using a combination of equal-channel angular rolling and high-speed-ratio differential speed-rolling processes," Scripta Materialia, 60(10), pp. 897-900.

[24] Sha, Y. H., Sun, C., Zhang, F., Patel, D., Chen, X., Kalidindi, S. R., and Zuo, L., 2014, "Strong cube recrystallization texture in silicon steel by twin-roll casting process," Acta Materialia, 76(0), pp. 106-117.

[25] Kim, K., and Yoon, J., 2015, "Effects of starting microstructure and billet orientations on the texture evolution and the mechanical behavior of Mg-3Al-1Zn rolled plate by half channel angular extrusion (HCAE)," Mater. Sci. Eng. A-Struct. Mater. Prop. Microstruct. Process., 622, pp. 46-51.

[26] Sagapuram, D., Efe, M., Trumble, K., and Chandrasekar, S., 2014, "Enabling shear textures and fine-grained structures in Magnesium sheet by machining-based deformation processing," IOP Conference Series: Materials Science and Engineering, IOP Publishing, p. 012155.

[27] Shibayanagi, T., and Naka, M., 2007, "Control of Grain Size and Texture in Al Alloys Utilizing Friction Stir Processing," Materials science forum, 539(4), pp. 3769-3774.

[28] Chen, J., Fujii, H., Sun, Y., Morisada, Y., and Ueji, R., 2013, "Fine grained Mg–3Al–1Zn alloy with randomized texture in the double-sided friction stir welded joints," Materials Science and Engineering: A, 580(0), pp. 83-91.

[29] Chen, J., Ueji, R., and Fujii, H., 2015, "Double-sided friction-stir welding of magnesium alloy with concave–convex tools for texture control," Materials & Design, 76(0), pp. 181-189.

[30] Raihanuzzaman, R. M., Xie, Z., Hong, S. J., and Ghomashchi, R., 2014, "Powder refinement, consolidation and mechanical properties of cemented carbides — An overview," Powder Technology, 261(0), pp. 1-13.

[31] Lu, K., 2008, "Sintering of nanoceramics," International Materials Reviews, 53(1), pp. 21-38.

[32] Kuttolamadom, M. A., Laine Mears, M., and Kurfess, T. R., 2015, "The Correlation of the Volumetric Wear Rate of Turning Tool Inserts With Carbide Grain Sizes," Journal of Manufacturing Science and Engineering, 137(1), pp. 011015-011015.

[33] Suárez, M., Fernández, A., Kessel, H., Hennicke, J., Menéndez, J., Kirchner, R., Torrecillas, R., and Kessel, T., 2013, Challenges and opportunities for spark plasma sintering: a key technology for a new generation of materials, INTECH Open Access Publisher.

[34] Mamedov, V., 2002, "Spark plasma sintering as advanced PM sintering method," POWDER METALLURGY, 45(4), pp. 322-328.

[35] Mandel, K., Krüger, L., and Schimpf, C., 2014, "Study on parameter optimisation for field-assisted sintering of fully-dense, near-nano WC–12Co," International Journal of Refractory Metals and Hard Materials, 45(0), pp. 153-159.

[36] Shatov, A. V., Ponomarev, S. S., and Firstov, S. A., 2009, "Modeling the effect of flatter shape of WC crystals on the hardness of WC-Ni cemented carbides," International Journal of Refractory Metals and Hard Materials, 27(2), pp. 198-212.

[37] Ning, J. L., 2006, "Preparation of textured zinc oxide ceramics by extrusion and spark plasma sintering," Advances in applied ceramics, 105(6), p. 265.

[38] Ishii, K., and Tashiro, S., 2008, "Fabrication of orientation-controlled bismuth-layer-structured ferroelectric ceramics by rolling-extended method and their piezoelectric properties," Journal of the Ceramic Society of Japan, 116(1360), pp. 1304-1308.

[39] Li, T., Li, X., Zhao, Z., Dai, Y., and Ji, H., 2015, "Evolution of textured Ca0.85(LiCe)0.075Bi4Ti4O15 ceramics via templated grain growth using a rolling-extended method," J Mater Sci: Mater Electron, 26(4), pp. 2082-2089.

[40] Tashiro, S., and Ishii, K., 2010, "Fabrication of grain-oriented MgO ceramics by the rolling-extended method," Journal of the Ceramic Society of Japan, 118(1382), pp. 927-931.

[41] Youseffi, M., and Menzies, I. A., 1997, "Injection moulding of WC–6Co powder using two new binder systems based on montanester waxes and water soluble gelling polymers," Powder metallurgy, 40(1), pp. 62-65.

[42] Kramer, B. M., 1986, "A Comprehensive Tool Wear Model," Ann. CIRP, 35(1), pp. 67-70.

[43] Larsen-Basse, J., 1978, "Abrasion mechanism - Delamination to Machining," Proc. of Int. Conf. on the Fundamentals of Tribology, MIT Press, Cambridge, p. 679.

[44] Rabinowicz, E., 1995, Friction and wear of materials. 2nd ed, New York : Wiley

[45] England, G., "Vickers Hardness Test," http://www.gordonengland.co.uk/hardness/vickers.htm.

[46] Yazdanbakhsh, A., Grasley, Z., Tyson, B., and Al-Rub, R. K. A., 2011, "Dispersion quantification of inclusions in composites," Composites Part A: Applied Science and Manufacturing, 42(1), pp. 75-83.